

DETERMINATION OF SUSCEPTIBILITY TO INTERGRANULAR
CORROSION OF UNS 31803 TYPE DUPLEX STAINLESS STEEL
BY ELECTROCHEMICAL REACTIVATION TECHNIQUE

A THESIS SUBMITTED TO
THE GRADUATE SCHOOL OF NATURAL AND APPLIED SCIENCES
OF
MIDDLE EAST TECHNICAL UNIVERSITY

BY

MEHMET EMİN ARIKAN

IN PARTIAL FULFILLMENT OF THE REQUIREMENTS
FOR
THE DEGREE OF MASTER OF SCIENCE
IN
METALLURGICAL AND MATERIALS ENGINEERING

AUGUST 2008

Approval of the thesis:

DETERMINATION OF SUSCEPTIBILITY TO INTERGRANULAR CORROSION OF UNS 31803 TYPE DUPLEX STAINLESS STEEL BY ELECTROCHEMICAL REACTIVATION TECHNIQUE

submitted by **MEHMET EMİN ARIKAN** in partial fulfillment of the requirements for the degree of **Master of Science in Metallurgical and Materials Engineering Department, Middle East Technical University** by,

Prof. Dr. Canan Özgen
Dean, Graduate School of **Natural and Applied Sciences** _____

Prof. Dr. Tayfur Öztürk
Head of Department, **Metallurgical and Mat. Engineering** _____

Prof. Dr. Mustafa Doruk
Supervisor, **Metallurgical and Mat. Eng. Dept., METU** _____

Examining Committee Members:

Prof. Dr. Semra Bilgiç
Chemistry Dept., Ankara University _____

Prof. Dr. Mustafa Doruk
Metallurgical and Materials Engineering Dept., METU _____

Prof. Dr. M. Kadri Aydınol
Metallurgical and Materials Engineering Dept., METU _____

Prof. Dr. Cevdet Kaynak
Metallurgical and Materials Engineering Dept., METU _____

Prof. Dr. C. Hakan Gür
Metallurgical and Materials Engineering Dept., METU _____

Date: 06.08.2008

I hereby declare that all information in this document has been obtained and presented in accordance with academic rules and ethical conduct. I also declare that, as required by these rules and conduct, I have fully cited and referenced all material and results that are not original to this work.

Name, Last name: Mehmet Emin ARIKAN

Signature:

ABSTRACT

DETERMINATION OF SUSCEPTIBILITY TO INTERGRANULAR CORROSION OF DUPLEX STAINLESS STEEL TYPE UNS 31803 BY ELECTROCHEMICAL REACTIVATION TECHNIQUE

Arıkan, Mehmet Emin

M. S., Department of Metallurgical & Materials Engineering
Supervisor: Prof. Dr. Mustafa Doruk

August 2008, 125 pages

In the present work the effect of isothermal ageing treatment on the microstructure and on the localized corrosion resistance of a duplex stainless steel (DSS) was investigated. Specimens taken from a hot rolled cylindrical duplex stainless bar with 22% Cr grade were solution annealed at 1050°C and then sensitization heat treatments were conducted at 650, 725 and 800°C with duration ranging from 100 to 31622 min.

The microstructural changes were examined by the light optical microscopy (LOM) and scanning electron microscopy (SEM). XRD technique and EDS analysis were used for microstructural evolution. Double Loop Electrochemical Potentiodynamic Reactivation (DLEPR) and standard weight loss immersion acid tests were performed in order to determine the degree of sensitization (DOS) to intergranular corrosion. The surfaces remained after the DLEPR test and the weight loss immersion test were also examined to observe the attack locations and their relationship with the chromium depleted zones.

The degree of sensitization is measured by determining the ratio of the maximum current generated by the reactivation (reverse) scan to that of the anodic (forward) scan, $(I_r/I_a) \times 100$. I_r is very small (less than 10^{-5} A/cm²) for solution annealed samples at 1050°C for 1 hr and those aged at 650°C for 100 and 316 min after the solution heat treatment, with the I_r/I_a ratios of 0.027634%, 0.033428% and 0.058928% respectively. Hence these samples were considered as unsensitized and their microstructure was composed of primary ferrite and austenite.

However, I_r increased to values as high as 10^{-2} A/cm² and even approached I_a for all samples aged for other temperatures and times,

associated with high I_r/I_a ratios. The increased degree of sensitization can be attributed to stronger effect of chromium and molybdenum depleted areas. The microstructure was composed of primary ferrite and austenite including also sigma phase and the secondary austenite that would be responsible for the localized chromium impoverishment.

The time required for sensitization was shorter in samples aged at higher temperatures. Accordingly ageing times of 1000 min at 725°C and of 316 min at 800°C were sufficient, whereas times longer than 10000 min was needed to achieve a sensitized structure at 650°C.

Keywords: Duplex stainless steels (DSS), precipitations in DSS's, intercrystalline corrosion in DSS's, electrochemical potentiodynamic reactivation (EPR) technique.

ÖZ

UNS 31803 TİPİ DUBLEKS PASLANMAZ ÇELİĞİN TANELERARASI KOROZYONA DUYARLILIĞININ ELEKTROKİMYASAL REAKTİVASYON TEKNİĞİYLE BELİRLENMESİ

Arıkan, Mehmet Emin
M.S., Metalurji ve Malzeme Mühendisliği Bölümü
Tez Yöneticisi: Prof. Dr. Mustafa Doruk

Ağustos 2008, 125 sayfa

Bu çalışmada, eşsıcaklık yaşlandırma ısıl işleminin, bir dubleks paslanmaz çeliğin mikroyapı ve yerel korozyon direnci üzerindeki etkisi araştırıldı. %22 krom içeren sıcak haddelenmiş silindirik dubleks paslanmaz çelik çubuktan çıkarılan numuneler önce 1050°C de çözündürme, sonra da 650, 725 ve 800°C sıcaklıklarda yaşlandırma ısıl işlemlerine tabi tutuldular. Her bir sıcaklıkta bir dizi numune 100 dakikadan 31622 dakikaya kadar değişen sürelerde hassaslaşma için bekletildi.

Mikroyapısal değişimler optik ve tarama elektron mikroskobu ile incelendi ve mikroyapısal gelişim için de x-ışını difraksiyon tekniği ve enerji disperzif analiz yöntemi kullanıldı. Ayrıca çift çevirimli elektrokimyasal potansiyodinamik reaktivasyon (DLEPR) ve standart asite daldırılmalı ağırlık kaybı testleri yapıldı. Çift çevirimli elektrokimyasal potansiyodinamik reaktivasyon testinin amacı tanelerarası korozyona karşı hassaslaşma derecesini (DOS) saptamaktı. DLEPR ve asit testleri sırasında korozif ortamdan etkilenen bölgeler ve bunların krom azalmasıyla olan bağlantıları incelendi. Hassaslaşma derecesi, geri ve ileri taramada elde edilen maksimum akım yoğunlukları arasındaki oran, $(I_r/I_a) \times 100$ olarak ölçüldü.

1050°C'de 1 saat süreyle çözündürme ısıl işlemi uygulanmış numunelerle, 650°C'de 100 ve 316 dakika süreyle yaşlandırılmış numunelerin I_r değerleri çok küçük (10^{-5} A/cm²'den az) bulundu. Bunların I_r/I_a oranları sırasıyla % 0.027634, % 0.033428 ve % 0.058928'dir. Bu verilere göre mikroyapıları birincil ferrit ve östenitten oluşan bu numunelerin hassaslaşmadığı kabul edilebilir.

Buna karşın, diğer tüm sıcaklıklarda ve değişik sürelerle yaşlandırılmış numunelerde I_r 'ın 10^{-2} A/cm² düzeyine ve hatta I_a 'e yakın

değerlere ulaştığı görüldü. Bunun sonucunda elde edilen yüksek I_r/I_a oranlarının gösterdiği korozyon ve hassaslaşmanın, krom ve molibdenle fakirleşmiş bölgelerden kaynaklandığı sonucuna varıldı. Bu numunelerde mikroyapının birincil ferrit ve östenit ile sigma ve yerel krom fakirleşmesi sonucu oluşan ikincil östenitten oluştuğu görüldü.

Yüksek sıcaklıklarda yaşlandırılan numunelerde hassaslaşma için gereken süre daha kısadır. Buna göre 725°C'de 1000 dakika ve 800°C'de 316 dakika yeterli iken 650°C'de hassas yapının oluşması en az 10000 dakika gerektirdi.

Anahtar Kelimeler: Dupleks paslanmaz çelikler, dupleks paslanmaz çeliklerde çökme, dupleks paslanmaz çeliklerde kristallerarası korozyon, elektrokimyasal potansiyodinamik reaktivasyon tekniği.

To My Family

ACKNOWLEDGEMENTS

I would like gratefully to express my sincere thanks to Prof. Dr. Mustafa Doruk for his enthusiastic supervision, excellent guidance and kindness throughout this study. I appreciate to him who is a model scientist and a virtuous person.

I thank to Prof. Dr. M. Kadri Aydınol for his supervision during the experimental work. I am indebted to him also for his support, insightful vision and encouraging conversations.

I would like to thank to Prof. Dr. Rafet Arıkan for his advices, guidance and positive attitude throughout the study.

I am forever grateful to my parents Ayşe-Rafet Arıkan, my sisters Esra Atbakan and Zehra Arıkan and my brother Ahmet Enes Arıkan for their endless understanding, patience and support throughout my life.

Special thanks to Aytek Çetin for his support and friendship.

Finally, I would like to thank the technical staff of METU, Department of Metallurgical and Materials Engineering, especially Cengiz Tan and Necmi Avcı.

TABLE OF CONTENTS

PLAGIARISM.....	iii
ABSTRACT.....	iv
ÖZ.....	vi
DEDICATION.....	viii
ACKNOWLEDGEMENTS.....	ix
TABLE OF CONTENTS.....	x

CHAPTER

I. INTRODUCTION.....	1
II. LITERATURE SURVEY	4
II.1. Austenitic Stainless Steels.....	4
II.1.1. Delta Ferrite.....	5
II.1.2. Sensitization	6
II.1.3. Sigma, Chi and Laves Phases	11
II.2. Ferritic Stainless Steels	12
II.2.1. Ferritic Stainless Steels with More Than 14% Chromium.....	12
II.2.2. Intermetallic Phases	13
II.2.3. Sensitization	15
II.3. Duplex Stainless Steels	17
II.3.1. Structure and Development of Duplex Stainless Steels	17
II.3.2. Super Duplex Stainless Steels	24
II.4. On the Mechanism of Electrochemical Corrosion.....	25
II.5. Corrosion Behaviour of Active-Passive Metals	31
II.6. Techniques for Measuring Susceptibility to Corrosion.....	40
II.6.1. Standard Test Methods for Detecting Detrimental Intermetallic Phases in Duplex Stainless Steel (ASTM A923-03)	40
II.6.2. Electrochemical Potentiostatic Reactivation Test (EPR)	43

III.	EXPERIMENTAL WORK	48
III.1.	Materials and Specimen Preparation.....	48
III.2.	Testing Equipment.....	50
III.2.1.	DLEPR Test	50
III.2.2.	Oxalic Acid Etch Test	52
III.2.3.	X-Ray Diffractometer	53
III.3.	Experimental Procedure	53
III.3.1.	Oxalic Acid Etch Test	53
III.3.2.	Sodium Hydroxide Etch Test	53
III.3.3.	DLEPR Test	54
III.3.4.	Weight Loss Test.....	55
III.3.5.	Metallography	55
IV.	RESULTS AND DISCUSSION.....	57
IV.1.	Metallography.....	57
IV.1.1.	Microstructural Evolution at 650 °C Ageing.....	58
IV.1.2.	Microstructural Evolution at 725 °C Ageing.....	62
IV.1.3.	Microstructural Evolution at 800 °C Ageing.....	66
IV.2.	Phase Volume Fraction By Light Optical Microscopy	70
IV.3.	Isothermal Sigma Phase Formation	74
IV.4.	Weight Loss Test.....	79
IV.5.	The Effect of Microstructural Changes on Corrosion.....	84
IV.6.	EDS Analysis of Phases.....	88
IV.7.	X-Ray Diffraction Pattern.....	92
IV.8.	DLEPR Results	97
IV.8.1.	DLEPR Test Results for Sample Solution Annealed at 1050 °C for 1 hr	102
IV.8.2.	DLEPR Test Results for Samples Aged at 650 °C.....	103
IV.8.3.	DLEPR Test Results for Samples Aged at 725 °C	105
IV.8.4.	DLEPR Test Results for Samples Aged at 800 °C.....	106
IV.8.5.	Micrographs of DLEPR Test Samples.....	107
IV.9.	Analysis of Polarization Curves in Reverse Scanning	112
V.	CONCLUSIONS	118
VI.	REFERENCES.....	120

CHAPTER I

INTRODUCTION

Generally duplex stainless steels are Fe-Cr-Ni alloys having an approximately volumetric fraction of 50% ferrite and 50% austenite in their microstructures. Their main feature is that they compromise the favorable corrosion resistance of austenitic stainless steels with good mechanical properties [1-4].

However duplex stainless steels are susceptible to sensitization due to the precipitation of additional phases when heated in a temperature range of 600-900°C. These phases affect the corrosion and mechanical properties. The sensitization temperature is often reached during isothermal heat treatment of fabricated components for stress relief, prolonged service at high temperatures, slow cooling from higher temperatures (i.e. solution annealing or during shut down of plant operating at higher temperatures), improper heat treatment in the heat affected zone (HAZ) of the weldments, or hot working of the material [5-9].

Undesirable phases such as intermetallic phases (sigma and chi), carbides and nitrides may exist in the steel if the manufacturing processes are not carefully controlled. Large amounts of elements stabilizing ferrite, such as chromium, molybdenum and silicon, can

promote the formation of sigma phase (σ). Sigma phase is a hard, brittle intermetallic phase, which is generally formed between 600 and 950 °C with rapid formation kinetics [10-12]. Additional phases found in duplex stainless steels can include chi (χ), R and α' [13]. χ -phase belongs to the topologically close-packed (TCP) phases. It frequently occurs in steels, as a ternary compound containing Fe, Cr and Mo, according to the composition $\text{Fe}_{36}\text{Cr}_{12}\text{Mo}_{10}$ [14]. The nucleation sites for σ - and χ -phases are grain boundaries, incoherent twin boundaries and dislocations. It is well established that the precipitation of these phases leads to a reduction of the creep ductility. It has also a reverse effect on the toughness and corrosion properties [11, 12]. A substantial depletion of solid solution strengtheners (like Cr, Mo, C and N) mainly due to a copious precipitation of the σ and χ -phases results in a decrease of the corrosion properties [15].

There are several test methods for determining the sensitization to intergranular corrosion. Weight loss acid test was first standardized and the test procedure was presented in ASTM A262-91 [16]. Corrosion rate is determined by measuring the weight loss of the sample. Another test method of measuring the degree of sensitization to intergranular corrosion involves electrochemical reactivation of the steel samples as defined in ASTM G108-94 [17]. This reactivation process is named as electrochemical potentiokinetic reactivation (EPR) and has been developed in single loop (SLEPR) or in double loop (DLEPR) types.

In this study, DLEPR was applied for the determination of susceptibility to sensitization in duplex stainless steel type UNS 31803 with 22% Cr grade. It is designated by X2CrNiMo 22-5-3 with the trade name of SAF2205. The summary of technical literature related to austenitic-ferritic duplex stainless steels show that the electrolyte often

consists of sulphuric acid (H_2SO_4) solution with the addition of KSCN as depassivator.

The purpose of the present work was to investigate intergranular corrosion behavior of DSS in relation to the influence of the microstructure produced by the different heat treatments. Electrochemical measurements were used to determine the degree of sensitization (DOS) to intergranular corrosion. SEM and light optical microscopy (LOM) were used to identify the different phases that form in bulk material after the heat treatments. XRD technique and EDS analysis were used for microstructural evolution. Surfaces obtained after the DLEPR test and the weight loss immersion test were also observed to check the attack locations and the relationship with the chromium depleted areas.

CHAPTER II

LITERATURE SURVEY

II.1. AUSTENITIC STAINLESS STEELS

The 300 series represents the largest category of stainless steels. It represents compositional modifications of the classic 18/8 (18%Cr-8% Ni) stainless steel, which has been a popular corrosion-resistant material for years. The following compositional modifications improve corrosion resistance: (a) addition of molybdenum, or molybdenum plus nitrogen, improve pitting and crevice corrosion resistance, (b) lowering the carbon content or stabilizing with either titanium or niobium plus tantalum reduce intergranular corrosion in welded materials, (c) addition of nickel and chromium improve high-temperature oxidation resistance and strength, and (d) addition of nickel improves stress corrosion resistance.

Compositional variations in the 300 series include a low carbon grade (L), a nitrogen-containing grade for increased strength (N), and a higher sulfur grade for improved machinability (F), as well as the higher carbon grade (H). In types LN, the loss in strength resulting from lowering of the carbon content is compensated for by addition of the strengthening element nitrogen. The resulting stainless steels are nitrogen-strengthened L grades that are resistant to sensitization, since

nitrogen at the level used (0.10-0.16%) does not produce sensitization in the austenitic stainless steels. In the nuclear grade (NG) variants of types, which have been used for boiling water nuclear reactor piping, the carbon content is kept below 0.02%(max.), which is below the 0.03% (max.). An extra high nitrogen grade (Hi)N is also available with 0.15-0.30% nitrogen. Type LMN is a low-carbon (L) grade containing higher levels of molybdenum (M) and nitrogen (N). Type B has a higher silicon content and greater oxidation resistance in high-temperature applications.

II.1.1. Delta Ferrite

Relating the compositions of the 300 series of austenitic steels to the Schaeffler diagram by calculating the nickel and chromium equivalents shows that the compositions of these steels are balanced to minimize the formation of delta ferrite. This phase is rich in chromium and other ferrite-stabilizing elements and lean in nickel and austenite-stabilizing elements. It is undesirable from a steelmaker's point of view because it causes difficulty in hot working [18]. The presence of delta ferrite is known to decrease pitting resistance. When present as isolated ferrite grains in significant quantities, as in duplex stainless steels, it markedly improves resistance to sensitization and stress corrosion cracking. However, it can decrease resistance to sensitization when present as a continuous grain boundary network. Long-term exposure of delta ferrite at elevated temperatures can lead to its transformation to sigma - a hard, brittle phase that can reduce ductility, toughness, pitting resistance, and crevice corrosion resistance.

For these reasons, the modern 300 series of austenitic stainless

steels usually contain sufficient nickel or its equivalents to avoid the presence of significant amounts of delta ferrite. However, some delta ferrite is intentionally allowed to be retained in weld metal and in castings, where its presence reduces hot tearing [18], or in special duplex stainless steels (e.g., type 329) in which wear resistance can be improved by intentionally heat treating to transform it to the hard sigma phase [19].

II.1.2. Sensitization

The exposure of austenitic stainless steels to elevated temperatures for long periods of time can result in the formation of various precipitates. The formation of such precipitates is generally described in the metallurgical literature by time-temperature-precipitation (TTP) diagrams. A TTP diagram for type 316 stainless steel is shown in Figure II-1 [20], where it is seen that carbide ($M_{23}C_6$) Chi, Laves phase, and sigma can be precipitated at certain elevated temperatures. Figure II-1 also shows that the precipitation of $M_{23}C_6$ carbide can occur in relatively short times or at relatively fast cooling rates compared to the other precipitates. Carbide precipitation can give rise to a phenomenon known as "sensitization." which can cause intergranular corrosion in certain environments.

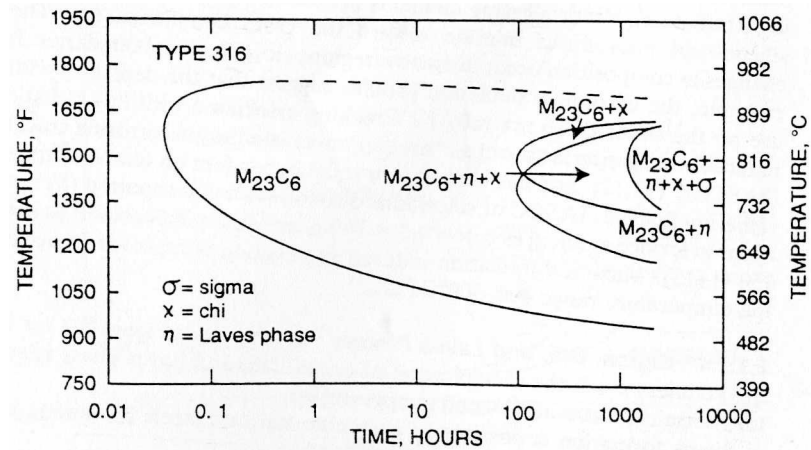


Figure II-1. Time-temperature-precipitation diagram for type 316 stainless steels containing 0.066%C [20].

To understand this phenomenon in terms of microstructure, it is instructive to examine the equilibrium relationships and carbon solubility in the Fe-18Cr-8Ni alloy, illustrated in Figure II-2 [21].

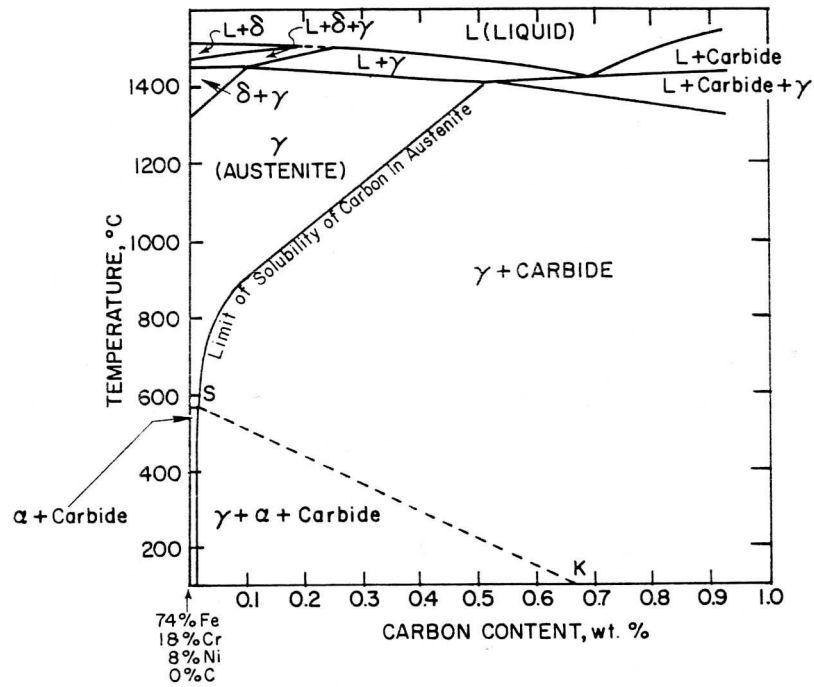


Figure II-2. Pseudo-binary phase diagram for an Fe-18%Cr-8%Ni alloy with varying carbon content [21].

This figure shows that in alloys containing between about 0.03 and 0.7% carbon, the equilibrium structure at room temperatures should contain austenite, alpha ferrite, and carbide ($M_{23}C_6$). In commercial alloys containing various austenite stabilizers, the reaction;



(at line SK) is too slow to take place at practical rates of cooling from elevated temperatures.

The same applies to the reaction;



at carbon contents below approximately 0.03%. For commercial purity materials, the transformation of austenite to alpha ferrite is ignored in practice, and in considering carbon solubility in austenite, the simplified diagram, as shown in Figure II-2, is often considered as being representative of real (i.e., nonequilibrium) situations [22]. In terms of this simplified diagram, austenite containing less than about 0.03% carbon should be stable. Austenite containing carbon in excess of 0.03% should precipitate $M_{23}C_6$ on cooling below the solubility line.

However, at relatively rapid rates of cooling, this reaction is partially suppressed. This is the case in practice when type 304 stainless steel containing more than 0.03% carbon is heat treated at 1050 °C, to remove the effects of cold work or hot work, and cooled at a fairly rapid rate to room temperature. While some carbide may have precipitated on cooling, the room-temperature austenite is still largely supersaturated with respect to carbon.

If this supersaturated austenite is reheated to elevated temperatures within the $\gamma+M_{23}C_6$ field, further precipitation of the chromium-rich $M_{23}C_6$ will take place at the austenite grain boundaries. Certain time-temperature combinations will be sufficient to precipitate this chromium-rich carbide but insufficient to rediffuse chromium back into the austenite near the carbide. This will result in the formation of envelopes of chromium-depleted austenite around the carbide [23, 24]. Since the carbides precipitate along grain boundaries, the linking of the chromium-depleted envelopes provides a continuous path of lower corrosion resistance along the grain boundaries for the propagation of intergranular corrosion or stress-corrosion cracking. This type of structure is known as "sensitized," irrespective of whether the chromium depletion has been caused by slow cooling, heat treatment, elevated temperatures service or welding. Sensitization also occurs in

ferritic and martensitic stainless steels.

The metallurgical remedies used to reduce sensitization in austenitic stainless steels include (i) the use of low-carbon (0.03% maximum) grades of stainless steel (i.e., types 304L, 316L, and 317L), (ii) postweld heat treatment to rediffuse chromium back into the impoverished austenite, and (iii) the use of titanium additions (type 321) or niobium plus tantalum additions (type 347) to precipitate the carbide at higher temperatures so that little carbon is left to precipitate as the chromium-rich grain boundary carbide during cooling. Types 321 and 347 are sometimes given a stabilizing treatment at 900-925°C to ensure maximum precipitation of carbon as titanium or niobium carbides. All these remedies have certain advantages and disadvantages. Thus postweld heat treatment is not always practical in large structures.

Other sensitization studies related to the nuclear power industry suggest that at boiling water reactor operating temperatures of about 288°C, the combined effects of the elevated temperatures and radiation can cause chromium depletion at the grain boundaries in type 304 stainless steels and nickel-base alloys [25]. In this radiation-assisted phenomenon there is no precipitation of chromium carbide, and the chromium depletion is thought to occur by a process known as "radiation-induced" segregation. During the irradiation of an alloy, some constituents of the alloy migrate toward point defect sinks such as grain boundaries or dislocation lines, and other constituents migrate away. This nonequilibrium segregation during irradiation was predicted in 1971 and has subsequently received considerable attention [26].

In austenitic stainless steels, this segregation causes depletion in the chromium levels and enhancement in the nickel levels near grain boundaries during irradiation. Minor alloying elements are also

redistributed; for example, silicon and phosphorus migrate toward the grain boundaries [25]. These changes in composition occur in narrow regions close to grain boundaries.

II.1.3. Sigma, Chi, and Laves Phases

As shown in Figure II-2 for type 316 stainless steel, the precipitation of sigma, chi, and Laves phase requires long-term exposure at elevated temperatures.

Sigma formation is possible in austenitic stainless steels containing more than 16% chromium and less than 32% nickel [27]. The sigma phase has a complex tetragonal structure with 30 atoms per unit cell and has broad composition and temperature ranges of stability that vary with alloy systems [28]. In Fe-Cr alloys it is given the formula FeCr, which is expanded to $(\text{FeNi})_x(\text{CrMo})_y$ in the Fe-Cr-Ni-Mo alloys such as type 316. Its composition in type 316 is 55%Fe-29%Cr-5%Ni-11%Mo [20]. From a corrosion viewpoint, this amount of chromium and molybdenum would make sigma cathodic (noble) with respect to the type 316 matrix. The detrimental effect of sigma on pitting resistance and crevice corrosion resistance is caused by chromium and molybdenum depletion in the surrounding matrix.

Sigma forms very slowly in the 300 series of stainless steels, first developing at grain boundaries. Its formation is favored by high chromium contents, silicon, molybdenum, titanium, small grain size, and cold work [29]. The presence of the sigma phase increases hardness, but it decreases ductility, notch toughness, and localized corrosion resistance. However, because of its slow rate of formation, sigma is usually a service problem where long exposures at elevated temperatures are involved. Sigma can be redissolved by heating to

temperatures of 1050°C or above. The Chi and Laves phases have received less attention than the sigma phase [28, 29]. However, the compositions of chi (52%Fe-21%Cr-22%Mo-5%Ni) and Laves phase (38%Fe-11%Cr-45%Mo-6%Ni) formed in type 316 stainless steel [20, 30] show that they have much higher molybdenum contents than the type 316 matrix. Hence, loss of pitting and crevice corrosion resistance due to molybdenum depletion in the surrounding matrix is a possibility. As in the case of sigma, these phases can also be redissolved by heating to temperatures of 1050°C or above.

II.2. FERRITIC STAINLESS STEELS

II.2.1. Ferritic Stainless Steels With More Than 14% Chromium

Type 430 is the basic 17%Cr ferritic stainless steel. In the past, type 430 was the multipurpose ferritic stainless steel, with a range of chromium content between 14 and 18%. Specifying chromium on the low side improved weldability, impact resistance, strength, and hardness, but with some sacrifice in corrosion resistance. With chromium on the high side, there was a gain in corrosion resistance, particularly in nitric acid, but a loss in mechanical properties, particularly impact strength. Later specifications narrowed the chromium range of type 430 to between 16 and 18% and identified the grade with chromium in the range of 14 to 16% as type 429. Type 429 subsequently became the bar and plate grade, with better weldability than type 430.

Types 430F and 430FSe contain a minimum of 0.15% of sulfur and selenium, respectively, to impart free-machining characteristics.

Both grades are suitable for automatic screw machine operations.

Type 434 contains molybdenum for increased resistance to pitting. Types 436 and 439 are the stabilized grades of types 434 and 430, respectively. Type 439 has been used for hot water tanks and water systems. Types 442 and 443 have higher chromium contents than type 430, with type 443 containing copper for sulfuric acid resistance. Type 444 is the highest molybdenum grade of the 400 series of ferritics and is also stabilized. Type 446 is the highest chromium grade in the ferritic 400 series and has the highest corrosion and oxidation resistance of this series. Nitrogen, niobium, aluminum, and titanium can be added to restrict grain growth.

The ferritic stainless steel containing 26%Cr and 1%Mo was originally introduced as a low interstitial ($\%C + \%N < 0.01\%$) material produced by electron beam melting of high-purity materials. It was designated as S44625 and has now been discontinued. Current alloys in this category are either produced by AOD (Argon Oxygen Decarburization) process and stabilized with titanium (S44626) or vacuum melted using high-purity materials and stabilized with niobium (S44627), and have been used to handle caustic soda.

The ferritic structure in these stainless steels introduces a number of complications of a metallurgical nature that can influence corrosion behavior. Among the metallurgical problems encountered in ferritic stainless steels are the ductile-to-brittle transition, 475°C embrittlement, precipitation of intermetallic phases, high-temperature embrittlement, low ductility of the welded condition, and sensitization.

II.2.2. Intermetallic Phases

Like austenitic stainless steels and austenitic higher alloys,

ferritic stainless steels can also precipitate the intermetallic sigma, chi, and Laves phases. Figure II-3 shows the region of temperatures and compositions over which sigma is an equilibrium phase in the binary iron-chromium system. In the lower-chromium 400 grades of ferritics, sigma forms very slowly and is usually a service problem when long exposures at elevated temperatures are involved. Increasing chromium and molybdenum contents favor the formation not only of sigma, but also of chi and Laves phases [31]. Because of their high chromium and molybdenum contents, the superferritic grades are particularly prone to the precipitation of these intermetallics. The time-temperature-precipitation diagram for Monit superferritic stainless steel (C:0.25, Cr:24.5-26, Ni:3.5-4.5, Mo:3.5-4.5, Ti+Nb:0.3-0.6, Mn:1.00) is shown in Figure II-4 [32], where it is seen that relatively rapid cooling rates are needed after heat treatment or welding to avoid the precipitation of intermetallics. Reheating to 1050 °C will redissolve these intermetallics.

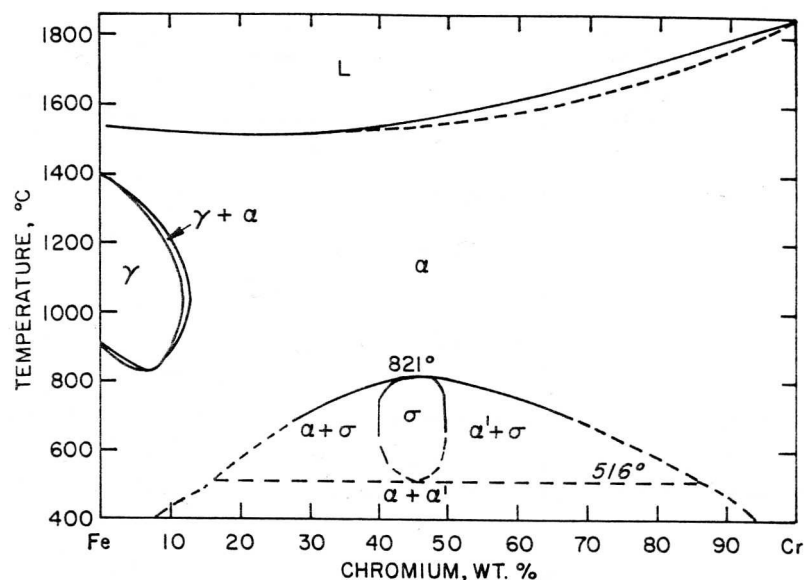


Figure II-3. Iron-chromium equilibrium diagram [33].

It should also be noted here that heating high-chromium ferritic stainless steels containing moderate to high levels of interstitial elements to 1000°C and above can result in extreme loss in toughness and ductility at room temperature. This effect, termed "high-temperature embrittlement," has been reviewed [34] and is thought to be caused by the precipitation of carbonitrides.

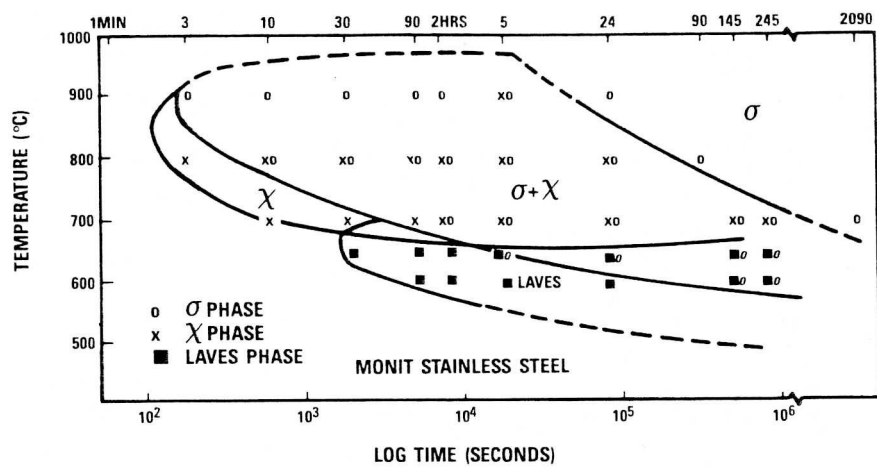


Figure II-4. Time-temperature-precipitation diagram for Monit superferrous stainless steel. Aged after a solution treatment at 1000°C for 10 min and water quenching [32].

II.2.3. Sensitization

Ferritic stainless steels, like the austenitic grades, can exhibit susceptibility to intergranular corrosion after certain thermal treatments. However, this subject has received much less attention than the comparable phenomenon in austenitics. In the case of the ferritics, most of the studies have been concerned with type 430.

In attempting to understand the metallurgical structure that is susceptible to intergranular attack, it is instructive to examine Figure II.5 [21], which illustrates the phase relationships and carbon solubility in an Fe-18%Cr alloy. This figure shows that the alpha ferrite has a low solubility of carbon, which, if present in any significant quantities in solid solution at elevated temperatures, should precipitate as carbide on cooling. It is generally accepted that to sensitize type 430, the alloy must be heated to temperatures at which austenite forms, that is, above fine P-L in Figure II-5. Material that has been heated to this temperature range shows severe susceptibility to intergranular attack (even in water), irrespective of whether it is water quenched or air cooled to room temperature. Thus, welds and portions of the heat-affected zone that have experienced temperatures above line P-L in Figure II-5 are susceptible to intergranular attack. Reannealing the sensitized material at approximately 800°C will eliminate this susceptibility.

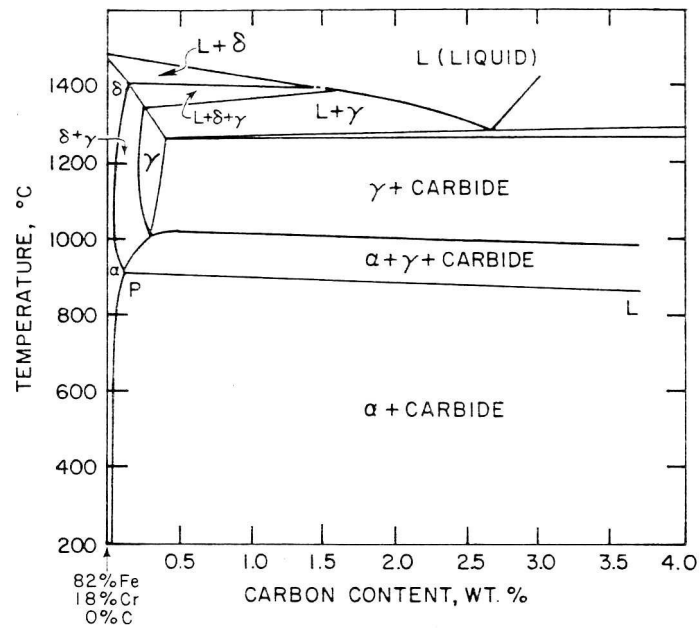


Figure II-5. Pseudo-binary phase diagram for an Fe-18%Cr alloy with varying carbon content [21].

II.3. DUPLEX STAINLESS STEELS

II.3.1. Structure and Development of Duplex Stainless Steels

The duplex steels are based on the ternary Fe–Cr–Ni phase diagram (Figure II-6). The section at 70% iron shows the quasi-binary phase diagram (Figure II-7), which represents the duplex stainless steels. They solidify primarily as ferritic alloys and transform at lower temperatures by a solid state reaction partially to austenite. Hence, the austenite ferrite ratio is adjusted in a temperature upside 1000 °C. Preferable a ratio of 60–50% austenite is achieved.

Due to the high amount of alloying elements, the duplex stainless steels show a rather complex precipitation behavior. The effect on the mechanical and corrosive properties of several

precipitations might be extensive. This is enhanced by a differential distribution of the alloying elements in the ferritic and austenitic phase. Because of the higher diffusion rate of the ferritic phase, all technically relevant precipitations can be found here. Most hazardous concerning a possible embrittlement is a precipitation of the hexagonal nitrides (Cr_2N) in a temperature range of 700–900°C, the α' precipitation (475°C embrittlement) and the intermetallic sigma and χ -phase. The intermetallic precipitations are of greater interest, because besides their influence on the mechanical properties, the corrosive properties are influenced severely.

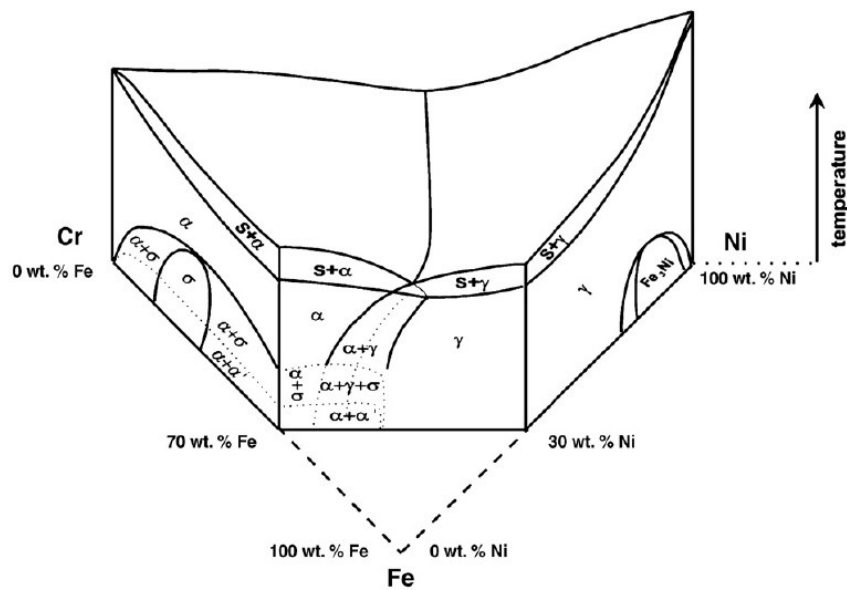


Figure II-6. Ternary Fe–Cr–Ni phase diagram.

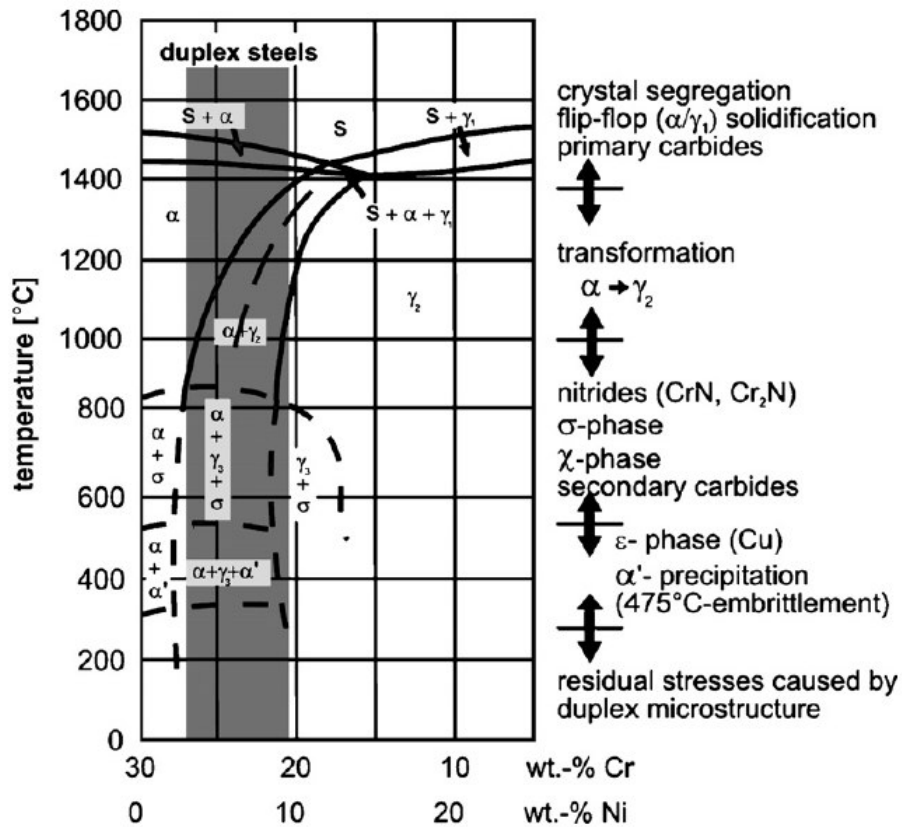


Figure II-7. Pseudo-binary Fe–Cr–Ni phase diagram at a 70% Fe section [35].

The phase diagram for a duplex stainless steel is shown in Figure II-7 [36]. This figure is a pseudo-binary diagram at 70% Fe [37]. The phase diagram shows that at 25% chromium the alloy will solidify as ferrite. Austenite precipitation will start at the $\alpha/(\alpha+\gamma)$ boundary, and the amount of austenite precipitated will depend on the cooling rate. Low cooling rates will enable more austenite to form. Commercial practice is to process or heat treat the alloy at temperatures in the range 1050-1150°C and to water quench to maintain a structure of about 50% ferrite and 50% austenite.

The first-generation duplexes, namely CD-4MCu and type 329,

do not contain nitrogen. In the welded condition, these grades form continuous regions of ferrite in the heat-affected zone, with a resultant reduction in toughness and corrosion resistance. While these properties can be restored by a postweld heat treatment to reform the austenite, the materials cannot be used in the as-welded condition.

The addition of the austenite-stabilizing element nitrogen causes the austenite to form from the ferrite at a higher temperature [38], with the result that an acceptable balance of austenite and ferrite forms in the heat-affected zone of the weld. The nitrogen content of the weld metal can be maintained by adding 5 vol% of nitrogen to the argon shielding gas during tungsten-inert gas welding of duplex stainless steels [39]. The nitrogen addition thus enables the duplex grade to be used in the as-welded condition.

The second-generation (i.e., nitrogen-containing) duplexes are marketed as proprietary products and are generally available only in the product forms produced by the supplier's mills. The duplex designed a 2205, however, is an exception. It is supplied by many producers and distributors in numerous product forms and is the most widely used duplex stainless steel. The total production of duplex stainless steels is quite small in comparison with the austenitics and ferritics.

It should also be noted here that the duplex stainless steels are capable of superplastic behavior, which is indicated by uniform large elongations without local necking in tensile deformation at temperatures near 0.5 of the melting point in absolute temperature (i.e., $\sim 1000^{\circ}\text{C}$). Structural superplasticity is highly favored by very small grains (e.g., 1-10 μm), which can be readily obtained due to the ferrite-to-austenite phase transformation.

The high strength of the duplex grades, together with their high

resistance to stress-corrosion cracking and resistance to sensitization-induced intergranular corrosion, has enabled their use in diverse applications. The duplexes have been used in power industry feedwater heaters and flue-gas scrubbers, in oil and gas production equipment; in chemical process industry heat exchangers, pressure vessels, tanks, valves and shafting; as liners for oceangoing tankers and chemical transport barges; and as tanks and piping in breweries [38]. The U.S. Navy has used the duplex stainless steels for catapult trough covers on aircraft carriers and for retractable bow plane systems on submarines.

II.3.1.1. Sensitization

The fact that sensitization of austenitic stainless steels could be eliminated by the introduction of ferrite to form a duplex alloy was first recognized in 1932 [40]. The mechanism of this beneficial effect has received considerable study [41]. The modern explanation [41, 42] of the observation that duplex stainless steels are highly resistant to sensitization can best be understood by considering the schematic shown in Figure II-8 [41]. This depicts the growth of an $M_{23}C_6$ carbide precipitate at an austenite-ferrite grain boundary and the corresponding chromium concentration profiles. Since chromium diffusion is about 100 times faster in the ferrite than in the austenite, the carbide grows much faster into the ferrite than into the austenite. Consequently, a very wide, shallow chromium-depleted zone develops on the ferrite side and a very narrow, deep chromium-depleted zone develops on the austenite side, as depicted in Figure II-8. Because the zone is so narrow on the austenite side, it can be quickly eliminated by minor rediffusion of chromium back into it. On the other side, the chromium at

the ferrite-carbide interface does not reach a sufficiently low level to cause intergranular corrosion.

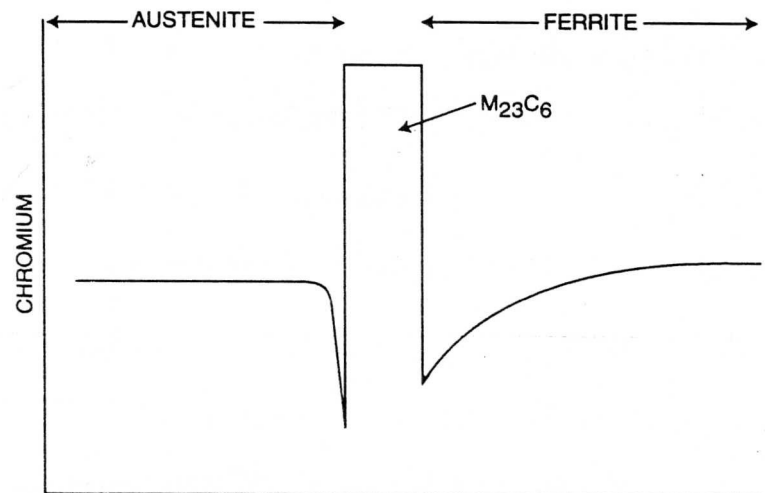


Figure II.8. Schematic chromium concentration profile at an austenite-ferrite interface containing $M_{23}C_6$ [41].

Carbides precipitated on austenite / austenite boundaries within the duplex stainless steel will exhibit the sensitization behavior characteristic of austenitic stainless steels. Therefore, to ensure high resistance to sensitization-induced intergranular corrosion, long, continuous austenite / austenite grain boundaries should be avoided in the microstructure of duplex stainless steels [41, 43].

II.3.1.2. Other High-Temperature Precipitates

In addition to the $M_{23}C_6$ carbide discussed in the previous

section, duplex stainless steels can precipitate chromium nitride, chi, sigma, and alpha prime (475°C embrittlement), as shown for 2205 duplex stainless steel in Figure II-9 [44]. Other studies using Uranus 50 [41] have also observed the presence of M_7C_3 carbide at temperatures of about 1000°C and the R-phase (Fe_2Mo) between 600 and 700°C. Sigma phase precipitation is facilitated by the addition of tungsten in the range 0-1% and is somewhat suppressed by tungsten additions in the range 1-3% [45].

The formation of the intermetallic phases, which is delayed due to the slower diffusion of substitutional elements required for their nucleation and growth, results in a depletion of chromium and molybdenum in austenite matrix [46, 47]. This causes a detrimental effect on the corrosion resistance, especially pitting, intergranular and crevice corrosion. Sigma (σ) phase with formula $FeCr$, which is more generally expanded as $(FeNi)_x(CrMo)_y$ is a severe problem due to its effect on the mechanical properties and localized corrosion resistance [48, 49]. It nucleates mainly on the grain boundaries. Laves (η) phase (Fe_2Mo) formation is observed after a minimum 10 hour at 750°C predominantly on dislocations. Chi (χ) phase with composition $Fe Cr Mo$ is a minor intermetallic phase found at 800°C for 10 hours.

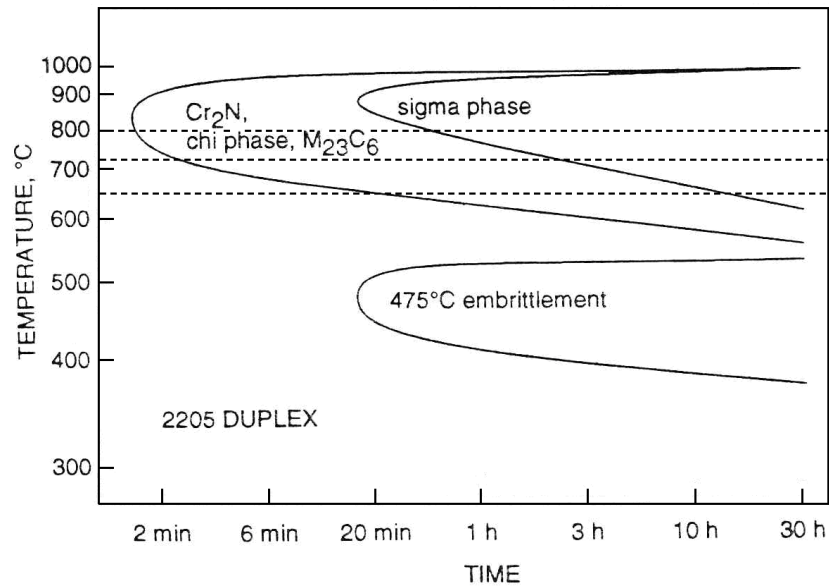


Figure II-9. Time-temperature-precipitation diagram for 2205 duplex stainless steel [44].

In duplex stainless steels, chromium nitride and sigma have been shown to provide sites for the initiation of crevice corrosion and sigma has been shown to reduce pitting resistance.

II.3.2 Superduplex Stainless Steels

The superduplex stainless steels are defined as those duplexes that have a PREN number equal to or greater than 40. These are the materials that contain the highest amounts of chromium, molybdenum, and nitrogen and hence have the highest pitting and crevice corrosion resistance.

Duplex stainless steels with PREN (pitting resistance equivalent number = %Cr + 3.3(%Mo) + 16(%N) (in weight %)) numbers-equal to or greater than 40 were originally needed to meet alloy composition

specifications for offshore oil rigs. However, both composition and microstructure can influence pitting and crevice corrosion resistance and time-temperature-precipitation diagrams are needed to define the effects of heat treatment and welding for these superduplex stainless steels.

II.4. ON THE MECHANISM OF ELECTROCHEMICAL CORROSION

The corrosion process consists of a set of redox reactions, which are electrochemical in nature. The metal is oxidized to corrosion products at anodic sites and general oxidation reaction is $M \rightarrow M^{+n} + ne^{-}$. This removes the metal atom by oxidizing it to its ion. All electrons generated by the anodic reactions are consumed by corresponding reduction reactions at cathodic sites of a corroding metal or at the cathode of an electrochemical cell. For example, one of the cathodic reactions is the reduction of hydrogen ions,



The anodic and cathodic reactions are controlled by the flow of the electrons through the metal. The transfer of electrons in these reactions is the corrosion current. As current flows, the anodic and cathodic potentials are displaced from the equilibrium or reversible values and approach each other. This process is called polarization. The polarization measurements are made with potentiostat which maintains the desired potential between the electrode being studied (working electrode) and reference electrode by passing the current between working and inert counter electrode. In a polarization diagram the first measurements is the corrosion potential when the applied current (I_{app}) is zero. When total rates of anodic reactions are equal to

the total rates of cathodic reactions, corrosion potential is called open circuit potential (E_{corr}), seen in Figure II-10. The current density at E_{corr} is called the corrosion current density (i_{corr}).

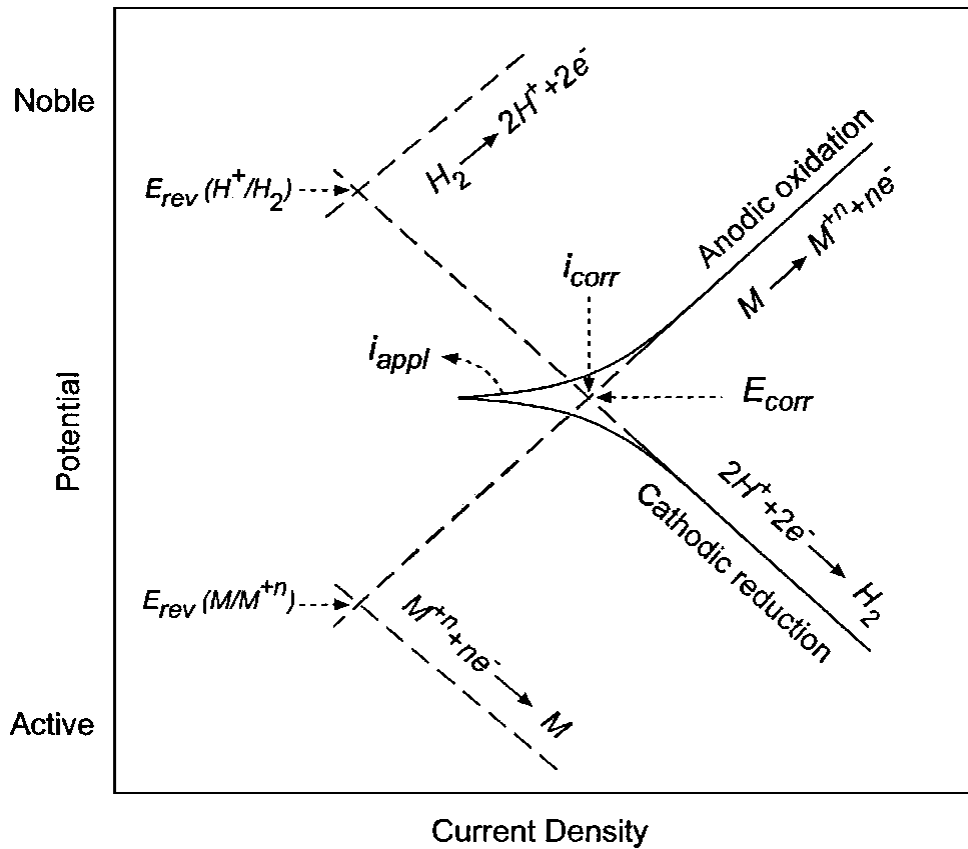


Figure II-10. Schematic illustration of applied potential vs current density.

When the applied potential is increased to more positive value (noble) than the specimen open circuit potential (E_{corr}), the specimen

behaves as anodic and metal dissolution reaction is realized as seen in Figure II-11. This is represented as anodic polarization curve. Anodic current density is proportional to the corrosion rate of metal. If the potential is increased, the rate of corrosion rises rapidly. This is the active range of the metal. If the potential is raised further, the corrosion will drop suddenly to a lower value, and then it will remain constant over a wide potential range. This is the passive range, in which a thin, invisible film of oxide covers the metal. This protective film acts as a barrier between the metal and its environment and reduces its rate of dissolution. If the potential is kept on increasing, corrosion rate will rise again. This is called the transpassive range.

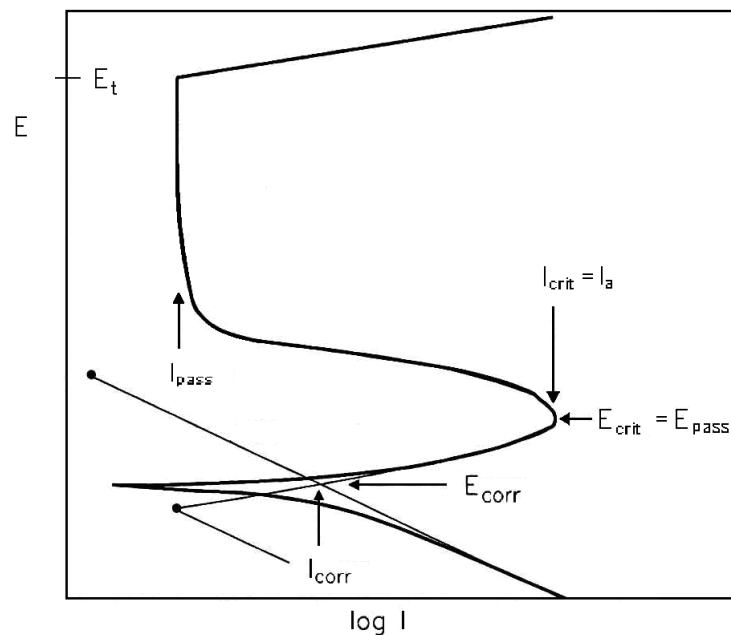


Figure II-11. Schematic anodic polarization curve.

The critical values on the anodic polarization curve are affected by the temperature and pH of medium. At higher temperatures and lower pH, critical current density (I_{crit}) increases. It means the transport to passive range can be realized difficultly. The passivation potential (E_{pass}) and passivation current density (I_{pass}) increase slightly as well [50].

Polarization curve changes from metal to metal depending on how the metal can easily be passivated. It can be seen in the Figure II-12 [51] the chromium is easily passivated since its passivation potential (E_{pass}) and critical current density (I_c) are lower. Also, chromium is passive over a broad range. However, iron has a higher critical current density and passivation potential. For nickel, anodic current changes continuously in the passive range and increases with a peak to transpassive range.

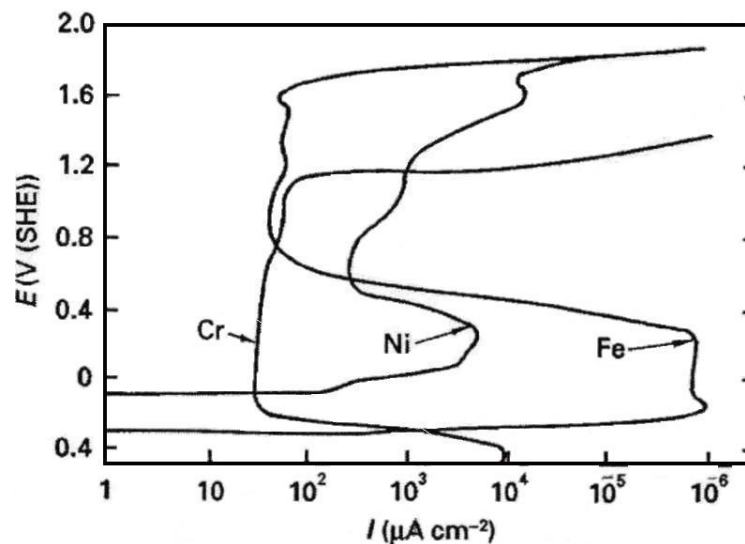


Figure II-12. Anodic polarization diagram of pure Cr, Ni and Fe in 1N H_2SO_4 [51].

As it is seen in Figure II-13 [52], molybdenum also contributes to passivity. Its polarization behavior is different compared to iron and nickel. Anodic current density of molybdenum does not increase steeply with the potential [19]. On the other hand, the corrosion potential of Fe18Cr14.3Ni2.5Mo alloy is nobler than chromium and iron but close to that of nickel and molybdenum and this is typical for austenitic alloys. As a consequence, it is shown that nickel and molybdenum are enriched on the surface of alloy during anodic polarization [53].

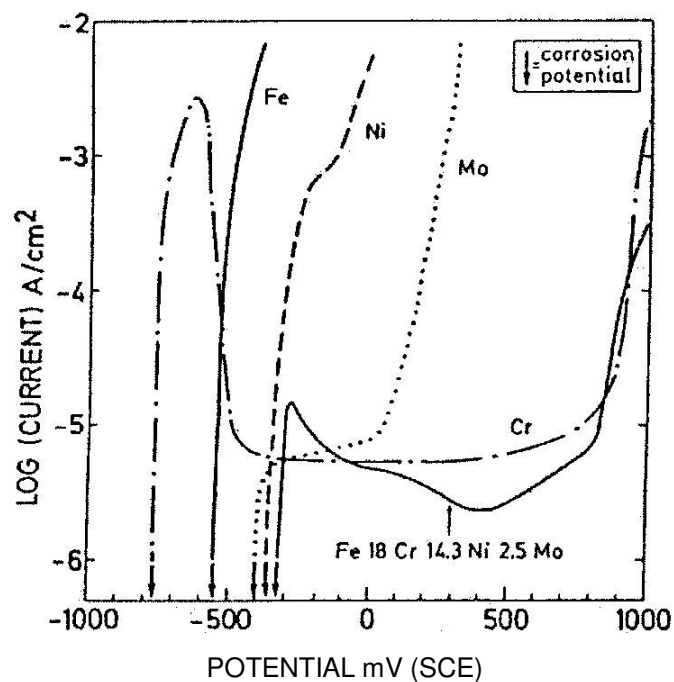


Figure II-13. Anodic polarization curves of pure metals, Fe, Ni, Cr, Mo and Fe18Cr14.3Ni2.5Mo (at%) austenitic stainless steel in 0.1 M HCl + 0.4M NaCl at 25 °C and 3mV/s [52].

Alloying the steel with both chromium and nickel accelerates the passivation. Even, addition of small amounts of molybdenum to Cr-Ni steels reduces the critical current density and also molybdenum alloyed steel is passive in broad potential range. Molybdenum also improves the pitting resistance of the steel especially in chloride environments. In solutions containing halogen ions, like chloride, polarization curve changes considerably. For example, passivation is realized more difficultly and the stability of passivation cannot be maintained, which is because of the aggressive attack of the chloride ion. In molybdenum containing stainless steels, it should be understood that, the formation of sigma and chi phases decreases the passive potential range because of chromium and molybdenum depletion in the matrix [54].

For explaining the nature of the passive film, there are mainly two theories, which are oxide film theory and adsorption, or electron configuration theory.

According to electron configuration theory, in stainless steels, iron can be transformed to passive state by sharing electron with chromium, which has stronger tendency to adsorb electron. Chromium with 5 vacancies in the 3d shell of the atom can share at least 5 electrons or can passivate 5 iron atoms. This proportion corresponds to 15.7 wt % chromium. That is, stainless Cr-Fe alloys are produced at critical minimum amount of chromium about 12% [55].

According to oxide film theory, a diffusion barrier layer of reaction products, which are metal oxide or other compounds, separates metal from its environment and slows down the rate of reaction. Its thickness and composition can change with alloy composition, electrolyte and potential. The passive film of austenitic stainless steel is presented as duplex layer, which consists an inner barrier oxide film and outer hydroxide film [53].

Main compounds in the passive film on Fe-Cr alloy are oxide products of chromium, although iron oxides generally predominate. The passive potential range consists of Fe^{+3} , Cr^{+3} and Fe^{+2} . Fe^{+3} oxide is reduced to Fe^{+2} hydroxide and finally to iron metal. Chromium stops the reduction of iron to metallic state and Cr^{+3} is not reduced, remains within the passive layer [56].

Nickel is oxidized only to a very low extent. Its positive influence is not in passive film, but in the underlying metal phase, it provokes passivability of the alloy. On the other hand, with molybdenum addition the passivity of stainless steel is improved and oxide product is enriched. Also, molybdenum in the alloy redissolves into solution and forms molybdenate ion, which adheres the surface to prevent the attack of chloride ions [57, 58].

Intergranular corrosion on Fe-Cr-Ni alloys is due to local deterioration of passive film. Thus, passive state of sensitive stainless steel is less stable than that of non-sensitive steel [59].

II.5. CORROSION BEHAVIOR OF ACTIVE-PASSIVE METALS

Corrosion behavior of active-passive metals can be explained on the basis of Evans diagram as shown in Figure II-14. If there are no strong oxidizing agents in the solution, the corrosion potential is E_{corr} , and the metal corrodes uniformly in a film-free condition. As the potential is raised in this active region (either by the application of an external current or by the introduction of oxidizing species into the environment), the dissolution rate of the metal increases until a potential of E_{pass} is reached. Above this passivation potential, a dramatic decrease in the dissolution rate occurs. Further increases in

potential usually have little effect on the passive current density, I_{pass} . In some cases, the difference between the critical anodic current density for passivation, I_{crit} (I_a), and I_{pass} can be over four orders of magnitude. These current densities are directly related to the dissolution rate of the material. Further increase in potential will eventually lead to an increase in the current due to a combination of oxygen evolution and transpassive dissolution of the passivating film for most metals. For the noble metals (e.g., aluminum, tantalum, lead, titanium), certain solutions will allow a thick, insulating oxide film to grow on which oxygen evolution does not occur. Under these conditions, anodization occurs. The electrochemical parameters that characterize passivity (E_{pass} , E_t , I_{crit} or I_a and I_{pass}) depend upon both the metal and the environment to which it is exposed.

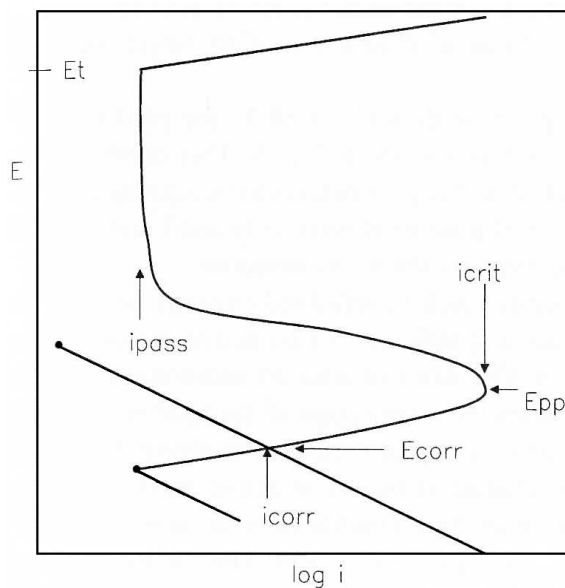


Figure II-14. Schematic Evans diagram for a material that undergoes an active-passive transition. Important parameters that characterize this behavior are identical.

In order to determine the corrosion state of an active-passive system, the position of the corrosion potential relative to E_{pass} must be determined. According to Figure II-14, if E_{corr} is below E_{pass} , the material will undergo uniform dissolution under film-free conditions. If E_{corr} is above E_{pass} but below E_t the material will be passive and will dissolve at its passive current density. Corrosion-resistant alloys (CRA) are designed to operate under such conditions. For situations in which E_{corr} is above E_t , the material will dissolve transpassively, i.e., uniformly.

As discussed before, the corrosion potential is determined by the intersection of the sum of the anodic Evans lines and the sum of the cathodic Evans lines. For active-passive materials, the only new wrinkle is the increased complexity of the anodic line. Since the anodic line is not single-valued with respect to current density, three distinct cases can be considered. In all cases, the condition $\Sigma I_a = \Sigma I_c$ determines the position of the corrosion potential (E_{corr}), and the condition $I_{\text{app}} = I_a - I_c$ determines the appearance of the polarization curve for each case. Thus the nature and kinetics of the cathodic reaction(s) are critical in determining the corrosion state and rate of dissolution of an active-passive material.

(a) Under reducing conditions (e.g., in acids such as HCl), the predominant cathodic reaction is hydrogen evolution as shown in Figure II-15. This combination results in a polarization curve in which all of the parameters characterizing passivity can be measured as shown in Figure II-15. If a material were to be used under these conditions, nothing would be gained from its ability to passivate.

(b) In the presence of oxidizing species (such as dissolved oxygen), some metals and alloys spontaneously passivate and thus exhibit no active region in the polarization curve, as shown in Figure II-16. The oxidizer adds an additional cathodic reaction to the Evans

diagram and causes the intersection of the total anodic and total cathodic lines to occur in the passive region (i.e., E_{corr} is above E_{pass}). The polarization curve shows none of the characteristics of an active-passive transition. The open circuit dissolution rate under these conditions is the passive current density.

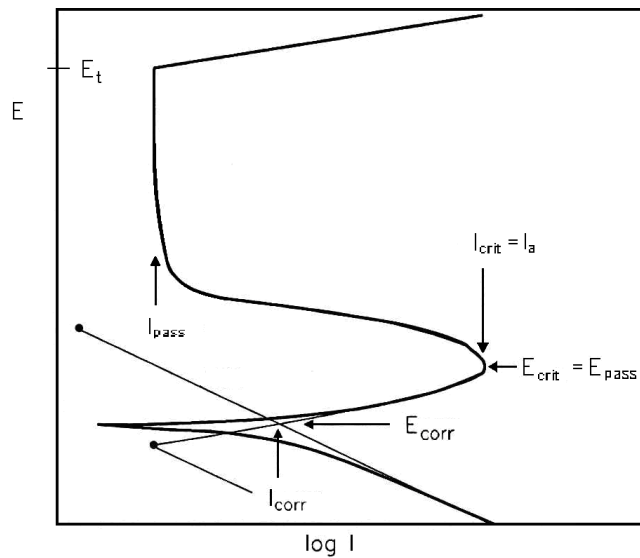


Figure II-15. Schematic Evans diagram and resulting potential-controlled polarization curve for a material that undergoes an active-passive transition and is in a reducing solution. The heavy line represents the applied current required to polarize the sample.

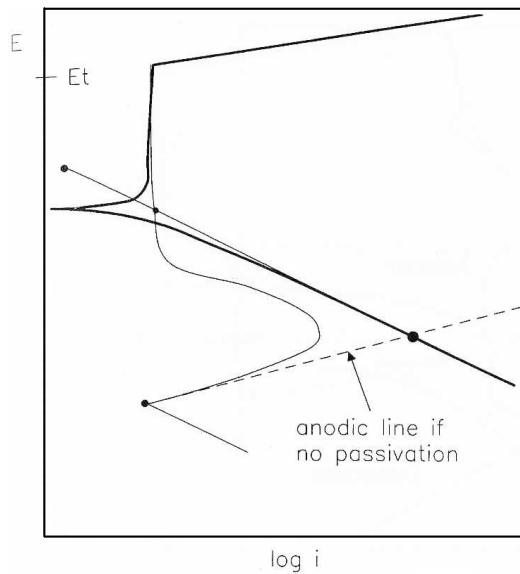


Figure II-16. Schematic Evans diagram and resulting potential-controlled polarization curve for a material that undergoes an active-passive transition and is in an oxidizing solution. The heavy line represents the applied currents required to polarize the sample. If the sample did not undergo an active-passive transition, it would corrode at a much higher rate in this solution, as is indicated by the intersection of the dotted line and the cathodic curve.

For the case shown in Figure II-17, the anodic and cathodic Evans lines intersect at three points. The polarization curve for this situation appears unusual, although it is fairly commonly observed with CRAs. At low potentials, the curve is identical to that shown in Figure II-15. However, just above the active-passive transition, another E_{corr} appears followed by a "loop" and yet a third E_{corr} before the passive region is observed. The direction (anodic or cathodic) of the applied current density for each region shown in the polarization curve of Figure II-17 is indicated, showing that the loop consists of cathodic current. The origin of the cathodic loop is the fact that at these

potentials, the rate of the cathodic reaction is greater than the passive current density (i_{pass}). Thus the net current is cathodic over that range of potential.

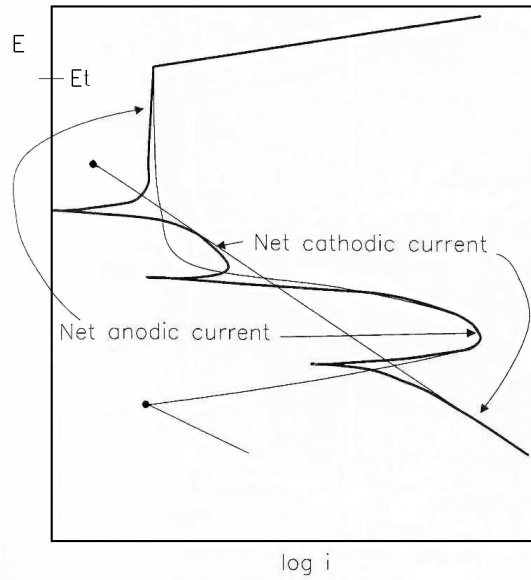


Figure II-17. Schematic Evans diagram and potential-controlled polarization curve for a material/environment combination that exhibits a cathodic loop. Note that the direction of the applied current changes three times in traversing the curve.

Generally, either the uppermost or lowermost E_{corr} is the most stable, and the material exhibits that corrosion potential spontaneously. Such cathodic loop behavior is often observed on the reverse scans of polarization curves in which pitting does not occur as shown in Figure II-18. During the initial anodic scan, the oxide is thickening and the anodic line is moving to the left. Thus, upon the return scan, the unchanged cathodic line now intersects the anodic line at several

places, leading to the appearance of cathodic loops. Cathodic loops do pose fundamental problems; they merely conceal the passive current density at potentials near the active-passive transition [60].

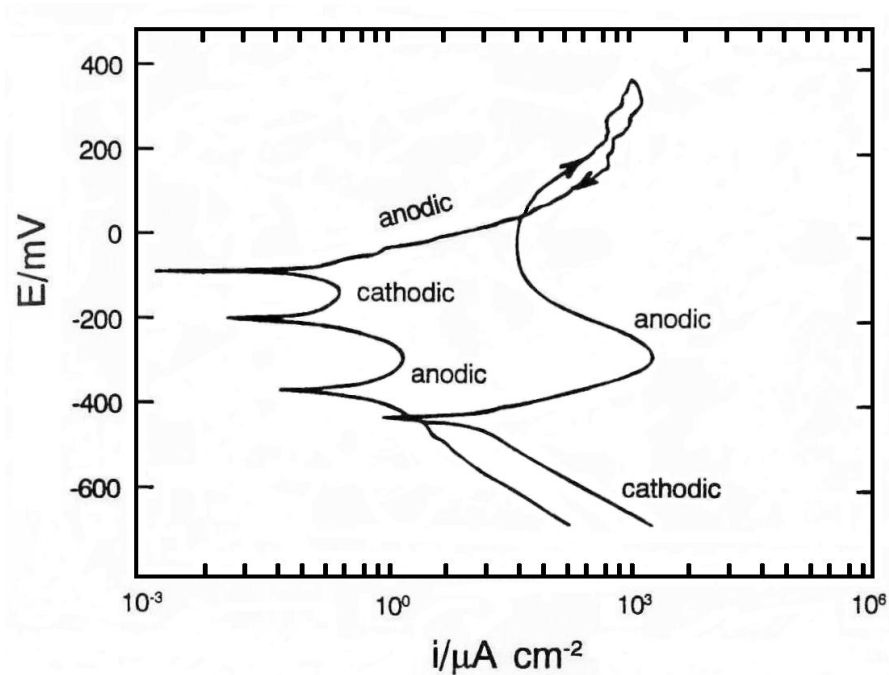


Figure II-18. Polarization curve for type 302 stainless steel in 0.5% HCl. Note the presence of a cathodic loop on return scan due to the greatly reduced passive current density. Also, note the lowered critical current density on the reverse scan due to incomplete activation of the surface [60].

The cathodic reaction kinetics thus play an important role in determining the corrosion state for an active-passive material. The introduction of additional cathodic reactions to an environment or the change in the kinetics of one already present can dramatically affect

the state of the material's surface. Figure II-19 shows schematically the effects of changes in the kinetics of a single cathodic reaction (modeled as changes in the exchange current density). From the different corrosion potentials established, one can see the key role of cathodic reaction kinetics in establishing the corrosion state of active-passive metals.

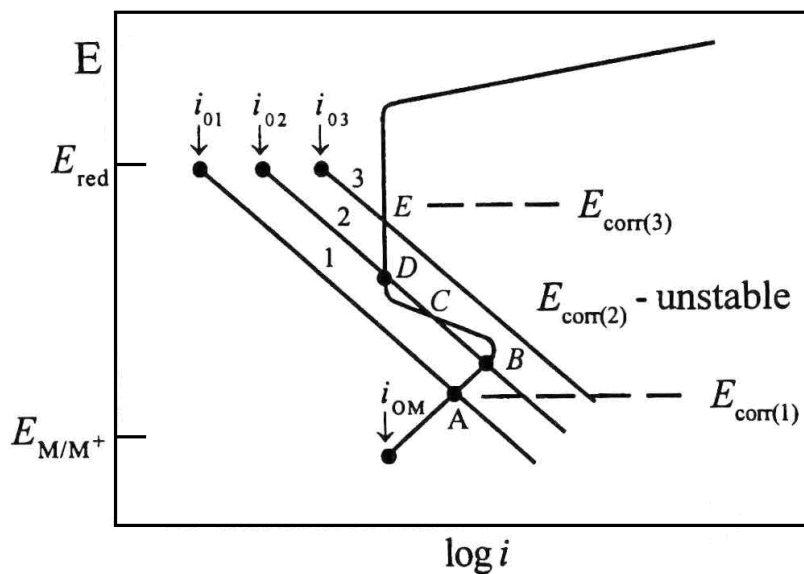


Figure II-19. Schematic Evans diagram illustrating the effect of a change in the cathodic reaction kinetics on the corrosion conditions. Case 1 would be representative of Figure II-15. Case 3 would lead to the polarization behavior described in Figure II-16. Case 2 would lead to the polarization behavior shown in Figure II-17.

Increasing oxidizer concentration increases the potential of the redox half-cell reaction according to the Nernst equation. The predictions of mixed potential theory are shown in Figure II-20 for an

active-passive alloy. As concentration increases from 1 to 2, corrosion rate, and corrosion potential increase from A to B as for a conventional metal or alloy. At concentration 3, the alloy may exist in either the active state at C or the passive state at D. The "negative resistance" portion of the anodic curve at the active-to-passive transition, where current decreases with increasing potential, is an artifact of the instrumental measurement and is sometimes indicated by a dashed line as shown. Thus, the point X is not a stable potential state and is never observed when passivity is established by dissolved oxidizers, in practice. As concentration increases to 4 and 5, only the passive state is stable, and the corrosion rate drops to the low passive values near D. Still further increases to 7 and 8 cause a transition to the transpassive state and corrosion rate increases to E and F [61].

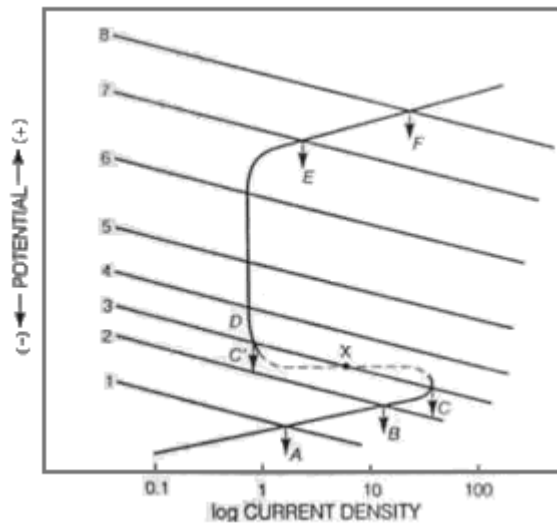


Figure II-20. Effect of oxidizer concentration on corrosion of an active-passive alloy.

II.6. TECHNIQUES FOR MEASURING SUSCEPTIBILITY TO CORROSION

For long time, before the electrochemical techniques were developed, and acid immersion tests have been used. Acid tests have simple principles that consist in subjecting the steel under examination to contact with a test medium. The purpose of the test medium is to attack the Cr-depleted zone in steel containing grain boundary carbide. Evaluation of corrosion rate is provided comparatively by visual, microscopic examinations and weight loss of the steel.

Intergranular attack is accelerated by potential differences between grain and grain boundaries, that is, attack is determined by availability of anodic sites at grain boundaries. Therefore, making it anodic passivates the specimen. At that time, the chromium depleted alloy sets up passive-active cell of appreciable potential difference, the grains (exhibit passive behavior) constituting large cathodic areas relative to small anode areas at grain boundaries (exhibit active behavior). During decreasing the potential, the protective passive film over Cr-depleted areas is more easily dissolved than that over undepleted (non-sensitized) surfaces.

II.6.1. Standard Test Methods for Detecting Detrimental Intermetallic Phases in Duplex Stainless Steel (ASTM A923-03)

The purpose of these test methods is to allow detection of the presence of intermetallic phases in duplex stainless steels to the extent that toughness or corrosion resistance is affected significantly [62]. These test methods will not necessarily detect losses of toughness or corrosion resistance attributable to other causes.

Duplex (austenitic-ferritic) stainless steels are susceptible to the formation of intermetallic compounds during exposures in the temperature range from approximately 320 to 955 °C. The speed of these precipitation reactions is a function of composition and thermal or thermo-mechanical history of each individual piece. The presence of these phases is detrimental to toughness and corrosion resistance.

Correct heat treatment of duplex stainless steels can eliminate these detrimental phases. Rapid cooling of the product provides the maximum resistance to formation of detrimental phases by subsequent thermal exposures.

Standard test methods include the following:

Test Method A: Sodium Hydroxide Etch Test for Classification of Etch Structures of Duplex Stainless Steels. The sodium hydroxide etch test may be used for the acceptance of material but not for rejection. This test method may be used with other evaluation tests to provide a rapid method for identifying those specimens that are free of detrimental intermetallic phases as measured in these other tests. The solution for etching is prepared by adding 40 g of reagent grade sodium hydroxide (NaOH) to 100 g of distilled water. The polished specimen should be etched at approximately 1 to 3 V dc, for 5 to 60 s.

The etch structures are classified into the following types:

Unaffected Structure: The ferrite has been etched without revelation of intermetallic phase. The interphase boundaries are smooth.

Possibly Affected Structure: The ferrite has been etched with isolated indications of possible intermetallic phase. The interphase boundaries may show a fine waviness.

Affected Structure: The indications of an intermetallic phase are

readily revealed before or simultaneously with the staining of the ferrite during etching.

Test Method B: Charpy Impact Test for Classification of Structures of Duplex Stainless Steels.

Test Method C: Ferric Chloride Acid Immersion Corrosion Test for Classification of Structures of Duplex Stainless Steels. This test method describes the procedure for conducting the ferric chloride corrosion test for detecting the presence of detrimental intermetallic phases in duplex stainless steels. The presence or absence of corrosion attack in this test is not necessarily a measure of the performance of the material in other corrosive environments; in particular, it does not provide basis for predicting resistance to forms of corrosion not associated with the precipitation of intermetallic phases. This test method does not determine the critical pitting temperature or test for the suitability for use in a particular environment. It is designed solely for detection of the precipitation of detrimental intermetallic phases in duplex stainless steels.

Before testing by the ferric chloride corrosion test, specimens of the steel may be given a rapid screening test in accordance with the procedures of Test Method A, "Sodium Hydroxide Etch Test for Classification of Etch Structures of Duplex Stainless Steels". Preparation, etching, and the classification of etch structures are described therein. Specimens having an etch structure described as "Unaffected Structure in Test Method A" will be essentially free of detrimental effects on pitting corrosion resistance as related to the formation of an intermetallic phase. Other mechanisms for loss of pitting resistance may occur independently but are beyond the scope of this test method. Specimens showing "Unaffected Structure in Test Method A" are acceptable with respect to the absence of intermetallic

phases and need not be tested by the ferric chloride corrosion test as described in Test Method C. All specimens having other than "Unaffected Structure" shall be tested by the ferric chloride corrosion test.

The test solution is prepared by dissolving 100 g of reagent-grade ferric chloride, $\text{FeCl}_3 \cdot 6\text{H}_2\text{O}$, in 900 ml of distilled water (approximately 6 % FeCl_3 by weight). The solution is filtered through glass wool or filter paper to remove insoluble particles. The pH of the test solution shall be adjusted to approximately 1.3 prior to beginning the test by the addition of HCl or NaOH, as required.

The corrosion rate is calculated in accordance with the weight loss and total surface area. Unless otherwise specified, the calculated corrosion rate shall not exceed 10 mdd. The corrosion rate is calculated in accordance with the following: corrosion rate (mdd) = weight loss (mg)/[specimen area (dm^2) x time (days)]. Tests are performed using FeCl_3 solution with a volume of 20 ml/ cm^2 at 25 ± 1 °C for 24 hours.

II.6.2 Electrochemical Potentiostatic Reactivation Test (EPR)

Several tests exist to determine the susceptibility of the material to intergranular corrosion, but most of them are destructive except the electrochemical potentiodynamic reactivation (EPR) test [63-66]. EPR test is based on the assumption that only sensitized grain boundaries become active, while grain bodies remain unsensitized. Accordingly this test provides the degree of sensitisation of the material by measuring the amount of chromium depleted areas which are zones adjacent to the precipitation of compounds that are rich in chromium. The test can be performed in single loop (SLEPR) or in double loop

(DLEPR) [67]. The latter has the advantage to be independent of the surface finishing. This test was first used for austenitic stainless steels. Few data are available concerning the susceptibility to intergranular corrosion of austeno-ferritic stainless steels using the EPR test. Moreover, the best advantage of this technique is that it obtains a quantitative value of the degree of sensitisation (DOS) [68].

II.6.2.1. Single Loop Test Method (SLEPR)

The single loop (SLEPR) test proposed by Clarke, et al., [69-71] is shown schematically in Figure II-21. It consists of first establishing the corrosion potential, E_{corr} of the specimen in the test solution of 0.5M H_2SO_4 + 0.01M KSCN. The alloy is then polarized to a potential of +200 mV vs. a saturated calomel electrode (SCE) for a period of 2 minutes. After this, the potential is decreased to its open circuit value, E_{corr} at a scan rate of 6 V/h (1.67 mV/s). The testing temperature is held at 30 ± 1 °C. The reactivation leads to the preferential breakdown of the passive film on the sensitized material where there is chromium depletion. As a result, a large loop is generated in the curve of the potential vs. current.

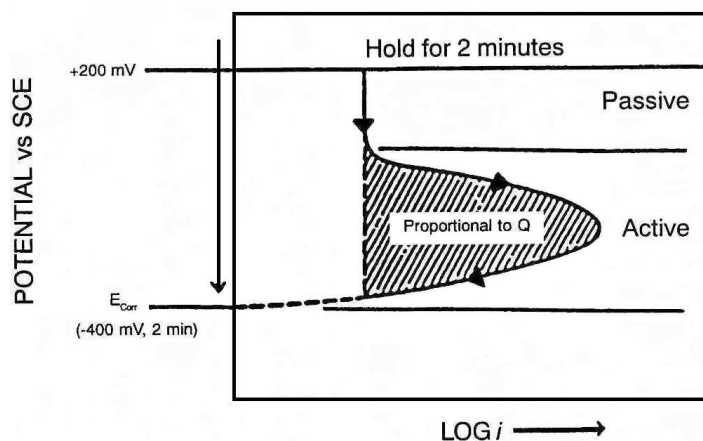


Figure II-21. Schematic diagram of SLEPR test method

The area under the loop is proportional to the electric charge, Q , where Q depends on the surface area and grain size. On nonsensitized material, the passive film remains essentially intact, and the size of the loop, and therefore, Q , are small. Clarke, et al., [69] normalized the charge, Q , by the total grain boundary area (GBA) by means of Equation (4) and used the normalized value of Q as an indicator of the degree of sensitization (DOS):

$$P_a = Q/\text{GBA} \text{ (coulombs/cm}^2\text{)} \quad (4)$$

$\text{GBA} = A_s[5.09544 \times 10^{-3} \exp(0.34696 X)]$, where A_s is the specimen surface area and X is the ASTM grain size number [80]. Equation (4) is based on certain assumptions which have been discussed elsewhere [72].

Although this test has been standardized, there are major difficulties in using single loop EPR test, which are, the necessity of measuring grain size and polishing with 1 μm diamond paste, since reactivation behavior is very sensitive to surface finish. This led to the development of a new procedure that is the double loop test method, which basically sets a reference state of sample's own.

II.6.2.2. Double Loop Test Method (DLEPR)

An improvement on the SLEPR test is the double loop, or DLEPR test. In this test, the reactivation scan from a potential in the passive range is preceded by a scan (anodic polarization) from the corrosion potential into the passive range. As a result, two "loops" are generated: an anodic loop and a reactivation loop (Figure II-22).

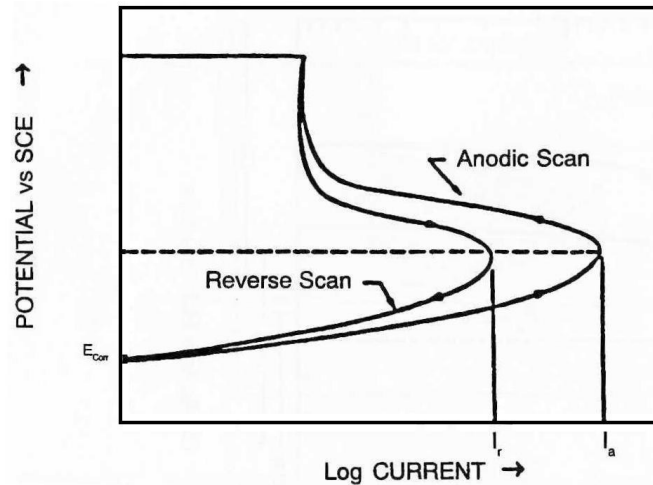


Figure II-22. Schematic diagram of double loop EPR test. Evaluation is by the ratio $I_r:I_a$.

Instead of using the area under the reverse scan-generated loop to measure sensitization, as is done in the single loop test, a ratio of the maximum currents generated in the two loops is used, $I_r:I_a$. This ratio of the two peak current densities is used as the degree of sensitization (DOS) indicator. During the anodic sweep, the entire surface is active and contributes to the peak current. During the

reactivation sweep, only the sensitized grain boundaries contribute to the passive-active transition. Thus in unsensitized specimens there is a small I_r and therefore a small ratio, while in heavily sensitized specimens, I_r approaches I_a . The principal advantage of this double loop test is that it is not necessary to polish the surface to be tested to a 1 μm finish. It has been claimed that a 100 grit (140 μm) finish is all that is needed to provide reliable results. In addition, it has been claimed that it is not necessary to normalize the ratio of maximum currents with a grain size factor, i.e., it would not be necessary to measure the grain size of the material being tested by means of microscopic examination of an etched surface.

CHAPTER III

EXPERIMENTAL WORK

III.1. MATERIALS AND SPECIMEN PREPARATION

The material used in this research is UNS31803 (X2CrNiMo22-5-3) type duplex stainless steel (trade name SAF2205). The chemical composition of the steel is given in Table III-1.

Table III-1. Chemical composition of 2205 DSS (wt%).

C	Cr	Ni	Mo	Mn	Fe
0.026	22.04	4.45	2.69	1.49	Ret.

The specimens were cut from a wrought cylindrical bar of 100 mm in diameter and 200 mm in length. The specimens were also in cylindrical shape of 10 mm in diameter and 20 mm in length. They were taken from the bar in an orientation parallel to the rolling direction. In order to homogenize the structure all specimens were subjected to a solution heat treatment at 1050°C for 1 hour and then quenched in

water. Then several heat treatments (ageing) were performed at 650°C, 725°C and 800°C for various times to develop different degree of sensitization. The applied heat treatments are given in Table III-2.

After heat treatments the specimens were remachined with CNC to remove oxide layer. Then a hole of 3.5 mm was drilled and an M4 thread was machined to connect a rod for anodic polarization test. The surfaces of the specimens were ground from 400 to 2000 grit emery paper. For microstructure examination, the bottom surfaces of the specimens were polished with 9 µm and 1 µm diamond paste.

Table III-2. Specimen codes and applied heat treatments.

Solution annealed at 1050°C for 1 hour and water quench				
Aging Heat Treatments	Ageing Time (minute)	Ageing Temperature (°C)		
		650°C	725°C	800°C
Solution annealed at 1050°C for 1 hour and water quenched				
	100	A-1	B-1	C-1
	316	A-2	B-2	C-2
	1000	A-3	B-3	C-3
	3162	A-4	B-4	C-4
	10000	A-5	B-5	C-5
	31622	A-6	B-6	C-6

III.2. TESTING EQUIPMENT

III.2.1. DLEPR Test

The electrochemical reactivation testing equipment was setup according to ASTM G108 standard [17]. The test cell consisted of a 1 litre flask with five necks for working electrode, two auxiliary electrodes, reference electrode and thermometer (Figure III-1).

The cylindrical working electrode was centrally located and two counter electrodes were placed next to specimen to improve the current distribution. The specimen was mounted according to Stern-Makrides arrangement. A stainless steel rod covered with a glass tube was screwed to specimen where between there was teflon gasket to prevent crevice attack from corrosive electrolyte (Figure III-2).

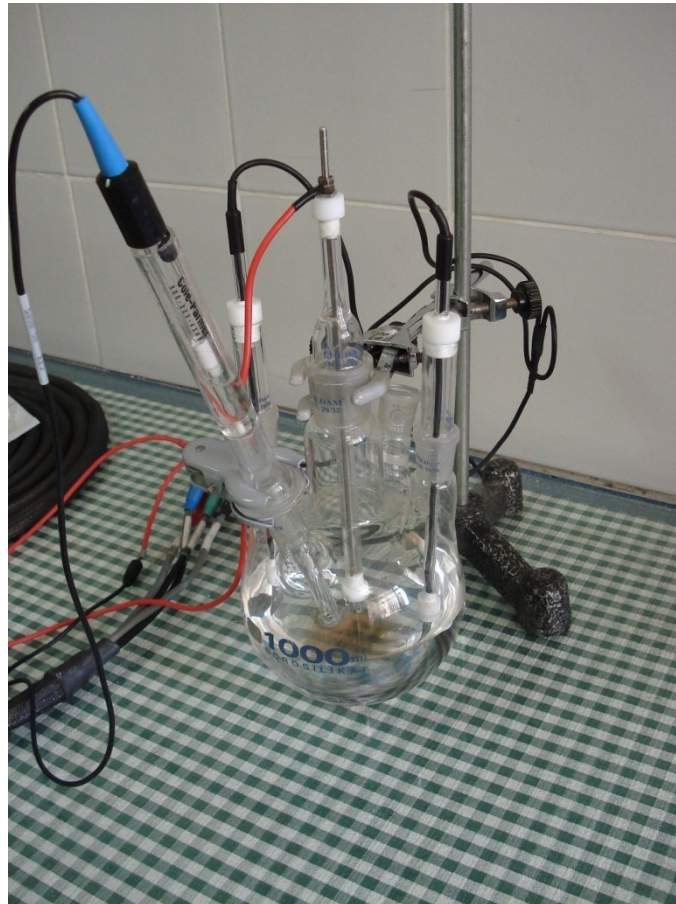


Figure III-1. Experiment setup [17].

The potential and current passing through the specimen was measured by Solartron 1480 multichannel potentiostat. Measurements were done with respect to a saturated calomel reference electrode (SCE). The reference electrode was placed in a salt bridge which contained the same solution used in experiment to provide the ionic conductivity. The data was converted to graphical view by CorrView software.

III.2.2. Oxalic Acid Etch Test

For oxalic acid tests according to ASTM A 262 Practice A [73], Struers Polipower potentiostat was used for power supply.



Figure III-2. Stern-Makrides specimen mount [17].

Etching solution was prepared using 100 gr of oxalic acid crystals ($C_2H_2O_4 \cdot 2H_2O$) dissolved in 900 ml deionized water. NaOH

electroetch test was done according to ASTM A923-03 [63] standard as described in section II-8.1.

III.2.3. X-ray Diffractometer

The presence of different phases in specimens was determined by X-ray diffraction analysis carried out by means of a Rigaku diffractometer with a Cu anticathode K. The specimens were scanned from 35 to 70 degrees (2θ) at a rate of 2°/min. The voltage was 40 kV with an applied current of 40 mA. Total power was 1.6kW.

III.3. EXPERIMENTAL PROCEDURE

III.3.1. Oxalic Acid Etch Test

The Oxalic acid test was applied according to procedure described in ASTM A262 Practice A [73]. The test consisted of the electrolytically etching a polished specimen at 1 A/cm² for 1.5 min in a 10% oxalic acid solution [74]. The etched specimens were then examined with SEM.

III.3.2. Sodium Hydroxide Etch Test

Sodium Hydroxide etch test is defined in ASTM A-923-03 [62] as a standard for duplex stainless steels. The solution for etching was prepared by adding 40 g of reagent grade sodium hydroxide (NaOH) to 100 g of distilled water. The polished specimens were electrolytically etched at 2 volts for 20 seconds.

III.3.3. DLEPR Test

The intergranular corrosion resistance can be reduced by the presence of chromium depleted areas. In order to relate the degree of sensitization (DOS) to intergranular corrosion, the DLEPR (Double Loop Electrochemical Potentiodynamic Reactivation) test is used [74]. It consists of polarizing the steel from the corroding potential to a potential in the passive area. Then the scanning direction is reversed to the corroding potential at the same rate. This reactivation leads to the preferential breakdown of the passive film on chromium-depleted areas due to precipitation. The DOS is then given by the ratio, I_r/I_a , with I_r being the maximum current recorded during reactivation and I_a the peak current of the first loop. The higher the ratio, the higher the material became sensitized.

This DLEPR test was first used on austenitic stainless steels by Majidi and Streicher [63]. The solution used was 0.5M H_2SO_4 + 0.01M KSCN. They observed that a sensitized material should give a current ratio, I_r/I_a , higher than 0.05. Some other studies have been carried out about the DLEPR test [67, 75, 76]. In 1994, Otero et al. [77] showed that there was a correlation between the σ -phase content of a duplex stainless steel and the reactivation loop. Nevertheless, a serious limitation of the DLEPR test appeared as the size effect of the precipitates which could lead to few chromium-depleted areas and, therefore, to a low current ratio while the material is very sensitized. In the present study, the test was performed according to the recommendations of Majidi and Streicher [63]. The standard solution was modified to suit duplex stainless steels and composed of: 2M H_2SO_4 + 0.01M KSCN + 0.5M NaCl at 30 ± 1 °C. All other experimental details were according to ASTM G 108 standard [17].

III.3.4. Weight Loss Test

The weight loss test was done according to ASTM A 923-03 Test Method C standard. This test method describes the procedure for conducting the ferric chloride corrosion test for detecting the presence of detrimental intermetallic phases in duplex stainless steels. In the present work the test solution was prepared by dissolving 100 g of reagent grade ferric chloride ($\text{FeCl}_3 \cdot 6\text{H}_2\text{O}$) in 900 ml of distilled water (6% FeCl_3 by weight). The pH of the solution was adjusted to approximately 1.3 by addition of HCl or NaOH. The thread openings of specimens were masked so that only the bottom and side faces of specimen were exposed to solution. The first step of the evaluation of tested specimens was visual and microscopic examination. The degree of sensitization was given by the loss of weight due to the dissolution of chromium depleted areas and is expressed as the rate of weight loss in mg per sq. dm per day (mdd).

III.3.5. Metallography

For metallographic examination an appropriate etchant should be used to detect the presence of phases in the material. Electrolytic etchants have been used widely in the study of stainless steels [78, 79], since they are simple in composition and use, generally quite safe and produce excellent results that are frequently superior to chemical etchants. The etching process can be accurately controlled by varying the voltage, current density and time. Thus, a high degree of reproducibility is obtainable. Usually the specimen surface can be etched, observed and re-etched without repolishing. This is not always possible for the case of using chemical reagents.

In the present work two metallographic etch tests were applied to detect the presence of phases in the duplex stainless steel. They are also used to check and validate the results of the DLEPR tests.

The first etch test is the oxalic acid etch test and it was performed according to ASTM A-262 A standard [73] as described in section III-3.1.

The second metallographic etch test is performed using NaOH aqueous solution as described in ASTM A-923-03 [62] as a standard for duplex stainless steels. It may be utilized in connection with other evaluation tests to provide a rapid method for identifying those specimens that are free of detrimental intermetallic phases. This test colors the different phases in the duplex stainless steel; any intermetallic phase is revealed by yellow austenite white, ferrite light brown, sigma dark brown and carbides black.

For microscopic examination specimens were prepared using conventional metallographic techniques. Grinding was performed using water cooled silicon carbide papers of 120-, 240-, 320-, 400-, 600-, 800-, 1000-, 1200-, 1500- and 2000- grid size. After being ground to a 2000-grit finish, the samples were polished to 1 μ m and then electrolytically etched. The microstructures and microanalysis of phases or precipitates in the aged specimen were investigated by using;

- Light optical microscopy (Leica DMI 5000 M metal microscopy),
- Scanning electron microscopy (Jeol 6400),
- EDS attached to SEM (Noran),
- X-Ray diffraction analysis by means of Rigaku diffractometer with a Cu-anticathode (K_{α} radiation).

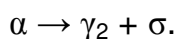
CHAPTER IV

RESULTS AND DISCUSSION

IV.1. METALLOGRAPHY

The optical micrographs obtained by etching with NaOH reagent are given in Figures IV-1-4. Figure IV-1 represents the microstructure of solution annealed parent alloy in which white phase is austenite (γ) and the dark phase is ferrite (α). The volume fraction of α and γ was approximately 54:46. The microstructure does not reveal any visible precipitation.

To study the influence of the microstructure on degree of susceptibility to intercrystalline corrosion, specimens were aged at 650, 725 and 800°C for times 100, 316, 1000, 3162, 10000 and 31622 min. The ageing heat treatments induce changes in the microstructures as depicted in Figures IV-2 and IV-3. The structures corresponding to the sensitization are characterized by an eutectoid decomposition of the ferrite phase which is transformed partially or totally into secondary austenite (γ_2), chromium carbides and intermetallic phases (σ , χ , etc.) [81]. The first carbide precipitates were identified at the α/γ grain boundaries. After longer period of times the following eutectoid transformation took place [82];



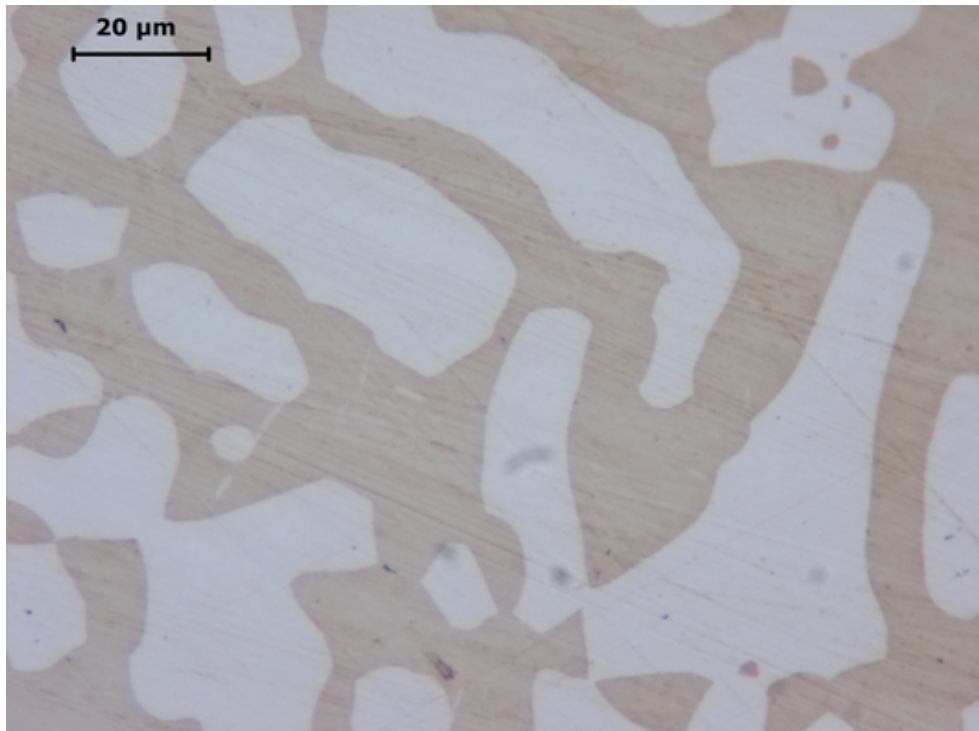


Figure VI-1. Solution annealed at 1050 °C for 1 hr then WQ (brown phase is ferrite, white phase austenite).

IV.1.1. Microstructural Evolution at 650 °C Ageing

Microstructural changes obtained by etching with NaOH reagent are shown in Figures IV-2(a-f). For ageing from 100 to 316 min, the first tiny precipitates appear at α/γ and α/α boundaries. Incoherent twin boundaries and dislocations inside the ferrite matrix may also be the nucleation sites for precipitation [83]. The precipitation of σ -phase was first identified after ageing for 1000 min and its size and amount increased with the ageing time.

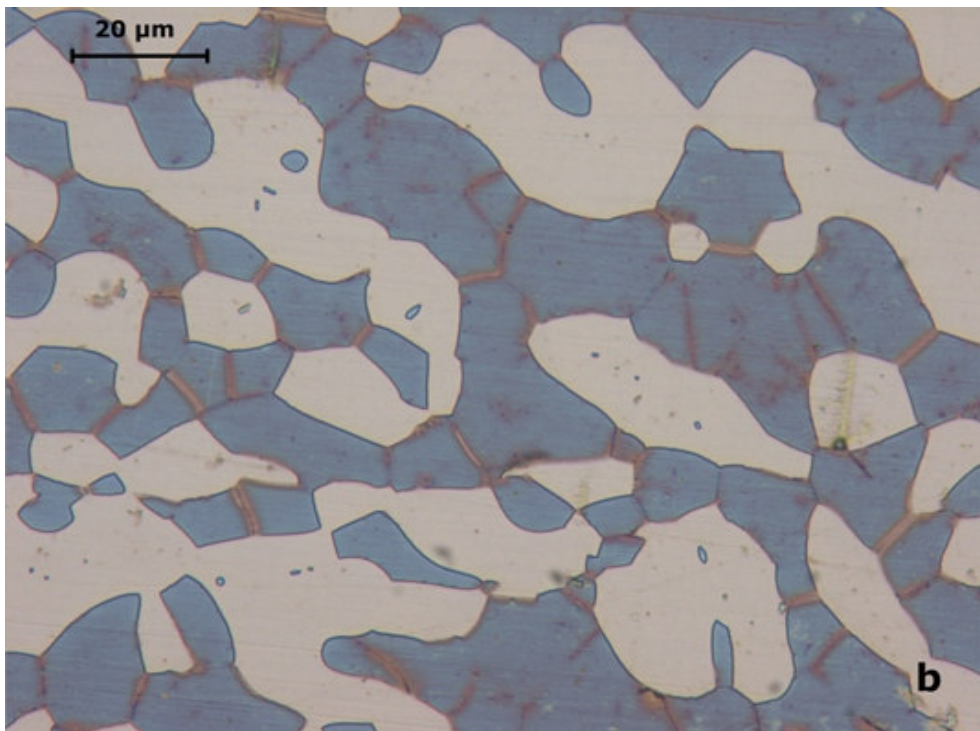
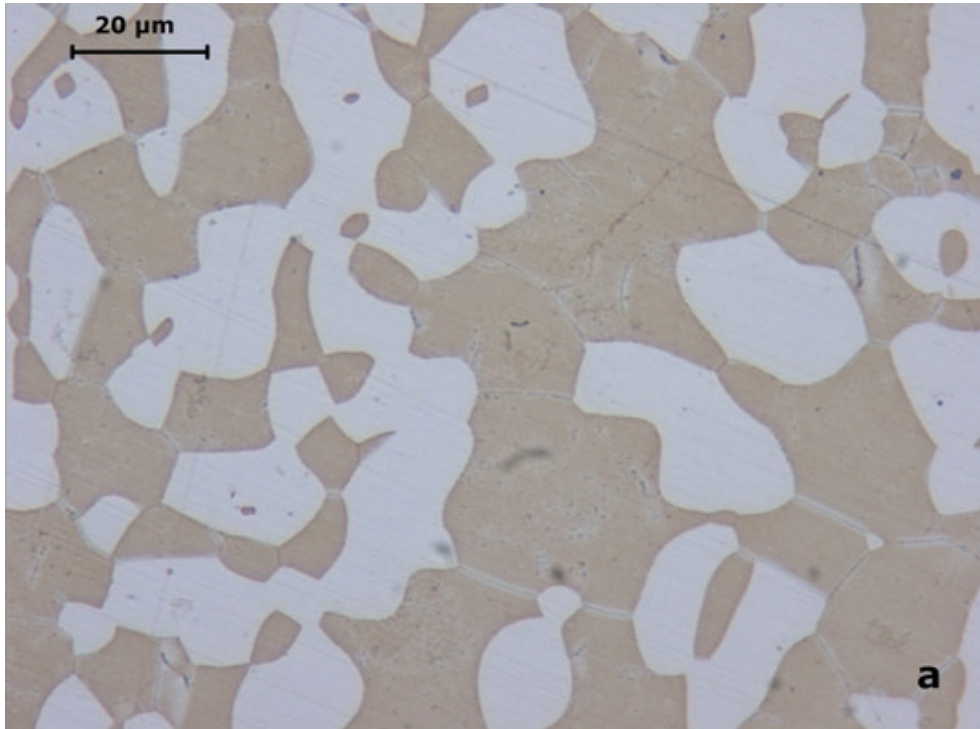


Figure IV-2. Optical micrographs obtained after ageing at 650 °C by etching with NaOH reagent (a) 100 min, (b) 316 min (austenite in white, ferrite in dark).

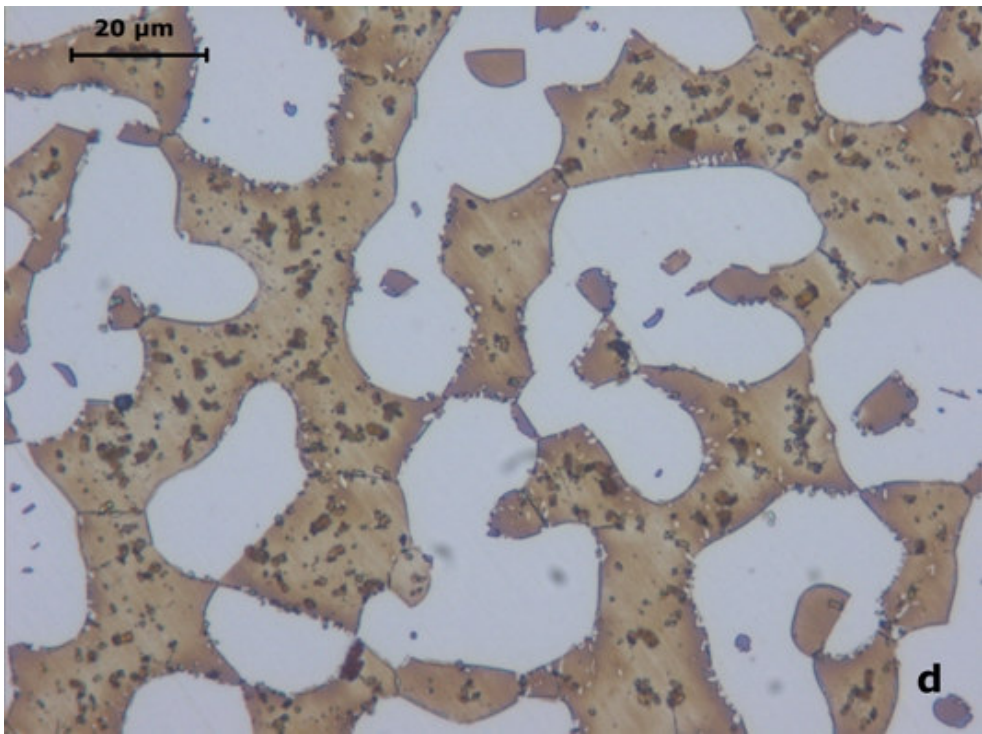
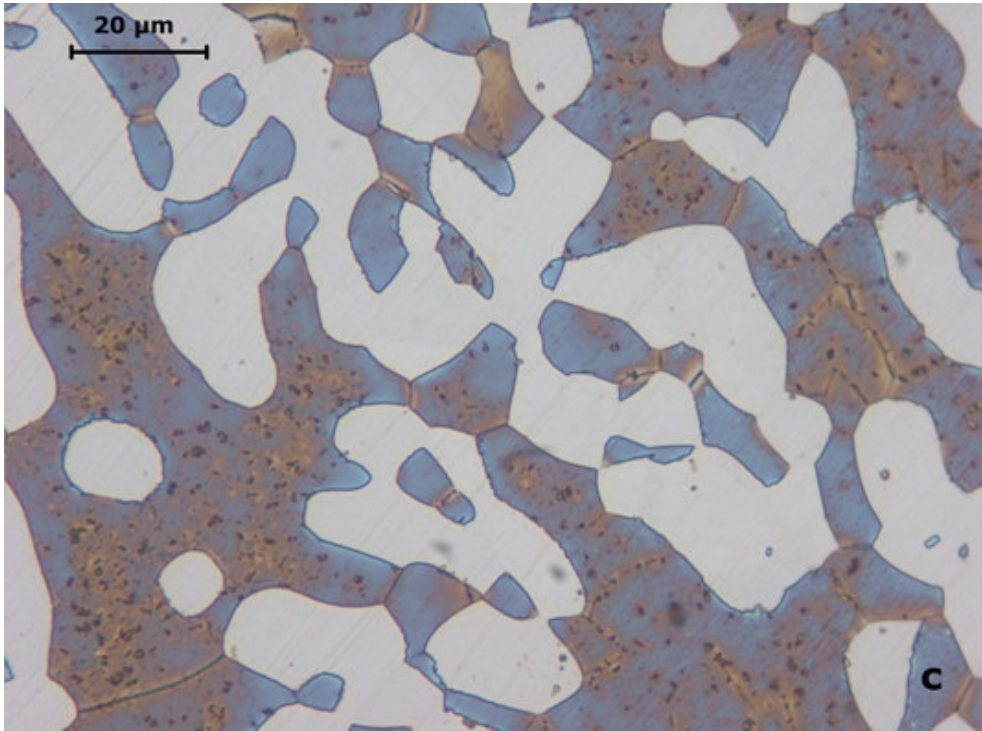


Figure IV-2.(cont.) (c) 1000 min, (d) 3162 min (austenite in white, ferrite in brown-blue, sigma precipitates in dark brown).

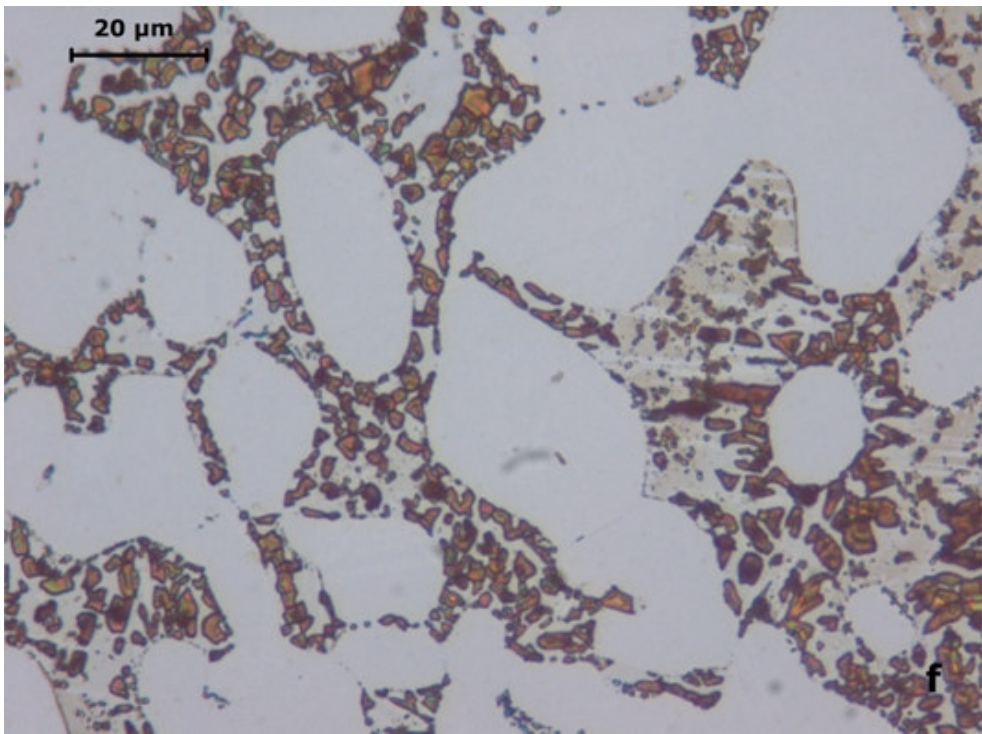
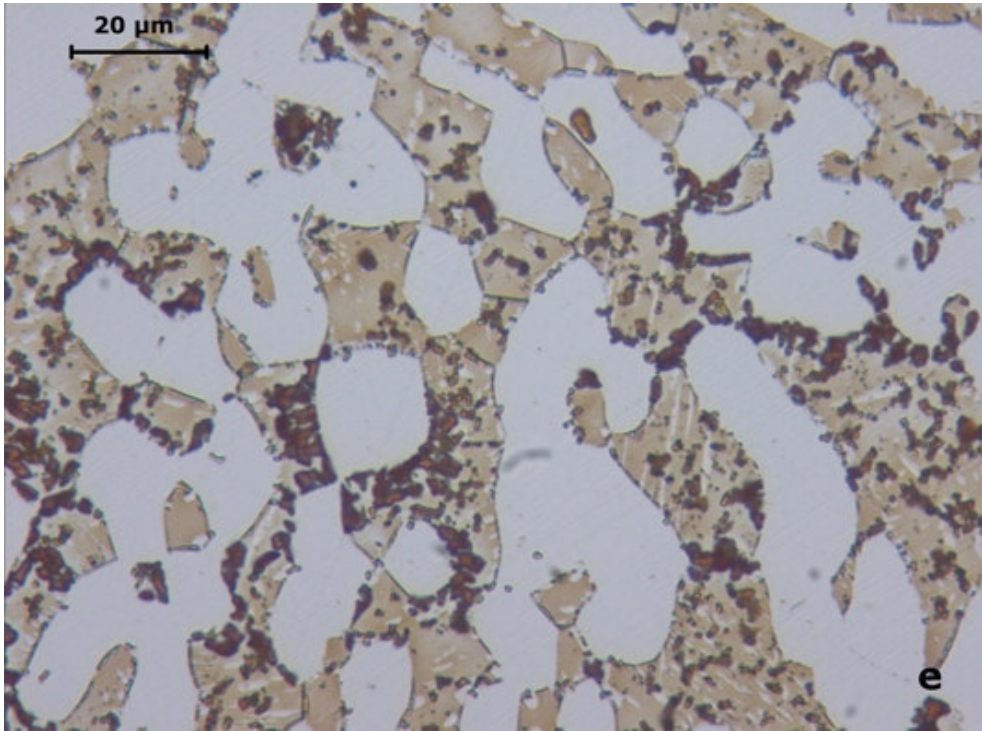


Figure IV-2.(cont.) (e) 10000 min, (f) 31622 min. (austenite in white, ferrite in brown, sigma precipitates in dark brown).

IV.1.2. Microstructural Evolution at 725°C Ageing

When ageing at 725°C for 100 and 316 min, carbides, nitrides and chi phases nucleated predominantly at α/γ boundaries, whereas precipitation at α/α and inside the ferrite matrix may also occur (Figure IV-3(a-b)). The formation of sigma phase was first observed after 316 min mostly at the phase boundaries.

After 1000 min a large number of sigma precipitates have formed at α/γ and α/α boundaries and inside the ferrite phase as shown in Figure IV-3(c). Longer ageing treatment resulted in the increase and coarsening of the σ -phase in irregular shape (Figure IV-3(d-f)).

From the EDS analysis of the phases, it is seen that the σ -phase is rich in chromium and molybdenum. During the growth of sigma phase, these elements diffuse from the surrounding ferrite matrix to the sigma phase and causes depletion in these elements. The depletion in chromium and molybdenum leads to the transformation of the region to secondary austenite (γ_2). At longer ageing times all ferrite has transformed into σ and γ_2 phase. Consequently the sigma precipitates were enveloped with the newly formed secondary austenite (γ_2).

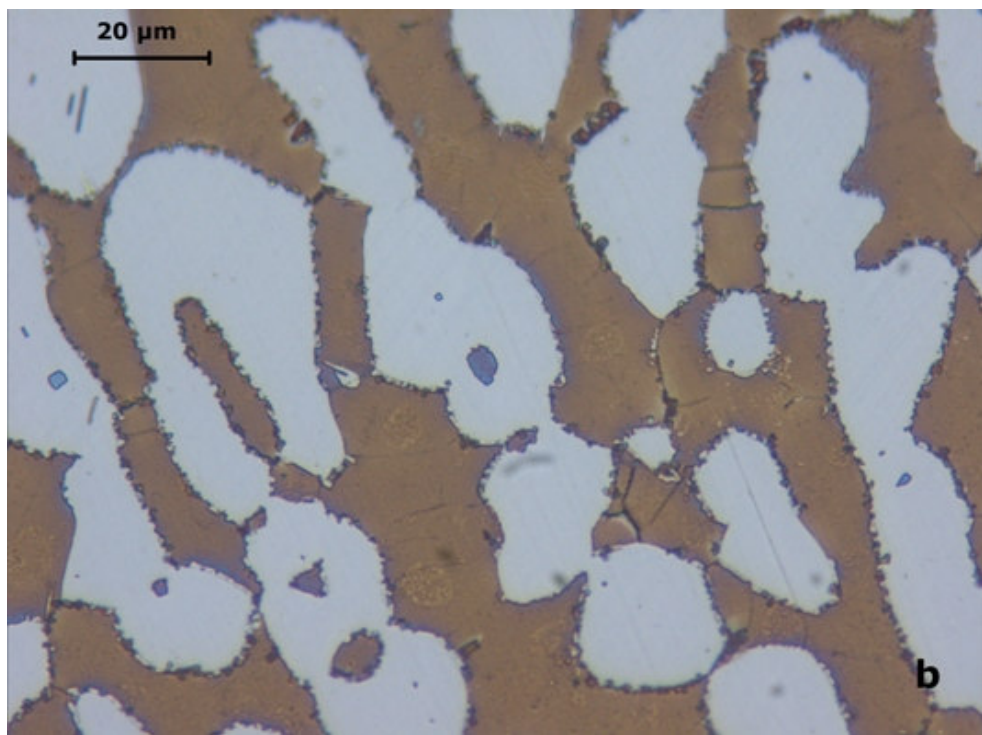
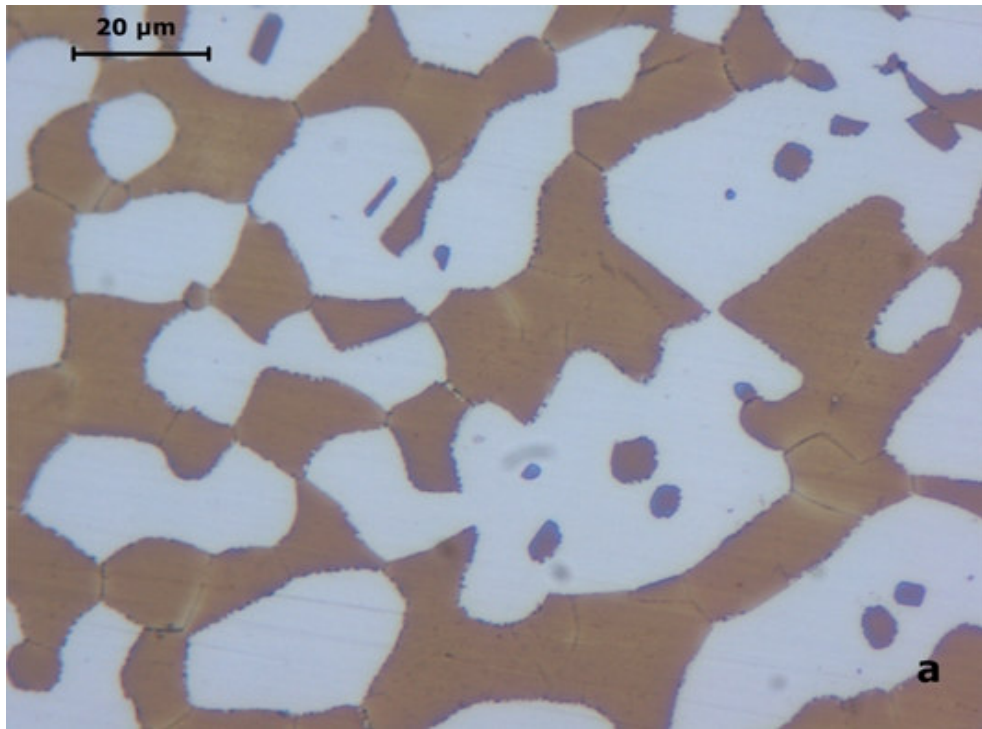


Figure IV-3. Optical micrographs obtained after ageing at 725°C, etched with NaOH reagent (a) 100 min, (b) 316 min (sigma precipitates along ferrite/austenite boundaries).

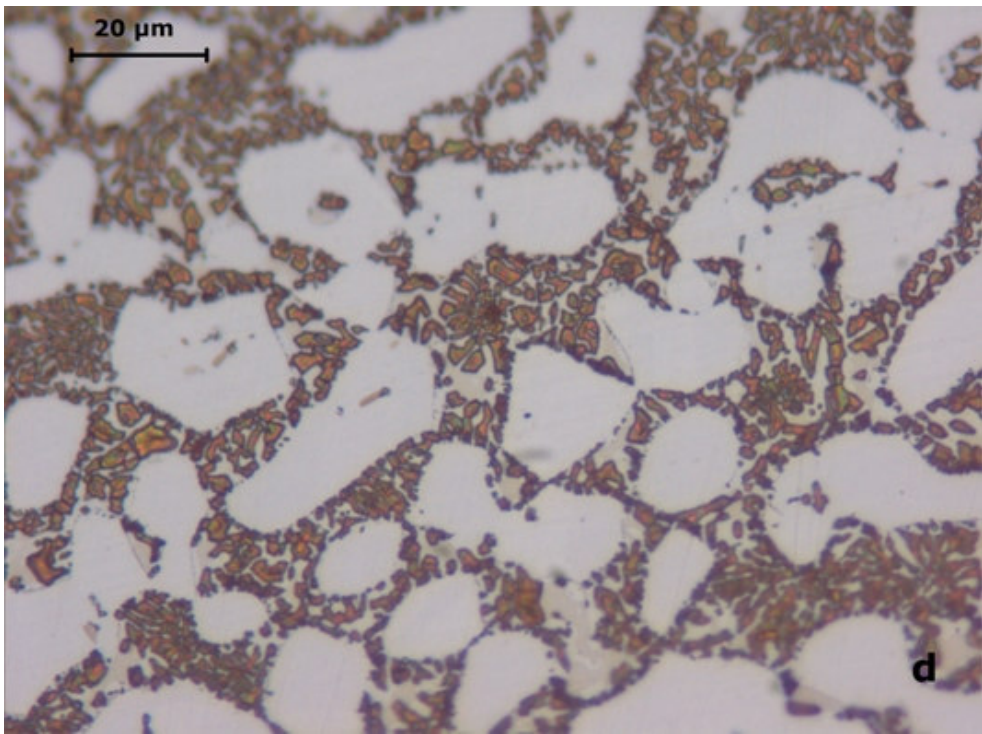
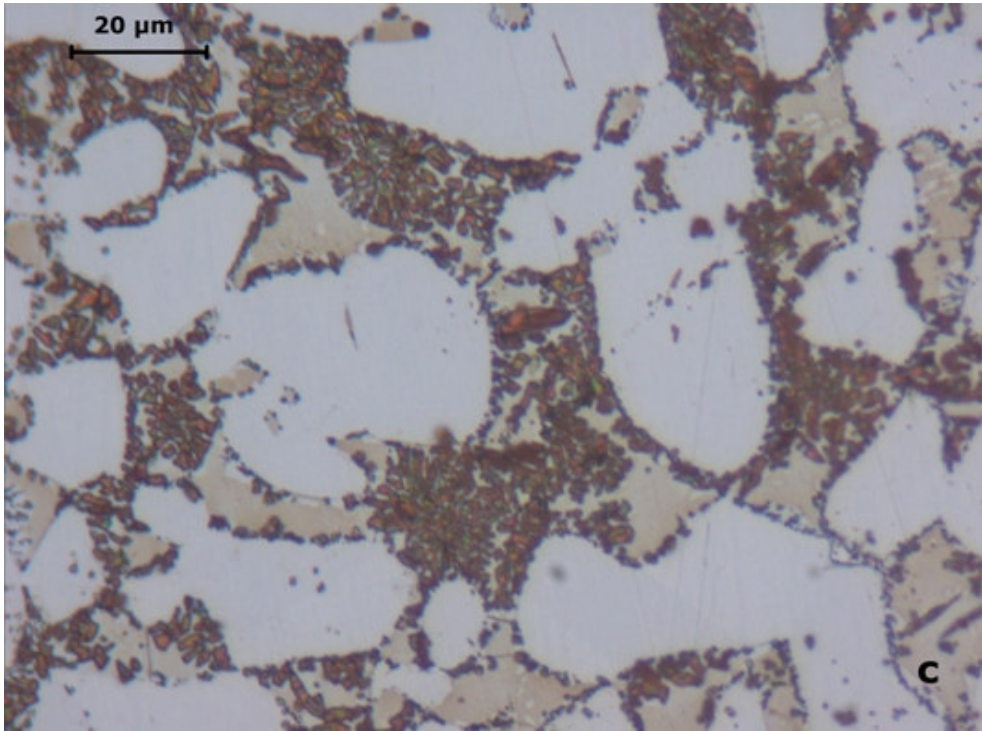


Figure IV-3.(cont.) (c) 1000 min, (d) 3162 min (austenite in white, ferrite in brown, sigma precipitates in dark brown).

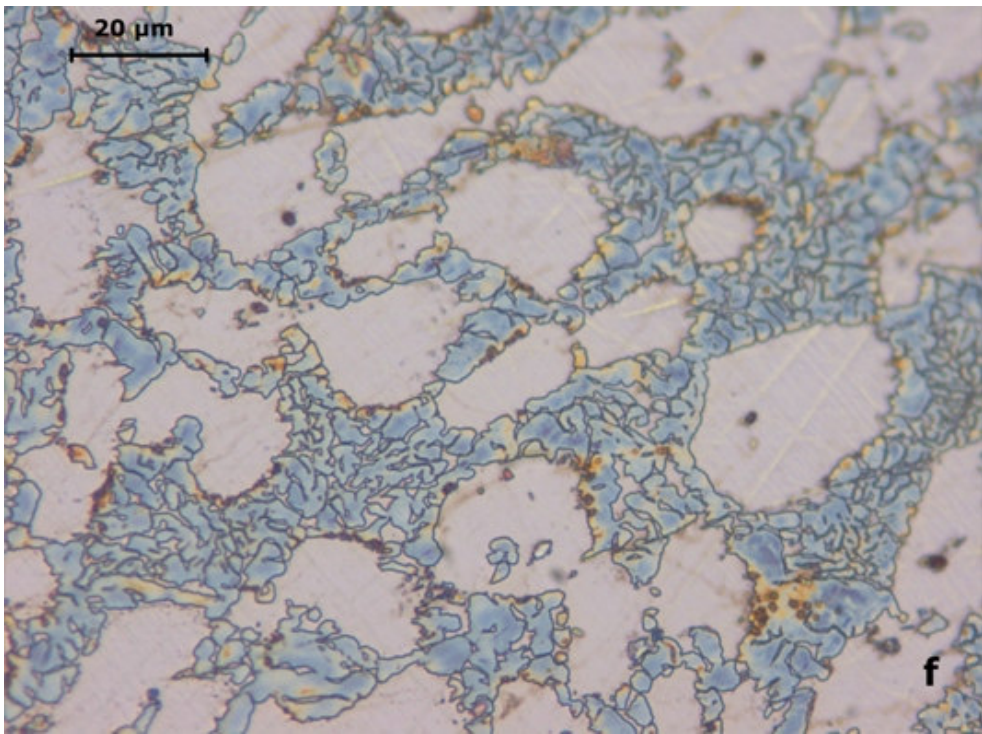
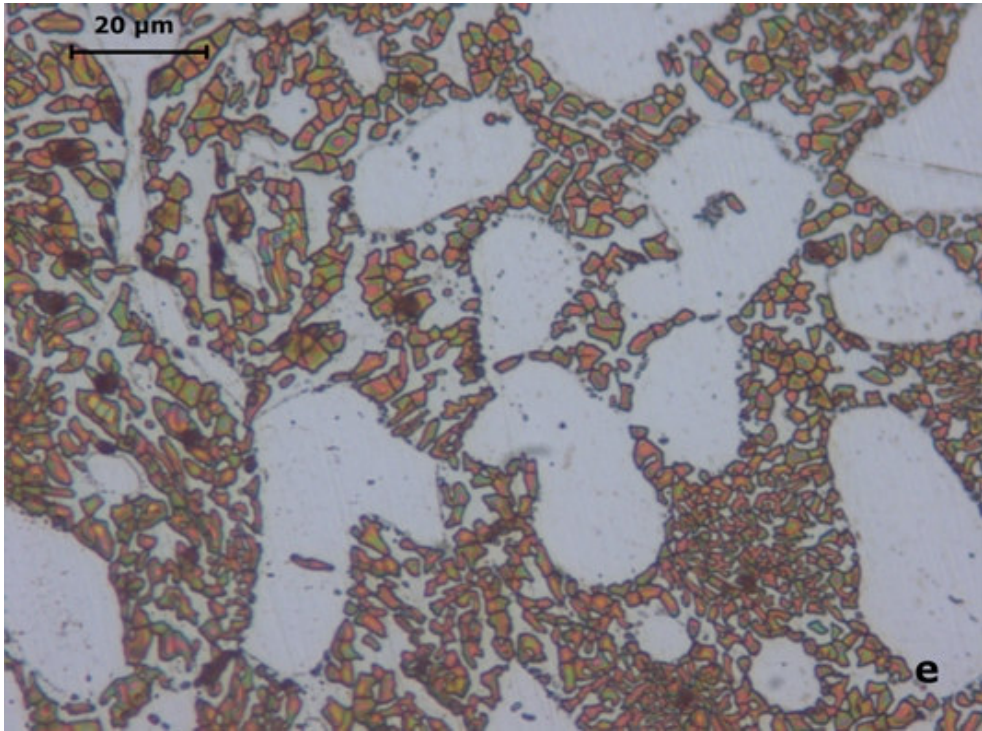


Figure IV-3. (cont.) (e) 10000min (sigma in dark brown) (f) 31622min (austenite in white, sigma precipitates in blue).

IV.1.3. Microstructural Evolution at 800 °C Ageing

At this ageing temperature, in addition to carbides and chi phase, small σ -phase precipitates formed in shorter time (100 min) and grew faster than that formed at 650 °C and 725 °C. The sigma phase became the dominant precipitate for the ageing time of 316 min. It is in reddish brown and became large in size after 1000 min. Between 3162 and 31622 min, the sigma and secondary austenite have grown into massive forms with irregular shape as shown in Figure IV-4(d-f).

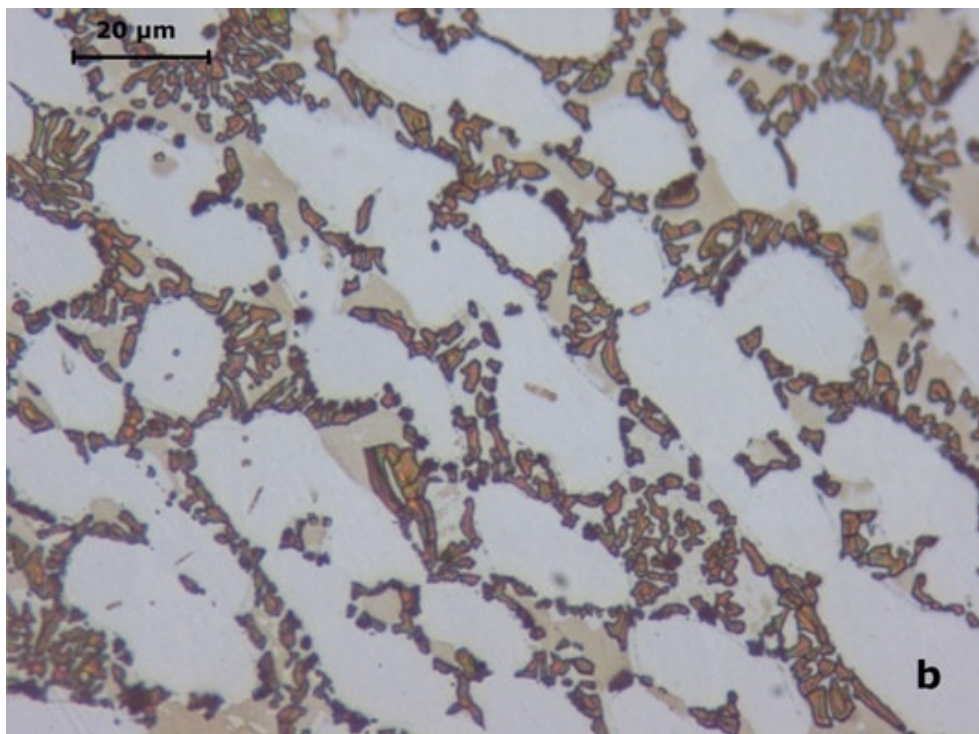
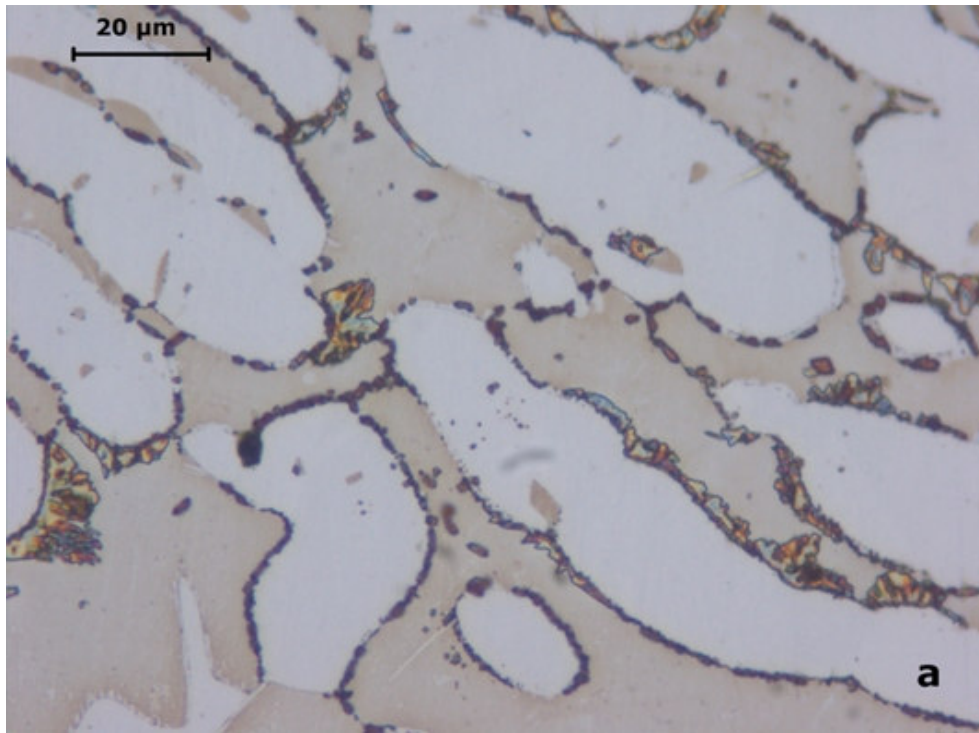


Figure IV-4. Optical micrographs obtained after ageing at 800°C, etched with NaOH reagent (a) 100 min, (b) 316 min (austenite in white, ferrite in light brown, sigma in dark brown).

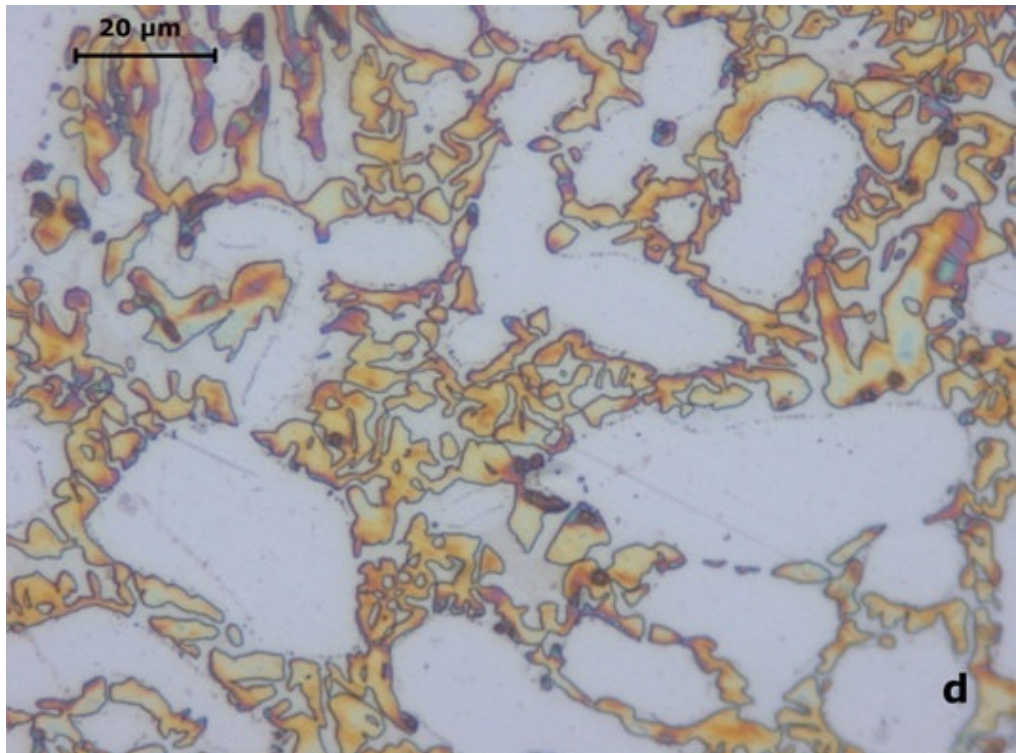
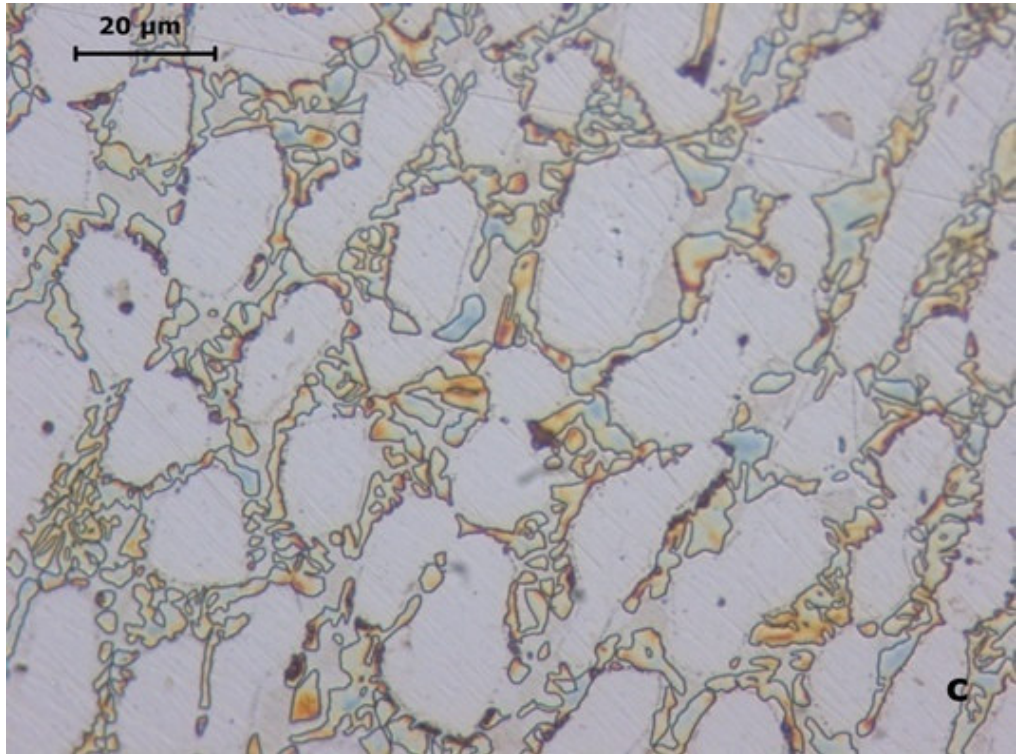


Figure IV-4.(cont.) (c) 1000min (d) 3162min (austenite in white, sigma in dark brown).

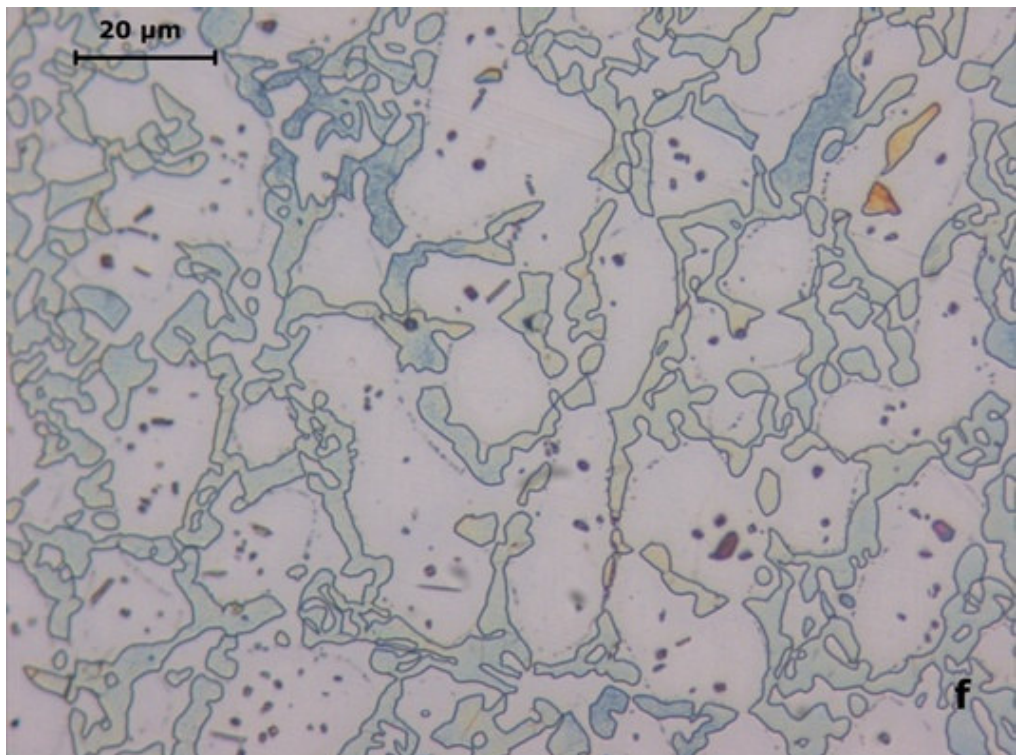
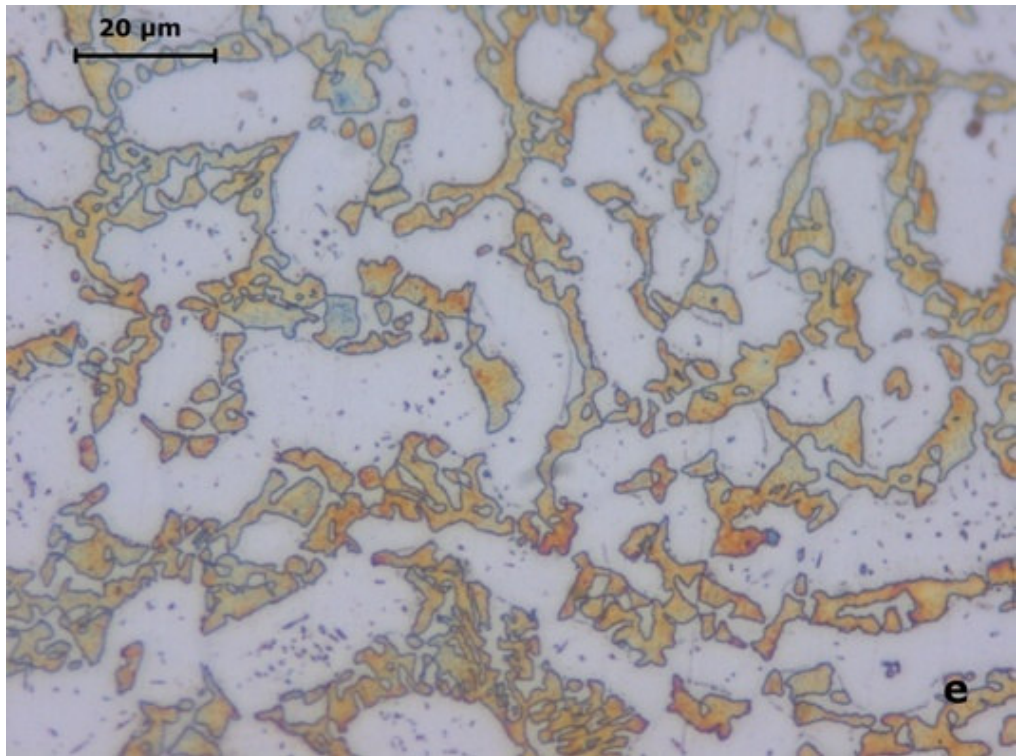


Figure IV-4.(cont.) (e) 10000min (sigma in dark brown)
(f) 31622min (austenite in white, sigma in blue).

IV.2. PHASE VOLUME FRACTION BY LIGHT OPTICAL MICROSCOPY

Microanalysis reveals that the solution annealed material consists of ferrite and austenite phases. The main microstructural change during ageing is the formation of σ -phase and secondary austenite (γ_2) from the ferrite phase due to the eutectoid reaction; $\alpha \rightarrow \sigma + \gamma_2$.

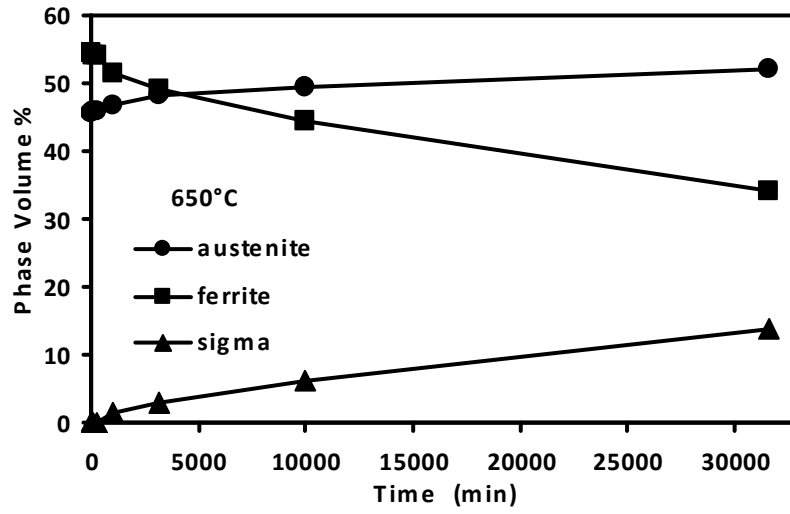
The amounts of phases were estimated by measuring the fractions of colored area on polished and etched specimens by LOM. The determined amount of precipitates is subjective since it is almost impossible to evaluate small precipitates, e.g. nitrides, carbides and chi phase quantitatively. Since the carbon content of the alloy is small (0.026%) the volume fraction of the carbide precipitate will be very low to detect by the employed technique. The measured volume fractions of ferrite, austenite and sigma phases at different ageing times and temperatures are given in Table IV-1 and Figure IV-5. Since the ferrite transforms into σ and γ_2 , the ferrite phase decreases as the volume percentages of sigma and secondary austenite increase with ageing time until the whole ferrite is totally consumed. At low temperature (650°C) the transformation of ferrite is slow and takes longer ageing time, whereas at high temperature (800°C) it disappears in shorter time. The total austenite considered as the sum of the primary and secondary austenite ($\gamma + \gamma_2$) increases with time at all temperatures.

Figure IV-5 compares the change of the volume fractions of ferrite, austenite and sigma phases as a function of ageing time at each ageing temperature. Figures IV-5(b-c) indicate that ferrite continuously decreases throughout each of the isothermal holds, reaching zero or near-zero values at 725°C and 800°C. However at

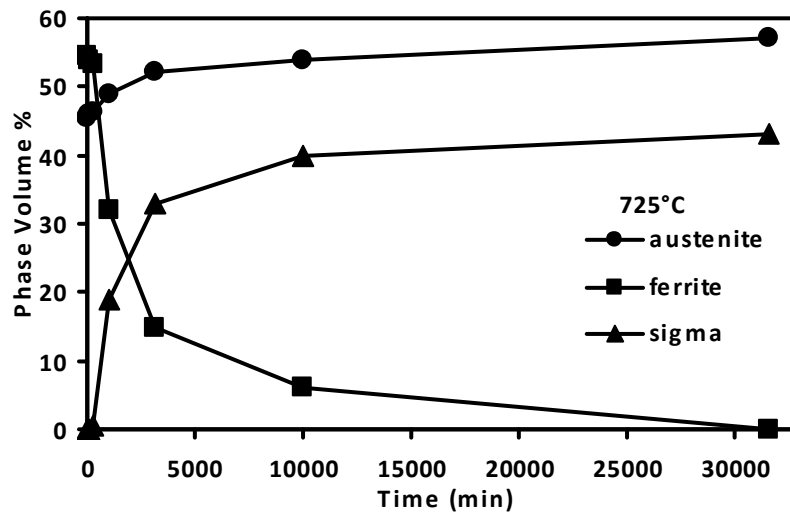
650°C (Figure IV-5(a)) the transformation appears too slow for the ferrite to reach its equilibrium value, which was nearly 20% at the end of the 31622 min run.

Table IV-1. The phase volume percentages obtained from digital image analysis.

Heat Treatment	Ageing Time (min.)	Ferrite Phase %	Austenite Phase %	Sigma Phase %
Solution annealed at 1050 °C, 1 h		54.55	45.45	0
Solution annealed at 1050 °C + Aged at 650 °C	100	54	46	0
	316	54	46	0
	1000	51.6	46.8	1.6
	3162	49.1	48.1	2.8
	10000	44.9	49.4	6.3
	31622	34.1	52.2	13.7
Solution annealed at 1050 °C + Aged at 725 °C	100	54	46	0
	316	53.2	46.2	0.6
	1000	32	49	19
	3162	15	52	33
	10000	6	54	40
	31622	0	57	43
Solution annealed at 1050 °C + Aged at 800 °C	100	49	46.4	4.6
	316	26.7	51.3	22
	1000	1.8	54.5	43.7
	3162	0.7	55	44.3
	10000	0	55	45
	31622	0	55	45

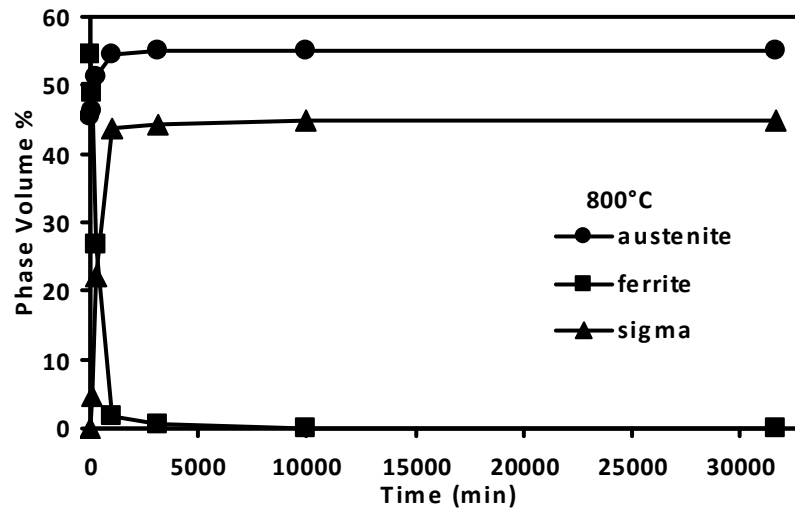


(a)



(b)

Figure IV-5. Changes in volume % of austenite, ferrite and sigma phases with ageing time at (a) 650°C, (b) 725°C and (c) 800°C.



(c)

Figure IV-5. (cont.) Changes in volume % of austenite, ferrite and sigma phases with ageing time at (a) 650°C, (b) 725°C and (c) 800°C.

At 725°C the austenite phase continuously increases to values between 52 and 60% during the isothermal holds (Figure IV-5(b)). The trends suggest that the austenite phase is reaching near equilibrium values at all temperatures. At 800°C the change of sigma phase is shown in Figure IV-5(c). At 650, 725 and 800°C the final volume fraction of sigma ranges from 13.7 to 45%, as summarized in Table IV-1.

During the early stages of the transformation, sigma forms preferentially at the α/γ and α/α grain boundaries and inside the α -grain and grows into the ferrite phase via a transformation mechanism involving diffusion. Because both nucleation and diffusional growth of σ -phase are thermally activated processes, temperature will have a

significant effect on the kinetics of the transformation. In order to look at this more closely, Figure IV-6 compares the measured volume fractions of sigma that forms during the early stages of the transformation at each temperature. Times where sigma was first observed are further summarized in Table IV-1, indicating that the minimum time needed to form sigma was less than 100 min at 800°C and longer than 316 and 1000 min at 725 and 650°C respectively.

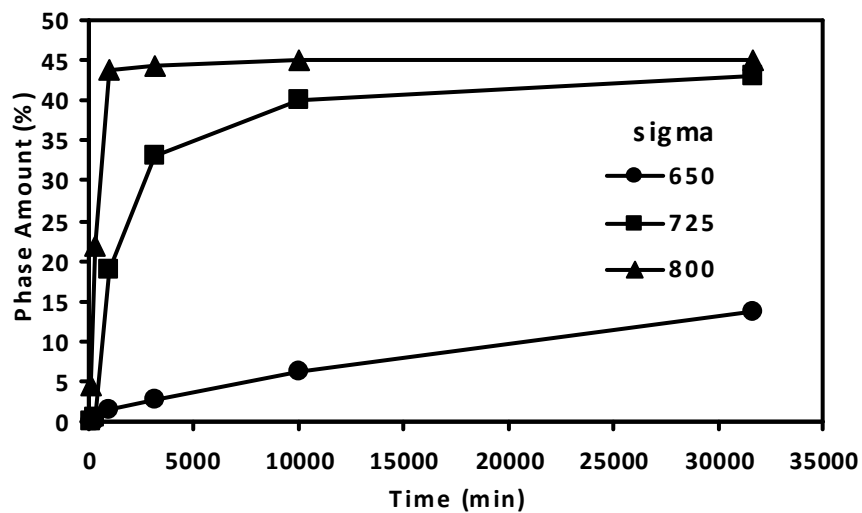


Figure IV-6. The change of sigma phase with ageing time at 650, 725 and 800 °C.

IV.3. ISOTHERMAL SIGMA PHASE FORMATION

Figure IV-7 (a, b) shows a portion of the microstructure in the early nucleation and growth stages at 650 and 725°C. It is clear that sigma preferentially forms at α/γ , α/α boundaries and inside the α

grains. At 725 and 800 °C, the precipitates take on more of blocky or elongated appearance.

When sigma nucleates, it grows from ferrite (α) with the simultaneous formation of secondary austenite (γ_2) by the transformation $\alpha \rightarrow \sigma + \gamma_2$ [84]. Although the transformation mechanism does not appear to be characterized perfectly well in the literature, it is likely that one of the major modes for decomposition of ferrite occurs by a discontinuous precipitation mechanism.

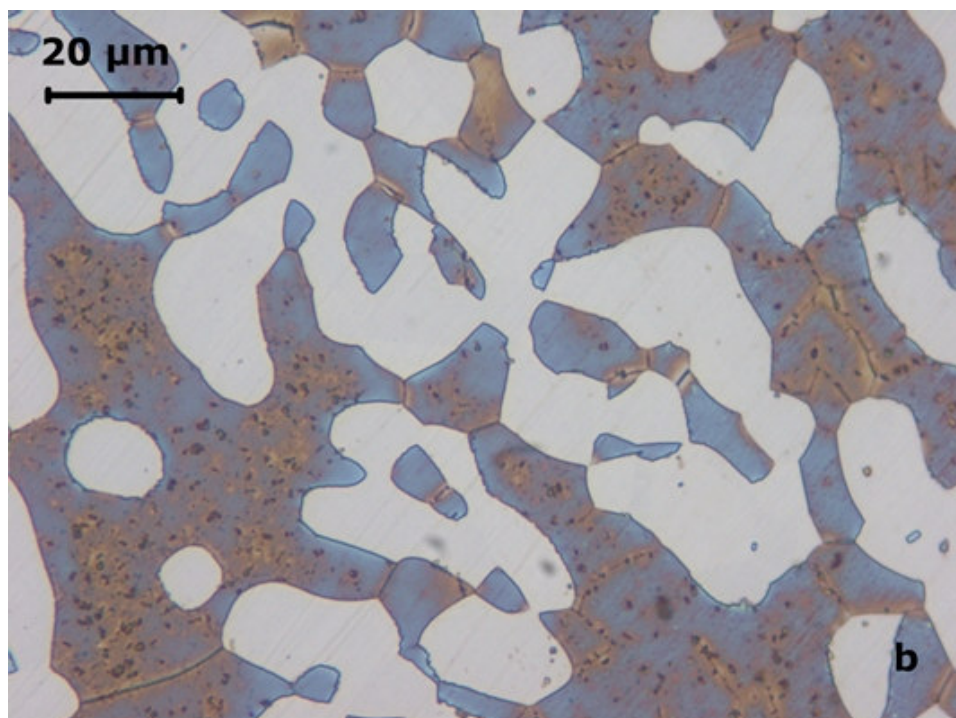
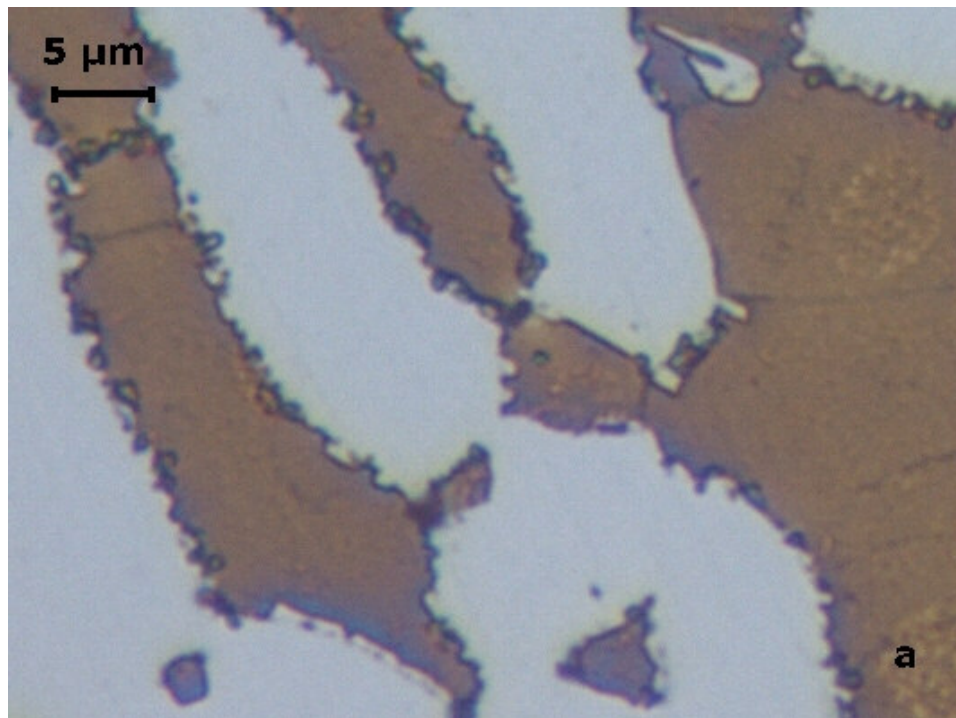


Figure IV-7. (a) Initial stage of sigma phase formation after 316 min at 725°C. The sigma phase precipitates form preferentially at α/γ and α/α boundaries. (b) Sigma phase precipitates inside the ferrite grains after 1000 min at 650°C.

This mechanism is also referred to as cellular precipitation which is similar to a eutectoid transformation in steels [84]. In the case of 2205 DSS, the secondary austenite and sigma phases would grow through the cooperative partitioning of elements between them [84, 85].

Microstructural evidence suggests that the secondary austenite first forms at the α/γ boundaries causing chromium and molybdenum to be rejected into the ferrite ahead of the secondary phase. When the concentration of the ferrite is enriched sufficiently in these elements, sigma nucleates and grows sometimes alongside the secondary austenite as indicated in Figure IV-8, and other times as isolated sigma particles that became surrounded by the secondary austenite as shown in Figure IV-9.

The time required for chromium and molybdenum to enrich accounts for the delay in nucleation of sigma phase, which is most evident at 650, 725 and 800 °C as shown in Figure IV-5 and Table IV-1. Figure IV-8 shows a micrograph of the partially transformed microstructure from the 800 °C isothermal hold and indicate the major microstructural constituents (α , γ , σ and γ_2). Secondary austenite and sigma grow cooperatively into the original ferrite. Possible evidence for the discontinuous precipitation of sigma appears most clearly at the original ferrite/austenite grain boundaries where multiple cells of secondary austenite (γ_2) are growing with sigma.

Isolated sigma phase precipitation also appears in the ferrite where they most likely nucleated heterogeneously from pre-existing inclusions or defects in the ferrite phase and are accomplished by secondary austenite. Optical metallography of the alloy aged at 650 °C revealed fine precipitates within the ferrite phase as shown in Figure IV-7(b). However these precipitates are too fine to allow definitive identification, but they suspected to be either carbides, nitrides or a

secondary phase.

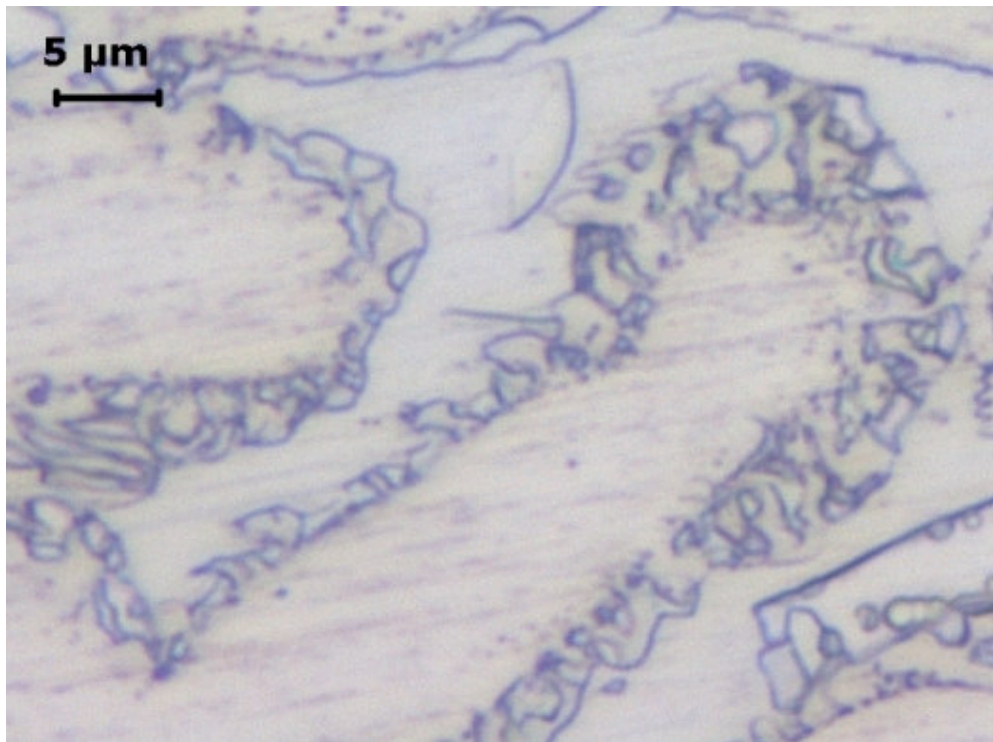


Figure IV-8. The micrograph taken after ageing for 316 min at 800 °C. The original austenite (γ), ferrite (α), secondary austenite (γ_2), nitrides/carbides at the original austenite/ferrite interface (N/C) and sigma phase (σ) are indicated. The discontinuous precipitation mode of the $\alpha \rightarrow \sigma + \gamma_2$ transformation can be seen along the original austenite grain.

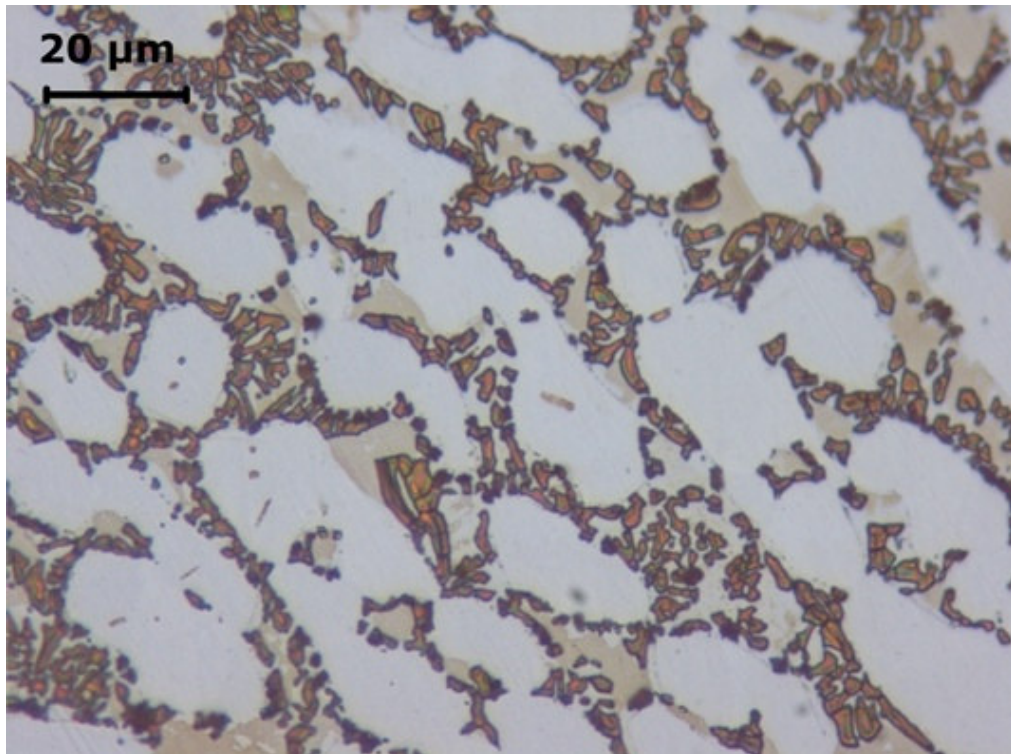


Figure IV-9. Optical micrograph showing ferrite (α) (light brown), austenite (γ) (white), sigma phase (σ) (dark brown) appear after 316 min of ageing at 800 °C.

IV.4. WEIGHT LOSS TEST

Evaluation of corrosion rate is provided comparatively by visual, microscopic examination and weight loss of the steel. The degree of sensitization is given by the loss of weight due to the dissolution of chromium depleted areas and is expressed as the rate of weight loss in mdd.

The results of standard weight loss immersion test are given in Table IV-2 and plotted in Figure IV-10. Corrosion rate of specimen aged at 650 °C is low up to 1000 min. Then it increases rapidly up to 31622 min. For specimens aged at 725 °C, the corrosion rate increases rapidly up to 1000 min, then slows down and even a slight decrease is

observed for 3162 and 10000 min of ageing and then increases slightly by the end of 31622 min. When aged at 800 °C the corrosion rate is quite high for 100 min and increases up to 1000 min. Beyond that point, its behavior resembles the curve obtained at 725 °C. The reason is the chromium replenishment of the depleted zone because of the availability of time for chromium diffusion from the interior of the grains. The other reason may be the coarsening of σ -phase while the secondary austenite area decreases.

Table IV-2. Weight loss immersion acid test results (mdd) according to ASTM A 923-03.

Ageing Time (min)	Ageing Temperature (°C)		
	650 °C	725 °C	800 °C
100	0.00000	0.49451	2.06075
316	0.01822	2.37328	4.39316
1000	0.50147	5.38945	4.99917
3162	2.42141	5.16104	4.64326
10000	5.88644	5.28002	4.80819
31622	7.09174	6.04718	5.09572

Moreover, the lower chromium and molybdenum content is not the only factor for being prone to corrosion. The neighborhood of more noble phases (sigma phase) will enhance the anodic dissolution of secondary austenite extensively. The network-like ferritic phase turns into a continuous network of low alloyed secondary austenite. This allows deep corrosion attacking through the whole wall thickness of the

component [86]. The surfaces of the corroded specimens were examined using LOM. The appearance of the localized attack after immersion testing is shown in Figures IV-11 and IV-12. The picture and pitting attack in black points in the figure clearly show that local corrosion is initiated in the secondary austenite phase adjacent to the sigma phase. In other words, the initiation sites for the pits are located inside the secondary austenite phase. This type of attack represents pitting corrosion as visible in the figure. Large numbers of small pits were observed.

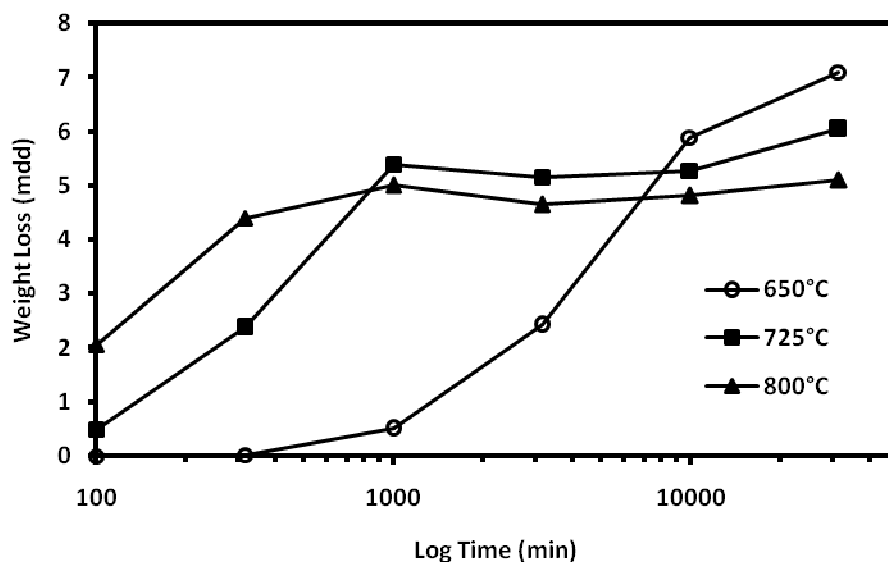
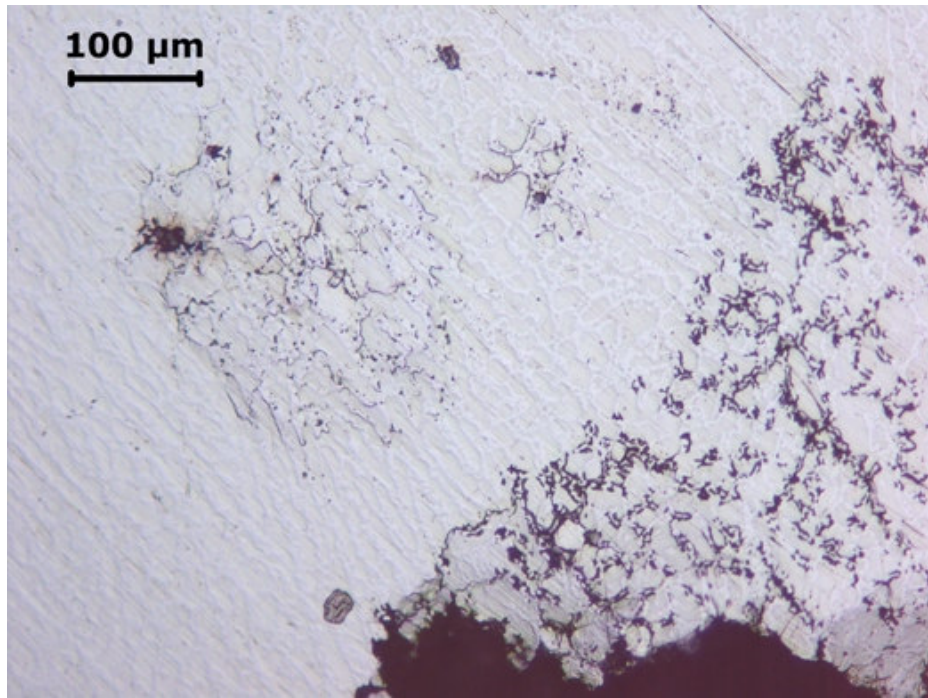


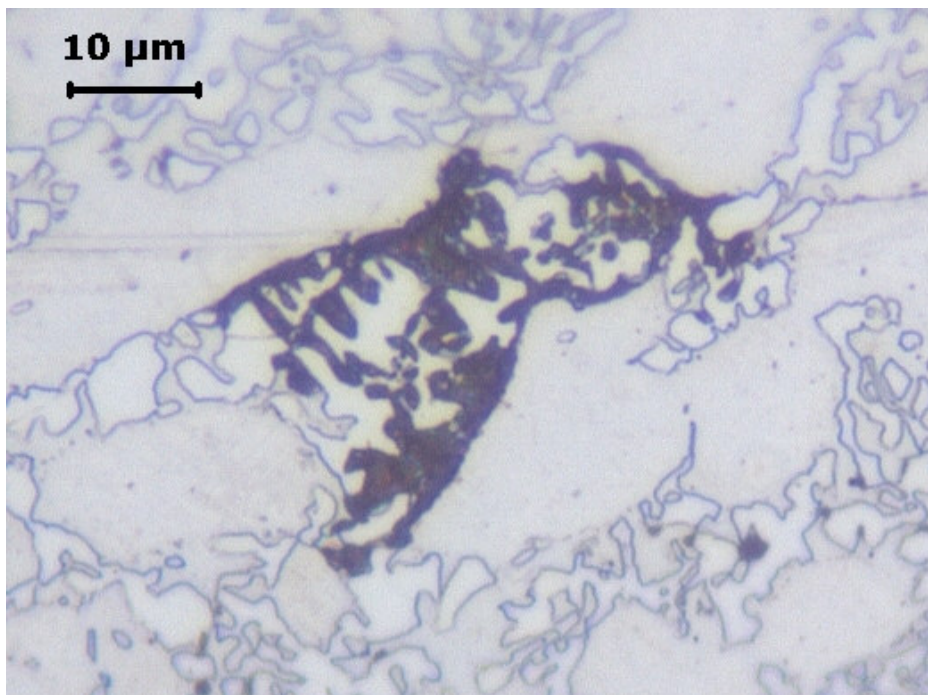
Figure IV-10. The change in weight loss with ageing time.

The austenite and sigma phase are by far more resistant to ferric chloride solution than the ferrite or secondary austenite. Once a pit is formed they rapidly propagate within the initial ferrite region. After a

long time of exposure, the corroded area extended and covered a large area including many sigma and austenite phases. As a result big cavities with 1-3 mm in diameter and 1-3 mm in depth were developed. It was also seen that there existed a large affected zone around cavities. This type of corrosion is known as localized corrosion.



(a)



(b)

Figure IV-11. Corroded area of the aged specimen at 800 °C / 31622 min after the standard immersion test for 24 hours . (a) large initiated areas of localized corrosion (black), (b) the corrosion propagates within the secondary austenite (slightly etched with oxalic acid) and big cavities are formed as seen in (a).

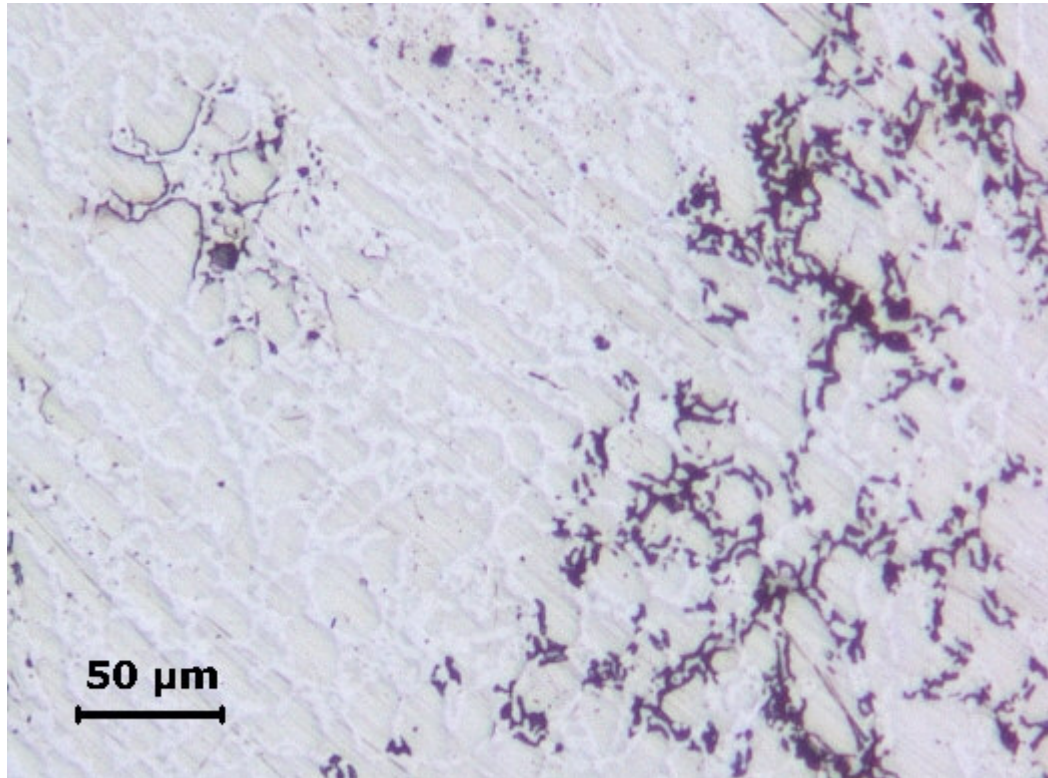


Figure IV-12. Dissolution of low chromium area (secondary austenite (γ_2)), aged at 800°C for 31622 min, results in considerable weight loss. (5.09 mdd) (Table IV-2.).

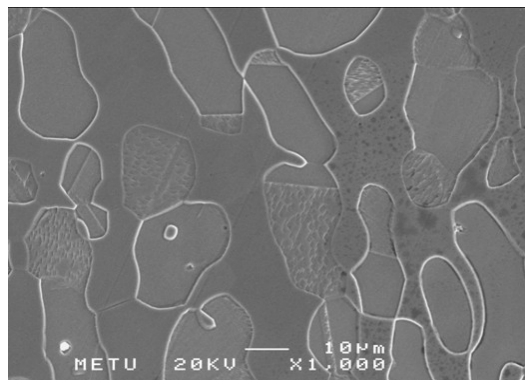
IV.5. THE EFFECT OF MICROSTRUCTURAL CHANGES ON CORROSION

Figure IV-13 shows SEM micrographs only for specimens electrolytically etched with oxalic acid after isothermal ageing at 650°C from 100 min to 31622 min.

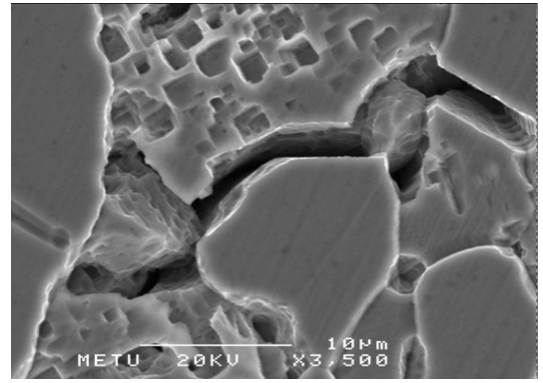
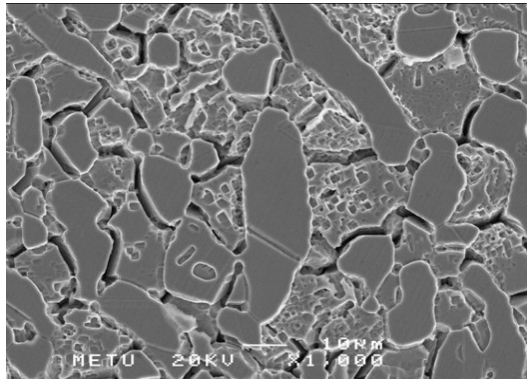
For shorter exposure times up to 3162 min, the regions of α -ferrite were partially decomposed into σ and γ_2 , but for longer ageing time of 10000min and above, the transformation showed a laminar structure of σ - and γ_2 -phases. The newly formed secondary austenite in

the eutectoid structure seemed to be easily etched away from the surface of specimens. This is probably due to depletion of chromium and molybdenum in the γ_2 -phase. As a result specimens aged for up to 3162 min a lot of small black pits around σ -precipitates inside ferrite regions were formed and consequently a sponge like or porous structure has developed. Sample aged for 10000 min shows eutectoid structure of finger like σ and γ_2 (etched away) phases (Figure IV-13(f)). In the case of ageing for 31622 min, the eutectoid structure of σ (coral-like structure) and γ_2 (etched away) phases were observed (Figure IV-13(g)).

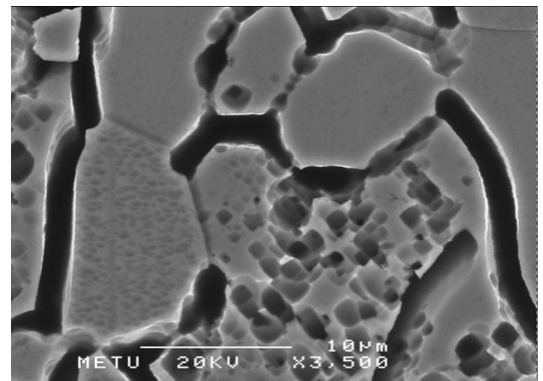
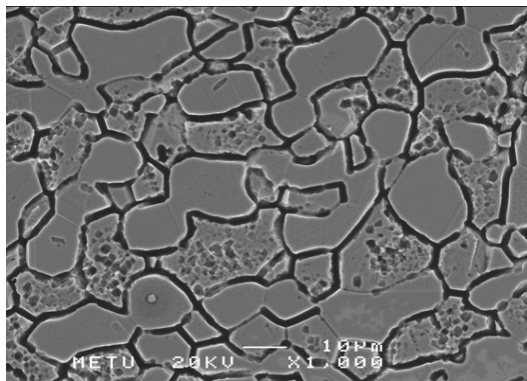
In all micrographs the secondary austenite was affected from oxalic acid. In comparing the micrographs of the structures etched with oxalic acid or subjected to weight loss acid test and DLEPR test, it can be concluded that there is a lower corrosion resistant area depleted in chromium and molybdenum due to the precipitation of σ -phase and in all cases the attack on secondary austenite is visible. A large number of pits were observed in the secondary austenite region after the weight loss acid test. The same region was also affected in the DLEPR test.



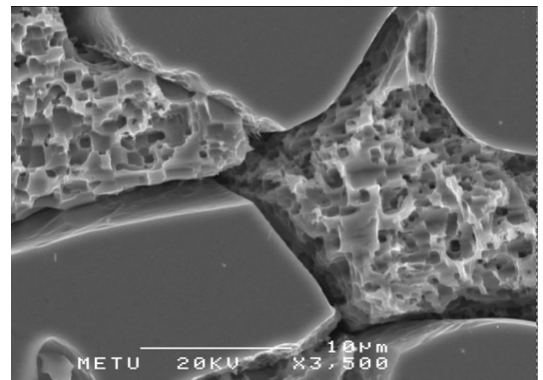
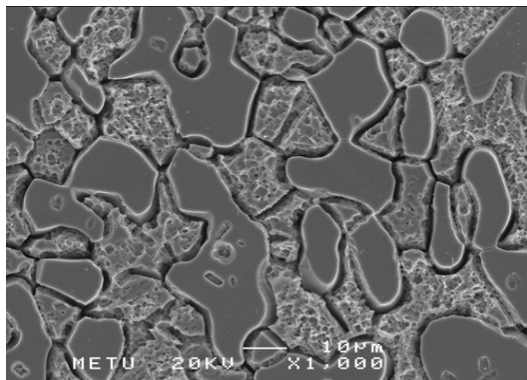
(a)



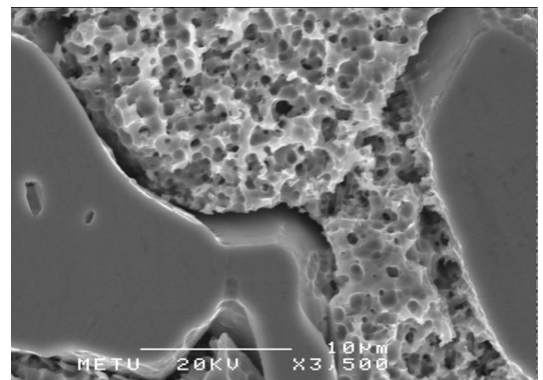
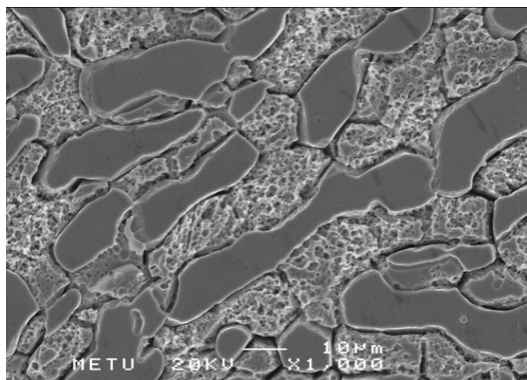
(b)



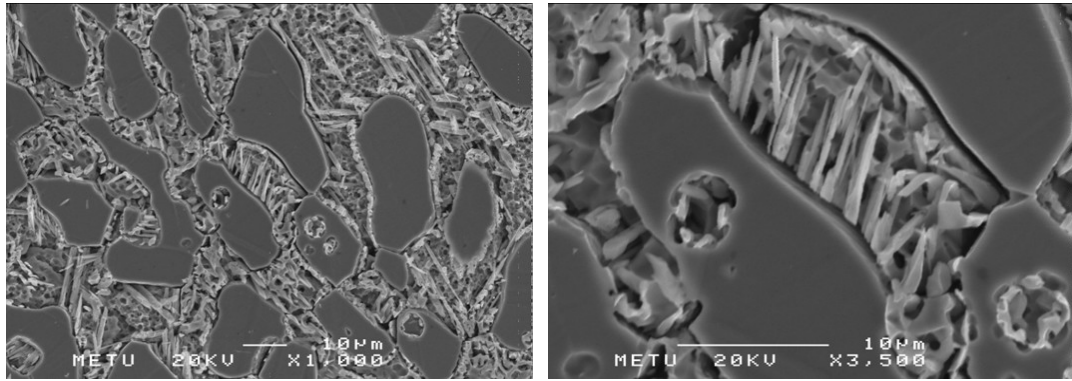
(c)



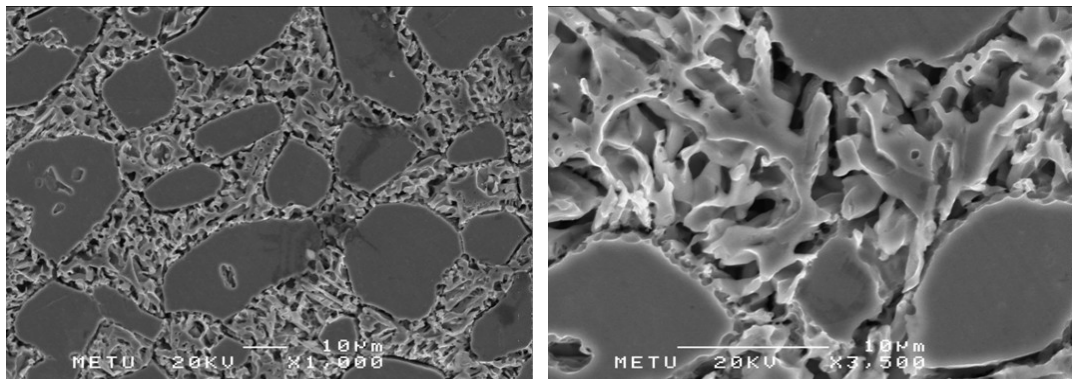
(d)



(e)



(f)



(g)

Figure IV-13. SEM images of specimens after electrolytically etching with oxalic acid: (a) solution annealed at 1050°C and water quenched; then aged at 650°C for (b) 100 min, (c) 316 min, (d) 1000 min, (e) 3162 min showing isolated sigma particles surrounded by the secondary austenite (spongy or porous structure), (f) 10000 min showing eutectoid structure of finger like σ and γ_2 (etched away) phases transformed from ferrite, (g) 31622 min showing the eutectoid structure of σ (coral-like structure) and γ_2 (etched away) phases transformed from ferrite.

The primary austenite (γ) with white contrast in the LOM of Figure IV-13(a) corresponds to the dark regions in the SEM image of Figure IV-13(b). In Figure IV-13(b-e) the regions of α -ferrite were partially decomposed into σ and γ_2 phases in the ageing times from 100

min to 3162 min. At 10000 min and above the transformation from α -ferrite to σ and γ_2 phases is indicated in Figure IV-13(d).

IV.6. EDS ANALYSIS OF PHASES

The precipitation of the sigma phase is accomplished by the formation of secondary austenite (γ_2). As the sigma phase forms, chromium and molybdenum are enriched in these precipitates and simultaneously nickel diffuses into the ferrite. The enrichment of γ -stabilizing elements (such as Ni) in the ferrite and the loss of α -ferrite stabilizing elements (such as Cr and Mo) lead to an unstable ferrite, transforming into secondary austenite which is depleted in chromium and molybdenum [86].

SEM micrographs of samples aged at 800°C are given in Figure IV-14. The sigma phase appears black, the ferrite dark gray and the primary austenite light gray. A bright region around the sigma phase is likely secondary austenite. Identification of the phases was confirmed by EDS analysis with SEM. The EDS results revealed the sigma phase to be chromium rich sigma and the bright phase to be depleted in chromium and molybdenum (Table IV-3) with respect to ageing temperature and time. The samples have revealed different phases with different chemical composition. For instance the EDS measurement of samples aged at 800°C for 316 min shows depletion of chromium from 26.32% to 20.26% and a nearly total loss of molybdenum. Chromium content of the σ -phase reaches to 30.76%.

The EDS measurements of Cr, Mo, Ni, Mn and Fe content of the α , γ , σ and γ_2 phases are given in Table IV-3. The relative concentration of major alloy elements across the secondary precipitates measured by

the line scanning are shown in Figures IV-14 and IV-15. The results indicate that the σ phase was partitioned in chromium and molybdenum where the secondary austenite is depleted in these elements. The previous optical identification of the phases presented in Section IV.1 was thus confirmed by this method (EDS).

Table IV-3. EDS analysis of the phases in DSS.

((*) unjustified data induced by the limitations of experimental technique)

Heat Treatment	Phase	Cr (wt%)	Ni (wt%)	Mo (wt%)	Mn (wt%)	Si (wt%)	S (wt%)	Fe (wt%)
Solution Annealed	General	22.04	4.45	2.69	1.49	0.45	0.003	68.29
Solution Annealed	α	26.32	4.87	4.15	1.59	0.74	-	62.32
	γ	23.55	7.08	-	1.85	-	1.19*	66.33
650°C / 31622min	σ	34.68	3.32	6.13	-	-	-	55.87
	γ_2	23.82	4.62	6.44*	-	0.78	-	64.34
725°C / 31622min	γ	23.81	6.43	-	-	-	-	69.76
	σ	35.21	-	7.21	-	-	-	57.58
	γ_2	23.03	6.91	-	-	1.04	1.26	67.75
	γ_2	18.65	5.21	-	-	-	-	76.14
800°C / 31622min	γ_2	22.03	6.10	2.27	2.05	0.56	-	66.98
	γ_2	19.97	7.20	-	2.22	0.72	-	69.90
	γ_2	20.23	6.29	-	2.41	-	-	71.08
	σ	32.15	2.26	6.66	1.80	0.71	-	56.41
	γ_2	21.92	6.16	-	1.95	-	0.80	69.17
800°C / 316min	α	27.71	3.47	-	-	0.55	0.98	67.28
	γ_2	26.97	2.77	-	-	-	0.91	69.36
	γ_2	20.26	4.76	-	2.10	0.61	-	72.28
	σ	30.76	3.36	7.88	1.80	0.71	-	55.50

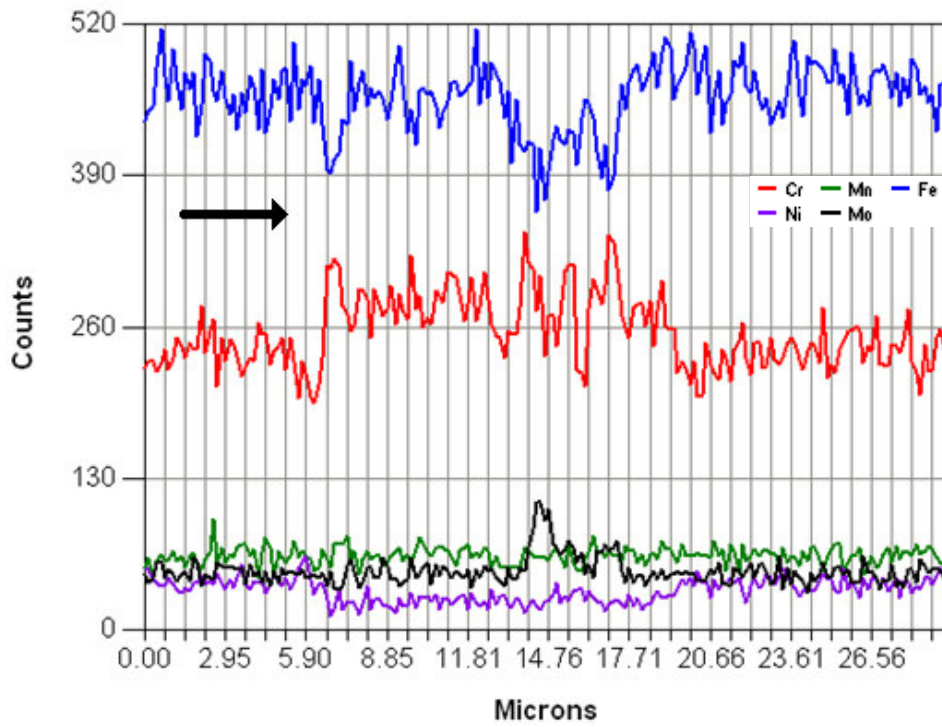
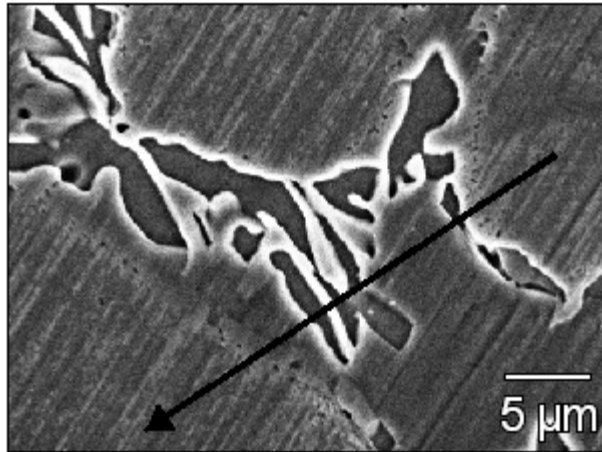


Figure IV-14. SEM image and profile line analysis of Cr, Ni, Mo, Mn, Fe for the sample aged at 800°C for 316 min showing chromium depleted areas due to the precipitation of σ -phase.

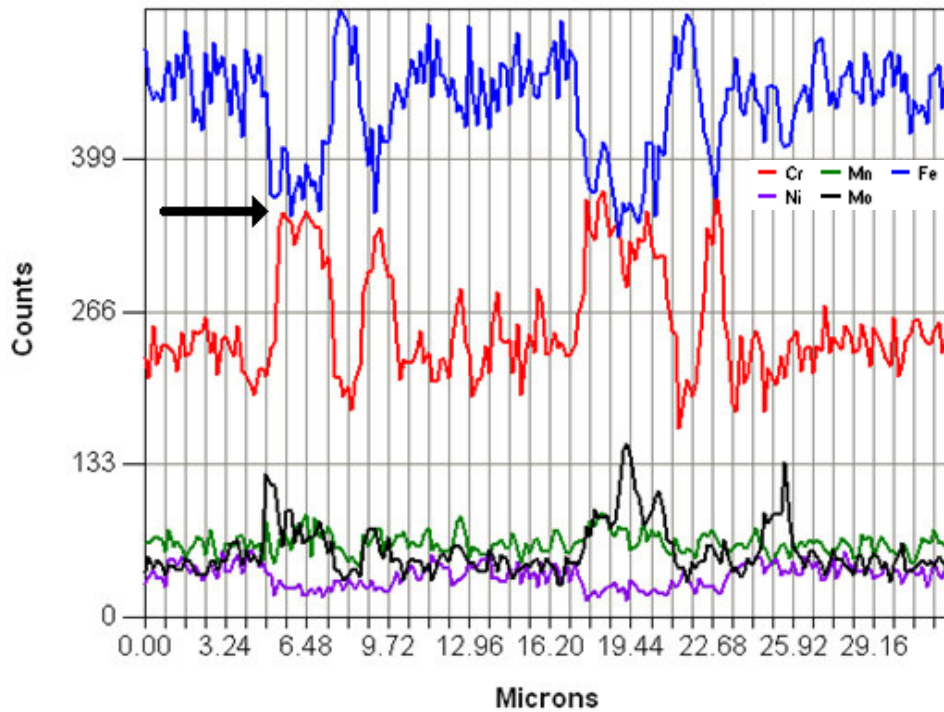
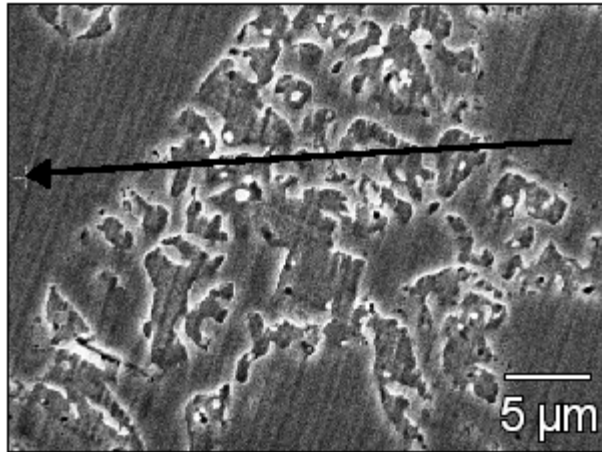


Figure IV-15. SEM image and profile line analysis of Cr, Ni, Mo, Mn, Fe for the sample aged at 650°C for 31622 min showing chromium depleted areas due to the precipitation of σ -phase.

IV.7. X-RAY DIFFRACTION PATTERN

The results of the X-ray diffraction experiments consist of a series of diffraction patterns. The diffraction pattern of the solution annealed parent alloy presents ferrite and austenite phase peaks only.

Samples aged at 650°C the diffraction patterns (Figure IV-16) do not show any peak corresponding to sigma phase even by the end of 3162 min. This may be due to the low volume fraction of the precipitated sigma phase. The X-ray sigma phase peak first appears after 10000 min of ageing. With increased ageing time the intensity of sigma peak increases. After longer periods of time such as 31622 minutes (22 days) the treatments promote the transformation of ferrite phase (Figure IV-16). This results in a noticeable decrease in the intensity of the α peaks and an increase of γ peaks. The decrease of the ferrite peak intensity indicates that the major fraction of ferrite is transformed into sigma. Consequently four sigma peaks are observed.

The diffractions patterns for samples aged at 725 and 800°C show sigma peaks first in 1000 and 100 min respectively. With increased holding time the intensity of sigma peaks increase and additional sigma peaks appear. With time one of the ferrite phase peaks decrease to nearly zero but the other peak does not disappear, it overlaps with sigma phase peak. This is in agreement with the previous works carried out by Elmer [87] and Chen [88] as shown in Figures IV-19 and IV-20. The changes in the diffraction peak intensity can be correlated with changes in volume fraction of each phase during the isothermal hold.

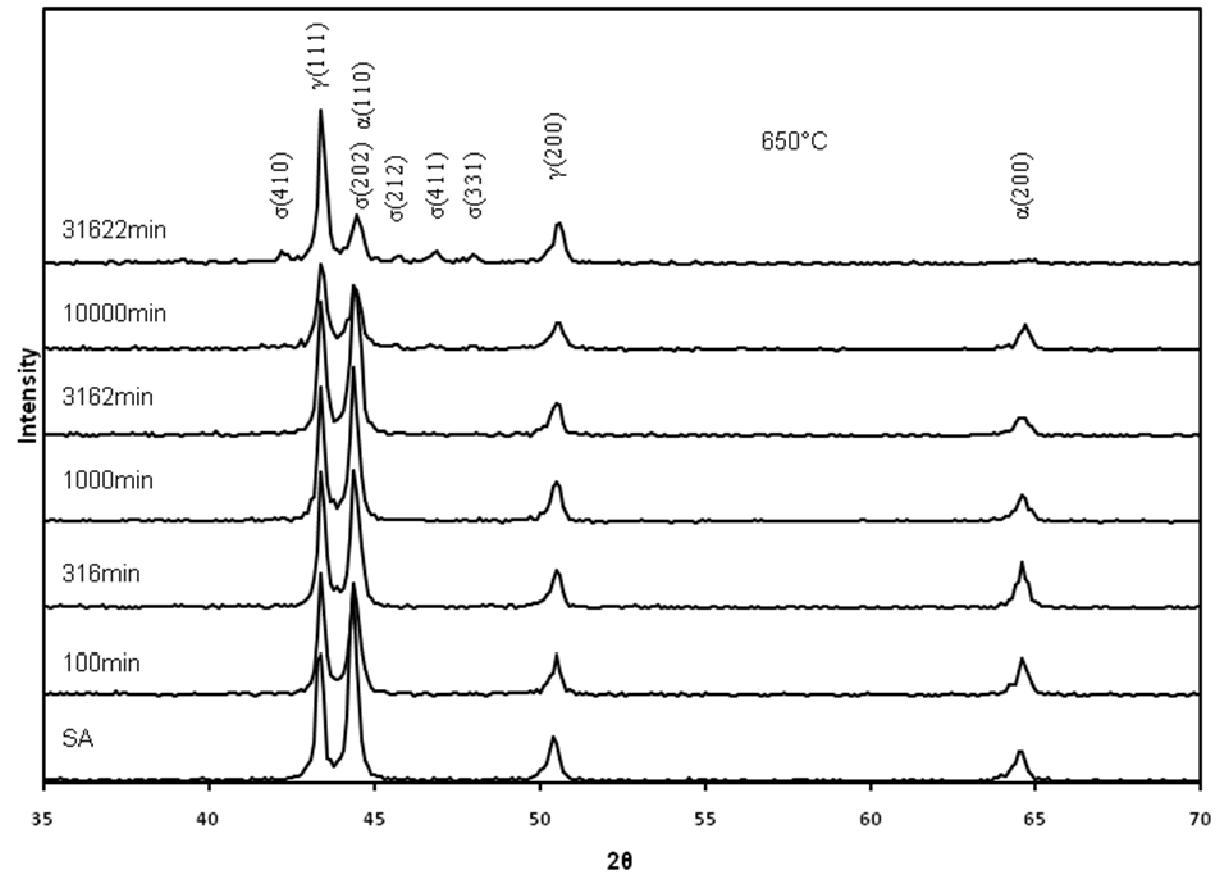


Figure IV-16. X-Ray diffraction pattern of samples annealed at 650°C.

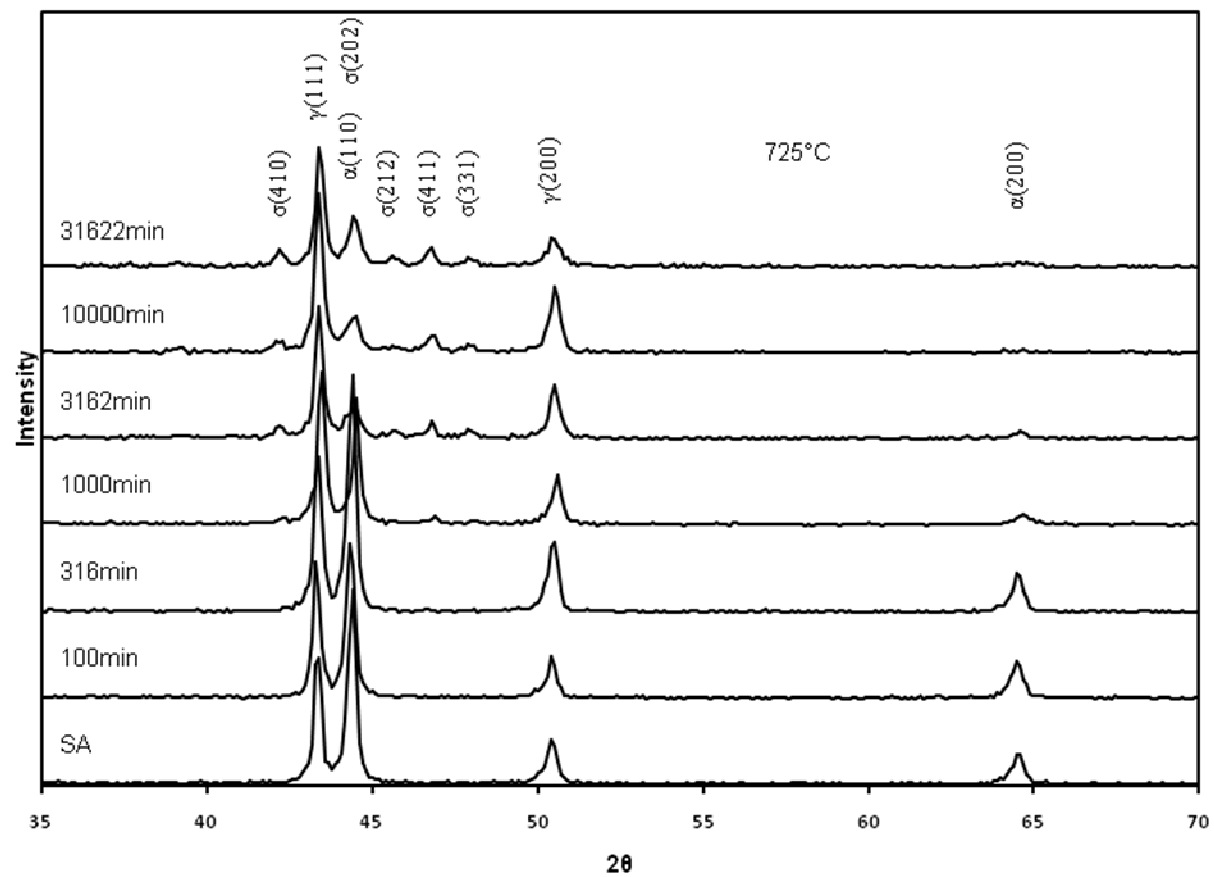


Figure IV-17. X-Ray diffraction pattern of samples annealed at 725°C.

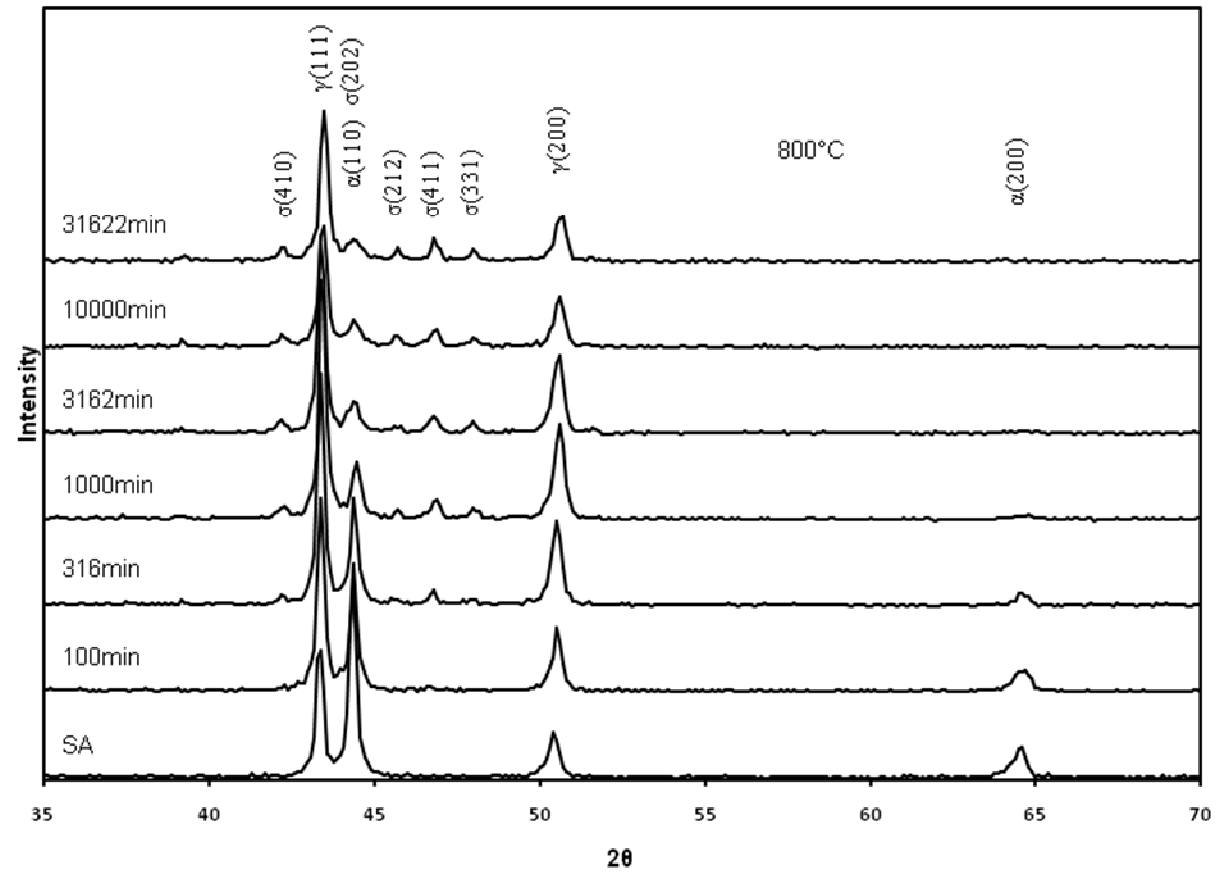


Figure IV-18. X-Ray diffraction pattern of samples annealed at 800°C.

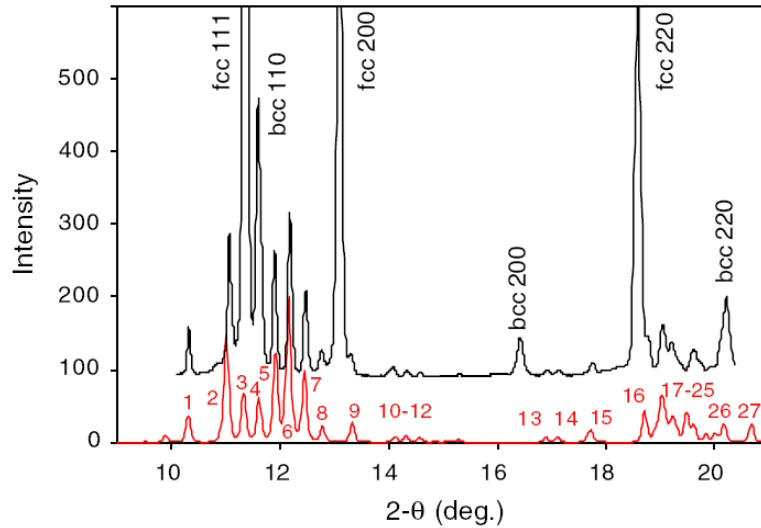


Figure IV-19. Comparison of diffraction pattern of sigma phase (black line) with the calculated diffraction pattern of the sigma phase (red line). Indexing numbers correspond to the sigma phase. Note that the sigma (330), peak 3, overlaps with the fcc (111), and that the sigma (202), peak 4, overlaps with the bcc (110) peaks [87].

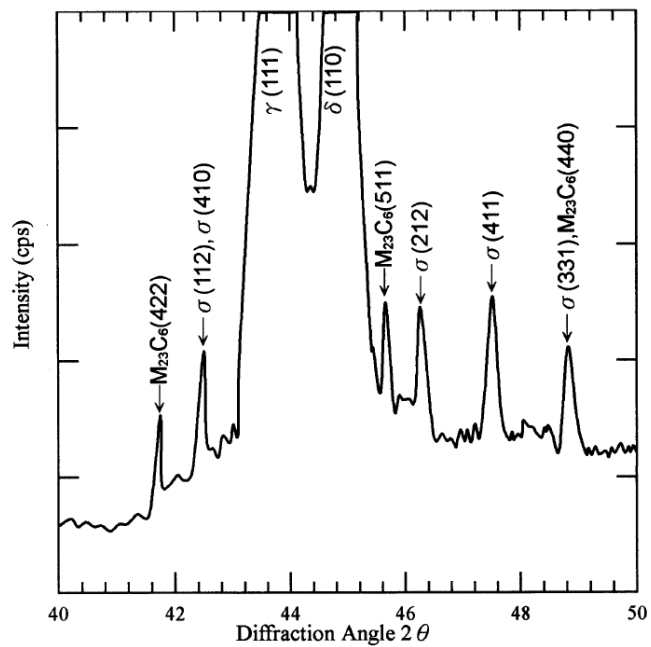


Figure IV-20. X-ray diffractogram showing the existence of σ and $M_{23}C_6$ precipitates [88].

Although the X-ray spectra of the aged samples for 100 and 316 min at 725°C do not reveal any sigma peak, the precipitations at grain boundaries are evident at 725°C for 316 min of ageing as shown in micrograph of Figure IV-3 (b). The X-ray diffraction analysis of the specimens aged at 800°C gives evidence of σ -phase precipitation already after 100 min of ageing (Figure IV-18). The decrease of the ferrite peak intensity indicates that the ferrite has transformed quickly to sigma at 725°C and 800°C. Carbides are not detected clearly because of low carbon content of the alloy [89].

IV.8. DLEPR RESULTS

The double loop electrochemical polarization reaction method is used to determine the sensitization behavior to local corrosion in DSS. Therefore the results of DLEPR test must somehow predict in the right manner, the state of the specimen as does the weight loss acid tests. In this regard, in order to determine what combination of DLEPR test parameters would give the best prediction, we correlate the results of the DLEPR and weight loss acid tests.

All samples in the solution annealed condition at 1050°C for 1 hour and heat treated (aged) at 650, 725 and 800°C for various times were tested by DLEPR. The test was performed by starting the sample from a potential lower than E_{corr} in the cathodic region. Then the potential is first scanned in the anodic direction from E_{corr} to a point of 0.250 V in middle of the passive region. The scanning direction is then reversed and the potential is reduced back to the cathodic region. As a result, two loops are generated, an anodic loop and a reactivation loop. The peak activation current (I_a) and the peak reactivation current (I_r)

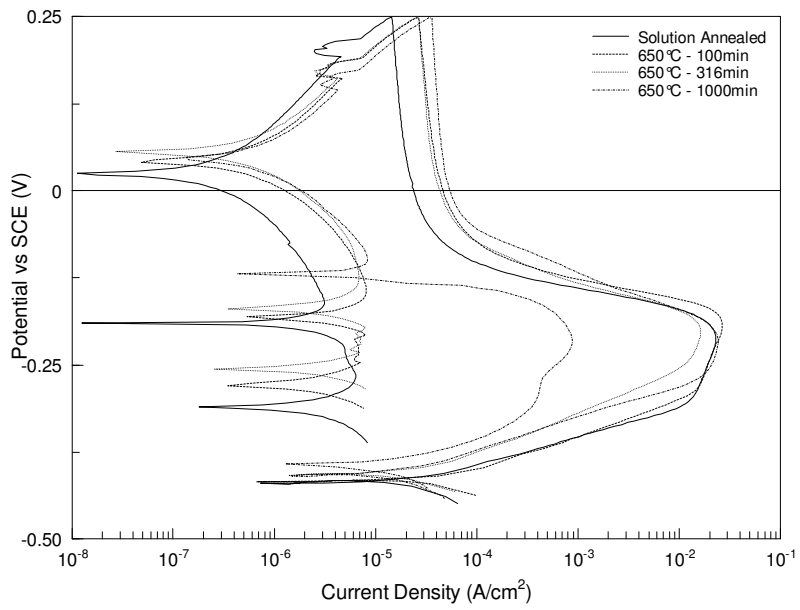
were measured during the forward and backward scans, respectively. The degree of sensitization (DOS) was measured as the ratio of the maximum current densities generated in the double loop test (I_r/I_a) x 100 [63, 90]. The activation or critical current density (I_a) or (I_{crit}) is proportional to corrosion rate of a metal. As the potential is increased to nobler value than the specimen open circuit potential (E_{corr}), the specimen behaves as anodic.

As a result the rate of corrosion (metal dissolution reaction) rises rapidly in the activation range up to the activation peak current density (I_a) is reached. The potential corresponding to this is called activation peak potential E_a or passivation potential E_{pass} .

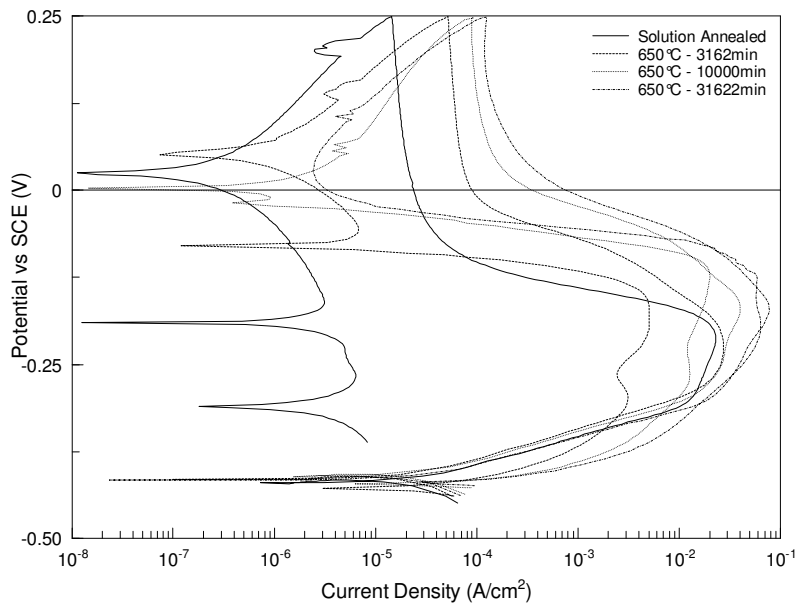
During the anodic sweep, the entire surface is active and contributes to the peak current. During the reactivation sweep, only the sensitized regions contribute to the passive-active transition. Thus in unsensitized specimens there is a small I_r , and therefore a small (I_r/I_a) ratio, while in heavily sensitized specimens, I_r approaches I_a , as shown in Figures IV-21, IV-22 and IV-23, giving a high (I_r/I_a) ratio.

If the potential is raised further, the anodic current will drop to a lower value called passivation current density (I_{pass}), and then it will remain constant over a wide potential range. This is the passive range, in which a thin, invisible film of oxide covers the metal surface. This protective film acts as a barrier between the metal and its environment and reduces the rate of dissolution.

Figures IV-21, IV-22 and IV-23 show the polarization curves for samples of solution annealed and aged at different temperatures and times.

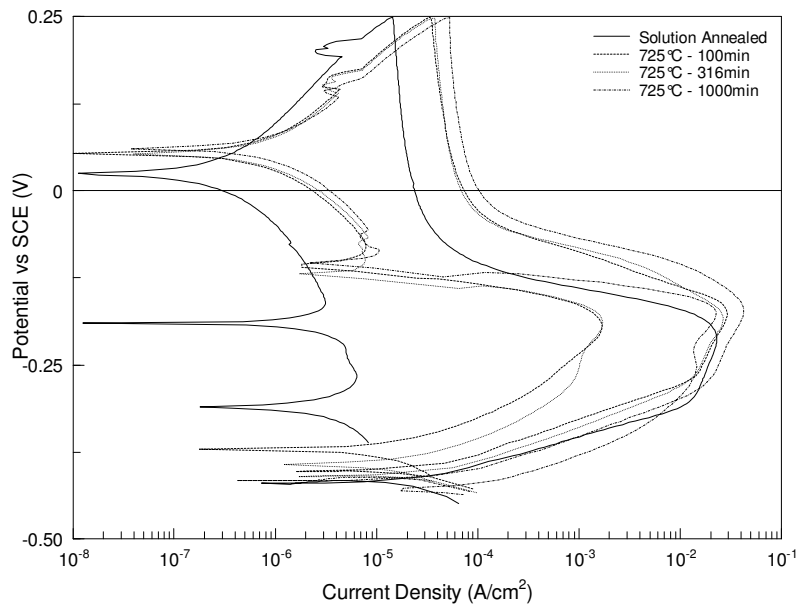


(a)

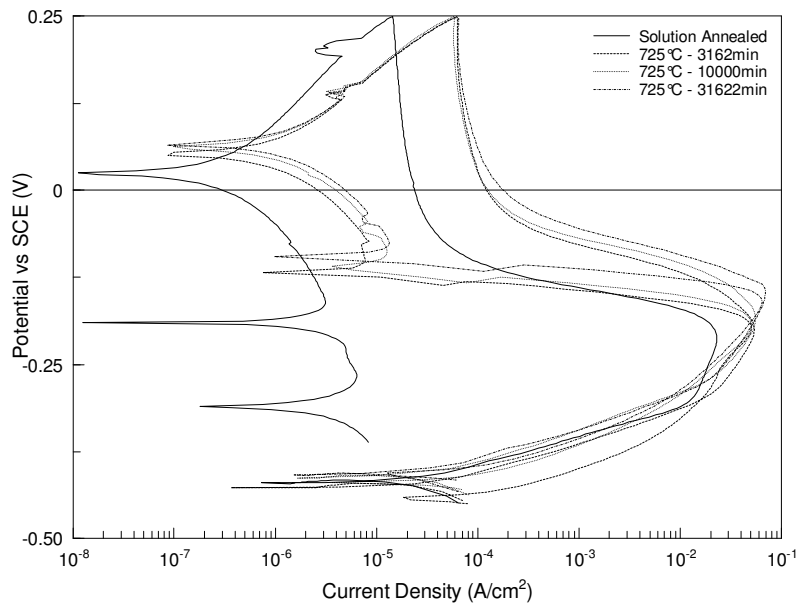


(b)

Figure IV-21. DLEPR curves plotted for DSS after solution and sensitization heat treatments at 650°C between 100 and 31622 min (scan rate:15V/hr).

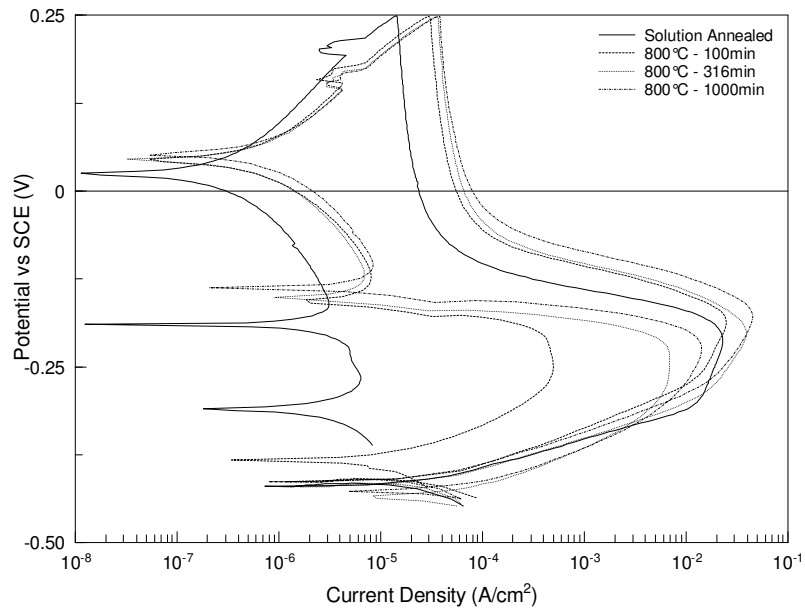


(a)

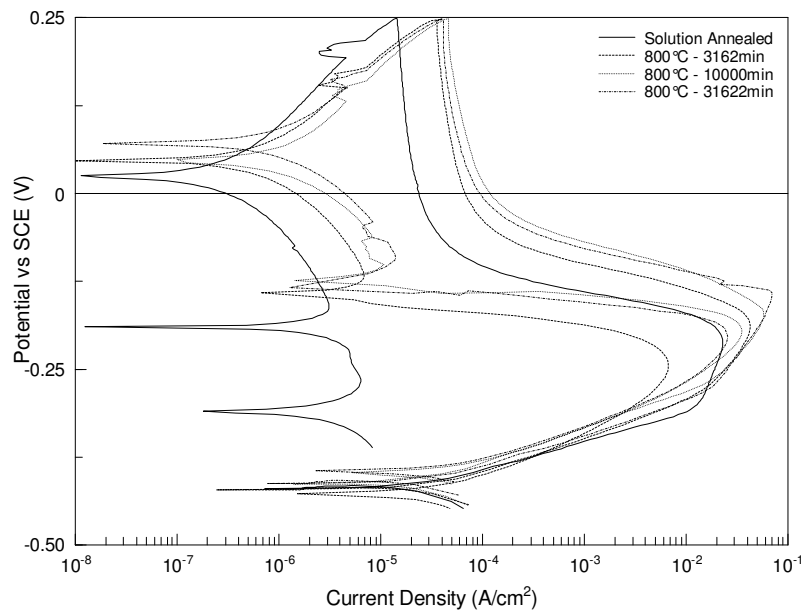


(b)

Figure IV-22. DLEPR curves plotted for DSS after solution and sensitization heat treatments at 725 °C between 100 and 31622 min (scan rate:15V/hr).



(a)



(b)

Figure IV-23. DLEPR curves plotted for DSS after solution and sensitization heat treatments at 800 °C between 100 and 31622 min (scan rate:15V/hr).

IV.8.1. DLEPR Test Results for Sample Solution Annealed at 1050°C for 1 hr

The curve obtained from the solution annealed sample is treated as a reference and compared with the others. The activation current density (I_a) of the reference curve increased proportionally with the corrosion rate of the alloy. The anodic current peak density is 23.13 mA/cm² and the corresponding activation peak potential E_a , or passivation potential E_{pass} is -212.78 mV. This peak may be attributed to the active dissolution of alloying elements. It then fell to a low passive current density (I_p) of 0.001448 mA/cm² before reaching to the chosen reverse potential ($E_{rev} = +250$ mV). The sample is thus passivated in a wide range between -212.78 mV and +250 mV. In this passive range a thin, invisible film of oxide may cover the metal surface. The protective film acts as a barrier between the metal and its environment and reduces its rate of dissolution. The I_r/I_a ratio is very low (0.027634 %). This may be considered as unsensitized material.

Only the solution annealed samples and the samples aged at 650°C for 100 and 316 min are unsensitized but samples aged at 650°C for 10000 and 31622 min are heavily sensitized. Similarly, samples after 1000 min of ageing at 725°C and samples after 316 min of ageing at 800°C are sensitized as well. The chromium replenishment of the depleted areas at 800°C is more pronounced than that of at 725°C. So the rate of corrosion and the degree of sensitization at 800°C are found lower than that of at 725°C.

IV.8.2. DLEPR Test Results for Samples Aged at 650 °C

Actually nucleation of precipitates (probably chromium carbides or nitrides and chi phase) occurs at α/γ interface although not optically visible (Figure IV-2). This leads to weak chromium depletion, resulting in a low sensitization because the I_r/I_a ratios are 0.033 and 0.058 % for 100 and 316 min of ageing respectively (Table IV-4). As the ageing time is increased to 1000 min fine precipitates of sigma phase first form in the ferrite phase and at the α/α and α/γ boundaries (Figure IV-2(c)). The I_r/I_a ratio 3.62 % being in line with the increase in corrosion rate to 0.50147 mdd. Similarly, the increase of ageing time to 3162 min results in an increase of DOS value to 18.57% accompanied with the rise of corrosion rate to 2.42 mdd (Table IV-2).

In specimens aged for 10000 and 31622 min the precipitates have grown as seen in Figures IV-2 (e, f). The precipitation affects the corrosion behavior by the depletion of chromium and molybdenum around its immediate vicinity. This leads to a high I_r/I_a ratio of 49.71 and 82.42% for 10000 and 31622 min of ageing respectively. So the samples are heavily sensitized.

Polarization curves for unsensitized samples resemble each other but they are different from that of sensitized material. When the polarization curves of the samples aged at 650 °C are compared with the reference curve, it is seen that the anodic peak current densities increase with increasing ageing times (Table IV-4). The passive current densities change from 0.025313 mA/cm² up to 0.1194 mA/cm² with ageing time from 100 to 31622 min respectively. The passivation potential (E_{pass} or E_{pp}) is also ranged from -212.78 mV to -172.23 mV with the same time interval.

Table IV-4. DLEPR Test results of the duplex stainless steel

Temperature (°C)	Time (min)	Activation Peak Potential, E _a (mV)	Activation Peak Current Density, I _a (mA/cm ²)	Reactivation Peak Potential, E _r (mV)	Reactivation Peak Current Density, I _r (mA/cm ²)	Passivation Current Density, I _{pass} (mA/cm ²)	DOS (I _r /I _a x100)
Solution annealed at 1050°C, 1 hr		-212.78	23.1304849	-267.33	0.0063918	0.001448	0.027634
Solution annealed at 1050°C, 1 hr and Aged at 650°C	100	-194.27	26.7204689	-227.99	0.0089320	0.025313	0.033428
	316	-201.59	16.2439211	-196.26	0.0095722	0.026611	0.058928
	1000	-214.66	24.1534434	-218.19	0.8752141	0.033795	3.623558
	3162	-229.56	27.4257333	-182.82	5.0936324	0.051553	18.572456
	10000	-169.23	40.3219057	-122.00	20.0460371	0.089166	49.715004
	31622	-172.23	77.7148929	-194.00	64.0553114	0.119407	82.423470
Solution annealed at 1050°C, 1 hr and Aged at 725°C	100	-178.33	29.2261754	-196.13	1.6857088	0.033688	5.767805
	316	-185.25	26.5737074	-189.43	1.7231466	0.037542	6.484404
	1000	-172.22	42.2727750	-177.35	22.5825614	0.052615	53.421053
	3162	-199.68	54.2137581	-195.70	50.5214698	0.062409	93.189389
	10000	-183.47	55.7856777	-191.11	50.4425582	0.057675	90.422059
	31622	-147.94	69.6430296	-160.30	64.3463484	0.059391	92.394528
Solution annealed at 1050°C, 1 hr and Aged at 800°C	100	-187.31	24.9231381	-249.84	0.498463	0.029998	1.999934
	316	-203.12	39.2419267	-238.16	6.9135766	0.035334	17.617832
	1000	-179.68	44.7944482	-224.01	14.1895596	0.038004	31.677025
	3162	-187.67	42.6067788	-245.27	6.58075448	0.035494	15.680028
	10000	-172.55	57.9448930	-197.77	35.3551309	0.046062	61.015094
	31622	-145.65	69.4685293	-204.05	25.5835941	0.040190	36.827603

The differences in the anodic peak current densities, passivation potentials and the passivation current densities as compared to the reference polarization curve of the solution annealed sample are the result of the varying degree of sensitization. The higher values of I_a or I_{pass} or E_{pass} is a direct indication of the worsening of corrosion properties.

Some dissolution of ferrite may also occur where the corroded areas appear in black (Figure IV-2). It is observed that the sigma and austenite phases are not almost intact, while the secondary austenite (γ_2) and some iron rich ferrite phases are attacked. The secondary austenite is poorer in chromium as compared with the primary austenite (Table IV-3). Since it originates from the primary ferrite phase [91]. Therefore, the secondary austenite around the sigma phase can degrade the stability of a passive film [92].

IV.8.3. DLEPR Test Results for Samples Aged at 725 °C

Similar behavior takes place during ageing at 725 °C and 800 °C. However shorter times were required at higher temperatures to produce the same microstructural changes. This results in less exposure time to attain sensitization.

With ageing to 100 min, carbides, nitrides and chi phases nucleate at the α/γ boundaries but they are not visible (Figure IV-3). Upon increasing the ageing time to 316 min, in addition to carbides, nitrides and chi phase, sigma phase nucleation starts at α/γ phase boundaries. As a result the I_r/I_a ratio is 6.48% and mdd value is 2.37.

After 1000 min, the σ precipitates have grown at the boundaries and within the ferrite grains. Next to the growing σ -phase the secondary austenite (γ_2) forms from the decomposition of ferrite. 41 % of ferrite

has transformed into σ and γ_2 (Table IV-1). Dissolution of the secondary austenite results in greater weight loss (5.38 mdd) and a high ratio of I_r/I_a (53.42%). From the appearance of the surface after immersion test some ferrite phase is said to be affected.

After 3162 min of ageing 72.5 % of the ferrite is decomposed and most of it is transformed into σ -phase (Table IV-1). This causes a substantial decrease in chromium content of the interfaces and around the precipitates. This leads to highest grade of sensitization at 725°C so that the DOS value reaches 93.189 % (Table IV-4.) and dissolution of the secondary austenite results in a corrosion rate of 5.161 mdd (Table IV-2).

The amount of ferrite decomposed increases from 89 to 100 % upon increase the ageing time from 10000 to 31622 min respectively. The corresponding DOS values (90.4 and 92.39 %) and the corrosion rates (5.28 and 6.04 mdd) are indicative of heavy sensitization.

IV.8.4. DLEPR Test Results for Samples Aged at 800°C

When aged for 100 min, very few precipitates were observed. After 316 min of ageing a lot of precipitates are developed at α/γ and α/α boundaries and inside the ferrite grains. The DLEPR and weight loss acid immersion tests reveal that the undesired secondary austenite at α/γ boundaries together with regions next to sigma in the ferrite phase is affected. In contrary to lower temperatures the samples aged at 800°C exhibit lower DOS (31-61%) mainly for exposure times between 1000 and 31622 min.

The growing sigma phase consumes chromium and molybdenum not only from the ferrite, but also from the primary austenite and leaves a region depleted in chromium [93]. This is an

undesirable phase and reduces the corrosion resistance and makes the alloy more susceptible to localized attack. Longer ageing treatment such as 1000, 3162, 10000 and 31622 min led to coarsening of the sigma phase and slowed the corrosion rate to 4.99, 4.64, 4.80 and 5.09 mdd respectively (Table IV-2). A possible explanation for this is that increasing ageing temperature to 800°C promotes a redistribution of chromium in depleted zones [94]. In other words this may be due to the replenishment of the secondary austenite by chromium diffusion from the chromium rich ferrite phase and from the interior of the austenite. As a result prolonged ageing at 800°C causes a decrease in DOS and hence a decrease in susceptibility to intercrystalline corrosion

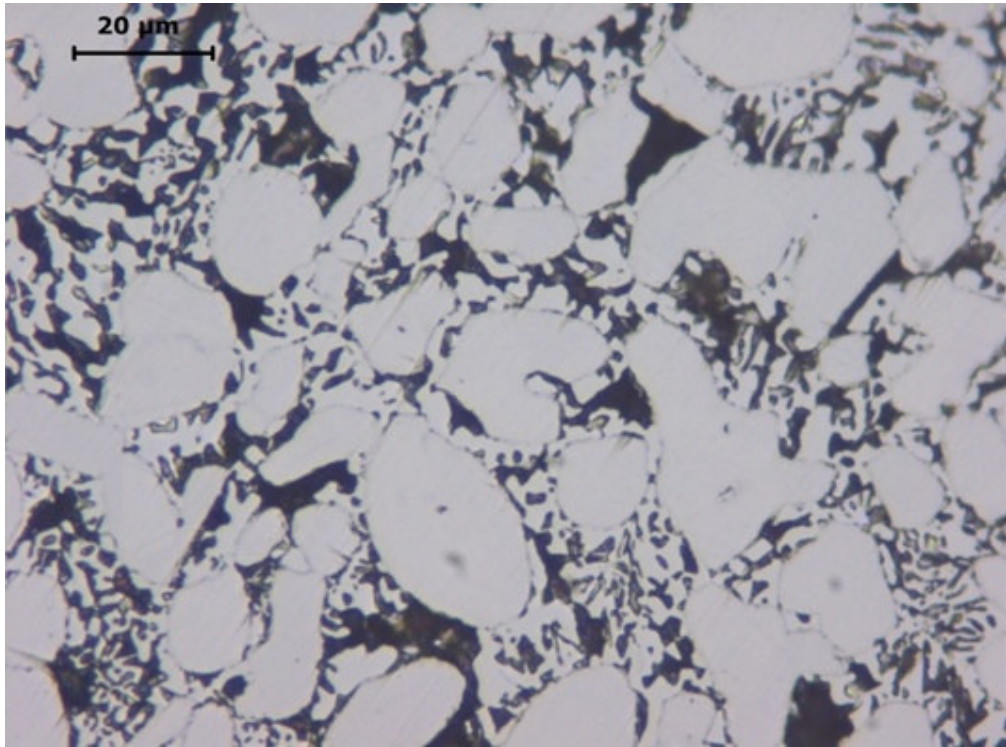
IV.8.5. Micrographs of DLEPR Test Samples

After DLEPR test, some samples were slightly polished and examined with LOM (Figures IV-24-26). The close observation of the surface indicates that the sigma and austenite phase are almost intact, while the secondary austenite and some iron rich ferrite phase are attacked. The corroded secondary austenite regions appear in black and the isolated sigma precipitates in white. Large primary austenite grains remain in white as usual. To distinguish sigma and primary austenite phases in color, the samples were electrolytically etched with NaOH reagent. The sigma phase is colored reddish brown and distinguished from the primary austenite which is not affected from the etchant.

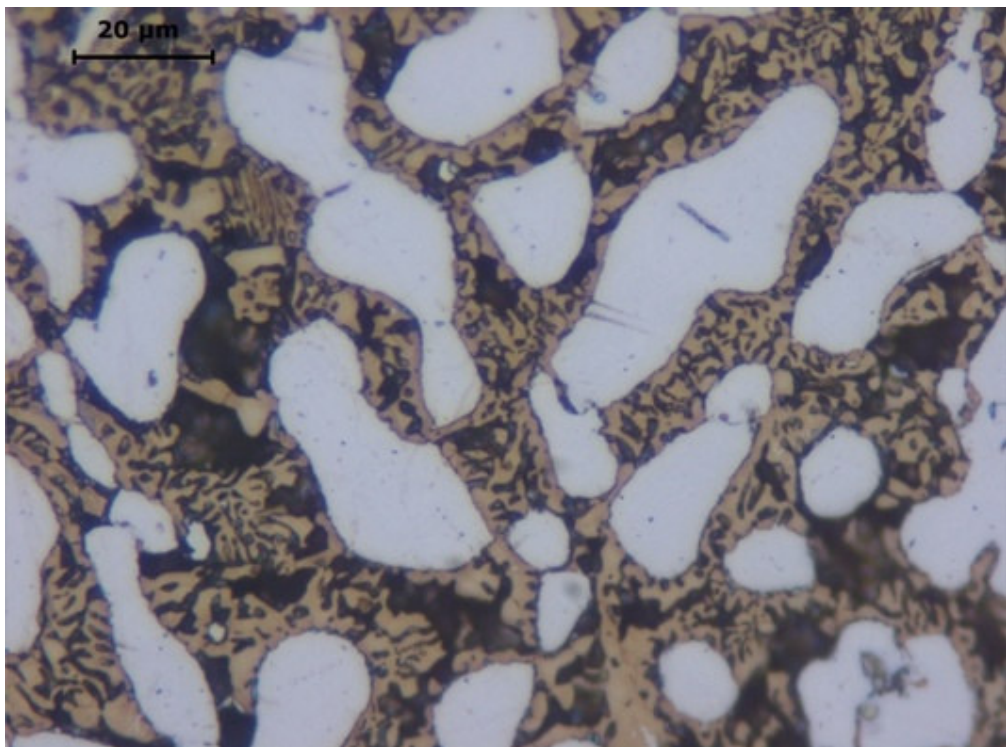
After the DLEPR test, black regions produced in the secondary austenite by corrosion attack were observed. The attack on samples aged at 800°C for 1000 min was less extensive and more superficial, while the attack was deeper on samples aged for 10000 min. In the

case of ageing at 725°C a deep attack was also observed on samples aged for 31622 min. In all cases the chromium depleted zone was the corroded region. These results are in acceptable agreement with the immersion test results.

Considering the sigma phase occurrence with ageing time, it is obvious that the state with more sigma phase and secondary austenite means worse corrosion resistance as shown in DLEPR and immersion test results. The distribution of the corroded areas corresponds to the distribution of the secondary austenite in the ferrite grains. Especially at the α/γ grain boundaries and inside the ferrite grains where isolated sigma precipitates are accumulated, pitting or corroded areas are more pronounced. These pits can grow together and form a hole in the secondary austenite region. Due to further attack, large areas covering many primary austenite and sigma phase regions are affected and big cavities were formed.

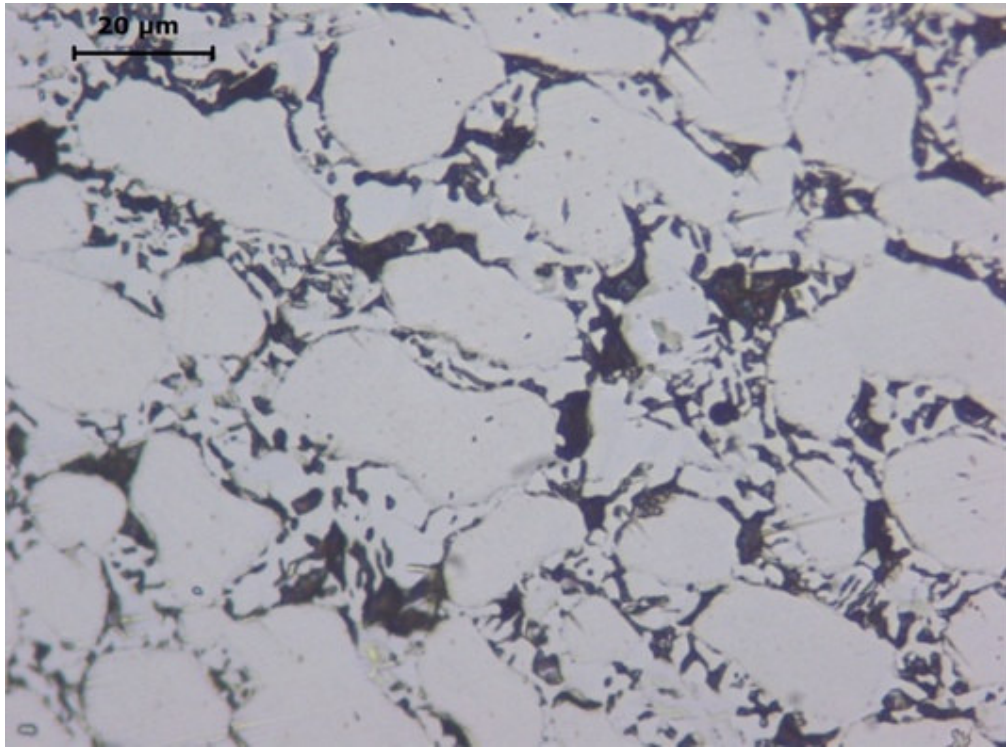


(a)

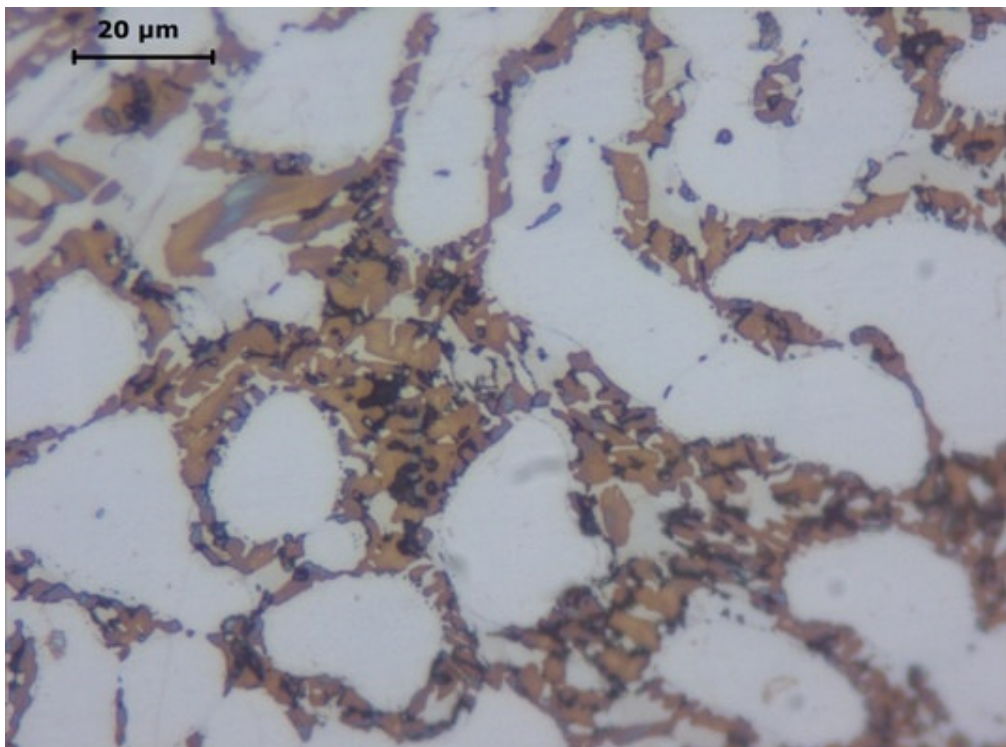


(b)

Figure IV-24. Optical micrographs after DLEPR test for sample aged at 725°C for 31622 min (a) after slightly polished (b) electrolytically etched with NaOH.

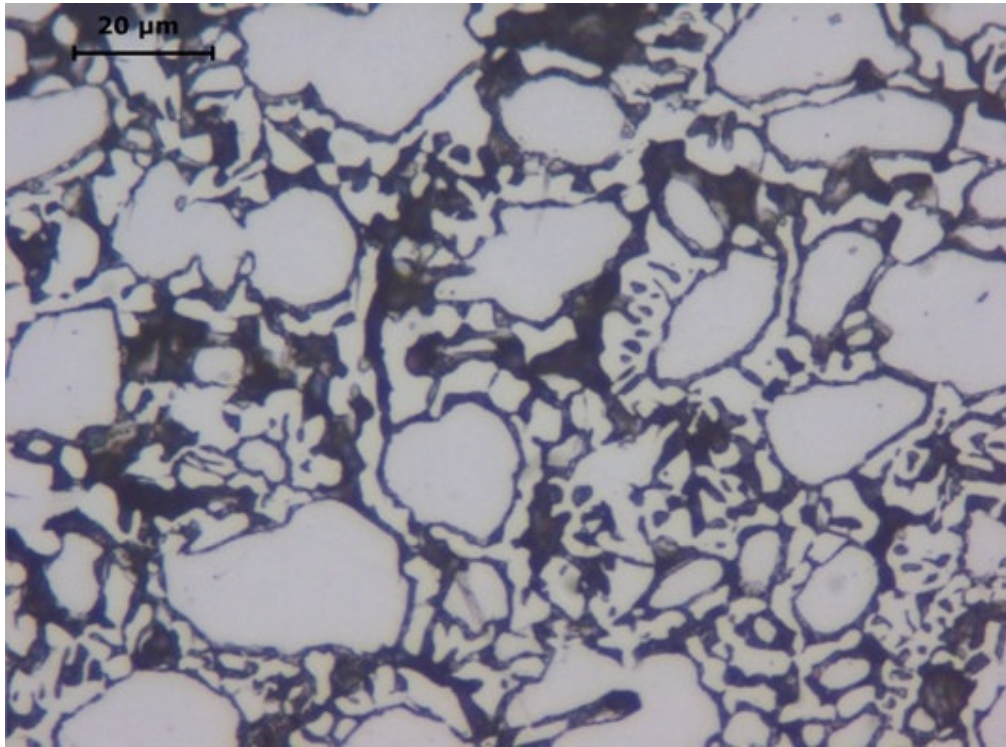


(a)

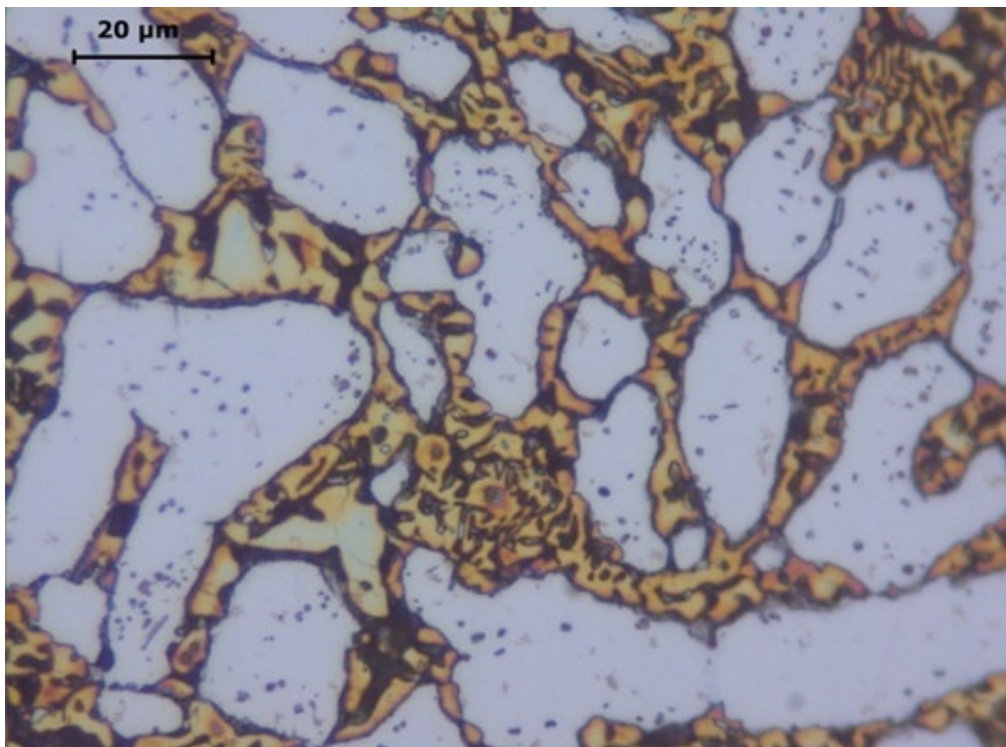


(b)

Figure IV-25. Optical micrographs after DLEPR test for sample aged at 800°C for 1000 min (a) after slightly polished (b) electrolytically etched with NaOH.



(a)



(b)

Figure IV-26. Optical micrographs after DLEPR test for sample aged at 800°C for 10000 min (a) after slightly polished (b) electrolytically etched with NaOH.

IV.9. ANALYSIS OF POLARIZATION CURVES IN REVERSE SCANNING

At the beginning of the reverse scanning, the anodic current density decreases and the anodic curve move to the left (Figure IV-21). This is an indication of thickening of the oxide film. On decreasing the potential the anodic current density is reduced nearly to zero. This is due to the slowing of the anodic dissolution kinetics caused due to thickening of the passive film. The sample has thus continued to passivate from E_{pass} through E_{rev} back to potential E_3 . Further reducing the potential, the direction of the current density has changed between E_3 and E_4 as shown in Figure IV-27. It shows a loop consisting of cathodic current [60]. The origin of the cathodic current can be attributed to the fact that at potentials between E_3 and E_4 the rate of the cathodic reaction is greater than the anodic current density and hence the net current is cathodic over the potential range, $\Delta E (=E_3-E_4)$ (Table IV-5). If the potential is further reduced on the reverse scan, the direction of the current density changes back and an anodic reactivation loop is generated. This indicates that the oxide has dissolved and metal dissolution reaction has occurred. The development of the reactivation peak current density can be attributed to metal dissolution. The lowered reactivation peak current density I_r (on the reverse scan) is due to incomplete reactivation of the metal surface.

If no cathodic loop were generated on the reverse scan the anodic reactivation would begin at higher potential and would likely reach in a short time to a high value of I_r and thus the metal dissolution would take place.

The same cathodic loop behavior is observed on the reverse scans of polarization curves obtained from the solution annealed and aged samples by DLEPR test (Table IV-5).

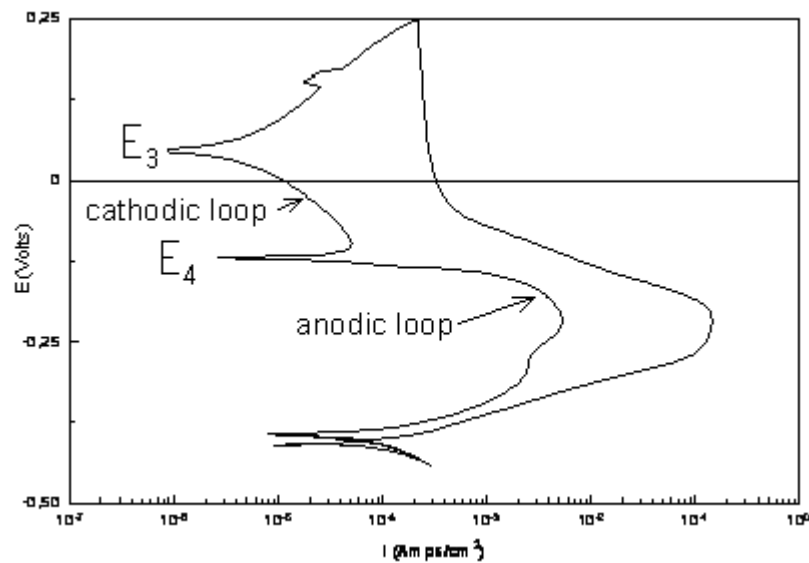


Figure IV-27. Cathodic and anodic loops during backscan.

Samples aged at $650^\circ C$ for 100 and 316 min the potential range (ΔE) that the cathodic loop is obtained are 0.22130 V and 0.22558 V respectively. These are very close to that of the solution annealed sample. Their reactivation curves look like that of the solution annealed sample. Similar cathodic loop behavior was observed for all cases. Since the precipitates during ageing are not visible, the influence of the microstructure on the polarization behavior is not evident.

Table IV-5. DLEPR test results on the reverse scans of polarization curves.

Heat Treatment	Time (min)	E ₃ (volt)	E ₄ (volt)	ΔE (=E ₃ -E ₄) (volt)	I _r (mA/cm ²)	DOS (I _r /I _a x100)
Solution annealed at 1050 °C, 1 hr		0.02521	-0.190090	0.215300	0.0063918	0.027634
Solution annealed at 1050 °C, 1 hr and Aged at 650 °C	100	0.040478	-0.180830	0.221308	0.0089320	0.033428
	316	0.055869	-0.169720	0.225589	0.0095722	0.058928
	1000	0.048454	-0.119260	0.167714	0.8752141	3.623558
	3162	0.050540	-0.079508	0.130048	5.0936324	18.572456
	10000	0.003096	-0.017805	0.020901	20.0460371	49.715004
	31622	-	-	-	64.0553114	82.423470
Solution annealed at 1050 °C, 1 hr and Aged at 725 °C	100	0.053818	-0.110000	0.163818	1.6857088	5.767805
	316	0.052163	-0.119650	0.171813	1.7231466	6.484404
	1000	0.060101	-0.103310	0.163411	22.5825614	53.421053
	3162	0.050114	-0.117800	0.167914	50.5214698	93.189389
	10000	0.063035	-0.108430	0.171465	50.4425582	90.422059
	31622	0.064701	-0.095247	0.159948	64.3463484	92.394528
Solution annealed at 1050 °C, 1 hr and Aged at 800 °C	100	0.045932	-0.15449	0.200422	0.4984463	1.999934
	316	0.045098	-0.15130	0.196398	6.9135766	17.617832
	1000	0.050937	-0.13741	0.188347	14.1895596	31.677025
	3162	0.046346	-0.14173	0.188076	6.68075480	15.680028
	10000	0.048046	-0.12440	0.172446	35.3551309	61.015094
	31622	0.070888	-0.13465	0.205538	25.5835940	36.827603

Therefore on the reverse scan similar behavior as the solution annealed sample was observed. The peak reactivation current density (I_r) is 0.00893 and 0.00957 mA/cm² respectively. The lowered critical reactivation current density (I_r) on the reverse scan is due to incomplete activation of the metal surface.

For samples aged for 1000 min the potential range (ΔE) for the cathodic loop is 0.16770 V. This is less than that of the solution annealed sample. This means that the formation of the cathodic loop delays the occurrence of the anodic reactivation current loop for a short time. Then the direction of the current density changes back quickly and the anodic reactivation current density begins to be generated at a potential of $E_4 = -0.119260$ V. It reaches to the peak value of $I_r = 0.875$ A/cm². The DOS value is 3.62%.

For the sample aged for 3162 min the range of potential for the cathodic loop is 0.13 V. This is lower than the value measured for the solution annealed one. The dissolution of oxide begins at a high potential such as $E_4 = -0.079508$ V. After a short delay the reactivation current density increases to $I_r = 5.09$ mA/cm². The DOS value is 18.57 %.

For ageing time of 10000 min a cathodic loop on the reverse scan is obtained within a very narrow potential range of 0.0209 V. And then the anodic reactivation loop suddenly begins at a potential of $E_4 = -0.017805$ V. This potential is higher as compared to the potentials obtained from the samples aged for 3162 and 1000 min. The reactivation peak current density (I_r) has reached to 20.046 mA/cm² corresponding to a high DOS value (49.71 %). E_4 values have found higher with increasing ageing time where E_3 changes disorderly.

The chromium depletion or dissolution of secondary austenite (γ_2) phase causes the passive current densities (I_{pass}) to shift to higher current densities (Figure 21, Table IV-4).

Due to longer ageing treatments for 1000, 3162 and 10000 min, more sigma precipitates and secondary austenite are formed. The change in the microstructure affected the polarization curve, so that the potential range for the cathodic loop decreased and the anodic reactivation began at higher potentials.

The sample aged for 31622 min is scanned in the reverse direction, the passive film thickens more but the thickness is not sufficient to reduce the anodic current density which may explain the absence of a cathodic loop. Upon the reverse scanning the anodic reactivation current density increases until the peak current density of $I_r = 64.055 \text{ mA/cm}^2$ is reached. The higher anodic peak reactivation current density is the result of complete activation of the metal surface as evident by the highest DOS value (82.42 %).

The reverse scan behavior of samples aged at higher temperatures was similar. For samples aged at 725°C for different time intervals from 100 to 31622 min, the potential ranges (ΔE) for the cathodic loops are all close to each other. As soon as the cathodic loops are formed for a short time the anodic reactivation loops began to be generated at higher potentials (Table IV-5). This was also the case for samples aged at 800°C for times from 100 to 10000 min (Table IV-5). The E_3 and E_4 were changed disorderly with increasing ageing time. The passive current densities (I_{pass}) shift to higher current densities because of the chromium depletion or dissolution of secondary austenite (γ_2) phase

In all cases the cathodic loops delay the occurrence of the anodic reactivation loops. The anodic reactivation peak current densities increased constantly until the peak current densities (I_r) were reached. The I_r values depend closely on the dissolution reaction of the phases in the metal, since during the reactivation sweep only the sensitized areas (chromium depleted secondary austenite) contribute to the passive – active transition.

Due to the limited replenishment of Cr-depleted zone at 800 °C, the potential range for cathodic loops were larger and the E_4 values are found lower than those obtained at 725 °C. This is why the occurrence of the anodic reactivation loop were delayed more. The anodic reactivation peak current densities at 800 °C for all ageing times were also found lower than that obtained at 725 °C because of the incomplete activation of metal surface for the same reasons. This resulted in lower DOS values as well.

From the observations of the polarization curves it may be concluded that cathodic loops are not directly related with metal dissolution. They merely delay the occurrence of anodic loops for a short time. Potential ranges over which the cathodic loops extend depend on the protective film thickness and microstructural changes in the material caused by applied heat treatments.

CHAPTER V

CONCLUSIONS

The effect of isothermal treatment in the temperature range 650°C-800°C on the microstructural evolution and consequent corrosion behavior of a DSS was investigated. The important findings are summarized as follows;

1. The evidence shows that the intermetallic σ -phase is first precipitated at the interface of α/γ , α/α and inside the α -ferrite grains. The ageing times needed for the formation of this phase depends on the ageing temperature being 1000, 316 and 100 min for temperatures 650, 725 and 800°C respectively. The σ -phase grew into coarse particles due to high diffusivity of chromium and molybdenum atoms in the ferritic structure.

2. The exposure of aged samples to iron-chloride aggressive media leads to a localized and selective attack of the previous ferrite zones, partially transformed to new austenite.

3. The solution annealed samples and the samples aged at 650°C for up to 316 min are unsensitized. However, the degree of sensitization increases rapidly with the increasing ageing time.

4. Contrarily, a heavily sensitized structure is generated at 725 and 800°C following the ageing treatment for durations of 1000 and 316 min respectively.

5. The chromium replenishment of the depleted areas at 800°C is more pronounced compared to that at 725°C. Accordingly, the degree of sensitization at 800°C is lower than that of at 725°C.

6. When the data obtained from digital image analysis and DLEPR tests are considered, a good correlation was found between the sigma phase percent and DOS values. The correlation coefficients are 0.978, 0.974 and 0.917 for 650, 725 and 800°C respectively.

7. The weight loss acid test and DLEPR test show good correlation also especially for 650°C. The coefficients are 0.959, 0.885 and 0.677 for 650, 725 and 800°C respectively. The poorer variation of 725 and 800°C may be due to the replenishment of chromium.

8. From the observations of the polarization curves it may also be concluded that cathodic loops are not directly related with metal dissolution. They merely delay the occurrence of anodic loops for a short time. Potential range for which the cathodic loops are obtained depend on the protective film thickness, ageing temperature and time and thus the microstructural changes in the material.

REFERENCES

1. A. Wensley, C. Reid, in *Duplex Stainless Steels '91*, J. Charles, S. Bernhardsson eds., Les Editions de Physique, 1099, (1992).
2. J. Husbands, P. K. Whitkraft, *CORROSION/91, Paper 171*, NACE, Houston, (1991).
3. D. J. A. Fruytier, in *Duplex Stainless Steels '91*, J. Charles, S. Bernhardsson eds., Les Editions de Physique, 499, (1992).
4. P. Jolly, *Bulletin du Cercle d'Etudes des Metaux*, XII-5, 317, (1973).
5. N. Parvathavarthini, R. K. Dayal, *Journal of Nuclear Materials*, **305**, 209, (2002).
6. R. D. Thomas, *Weld Res J*, **24**, (1984).
7. R. D. Thomas, *Suppl Weld Res J*, **355**, (1984).
8. C. F. Meitzner, *Weld Res Council Bull*, 211, 1, (1975).
9. A. Dhooge, *Weld World*, **41**, 206, (1998).
10. J. S. Kim, H. S. Kwon, *Corrosion*, **55**, 512, (1999).
11. M. E. Wilms, V. J. Gadgil, J. M. Krougman, B. H. Kolster, *Mater High Temp*, **9**, 160, (1991).
12. T. H. Chen, J. R. Yang, *Mater Sci Eng A Struct Mater Prop Microstruct Process*, **11**, 28, (2001).
13. T. A. Debold, *J Met*, March, 12-5, (1989).
14. Y. H. Lee, K. T. Kim, K. Y. Kim, Y. D. Lee, *Mater Sci Technol*, **14**, 757, (1998).
15. N. Lopez, M. Cid, M. Puiggali, *Corros Sci*, **41**, 1615, (1999).
16. ASTM A262-02: *Standard Practices for Detecting Susceptibility to Intergranular Attack in Austenitic Stainless Steels*.
17. ASTM G108-94: *Standard Test Method for Electrochemical Reactivation (EPR) for Detecting Sensitization of AISI Type 304 and 304L Stainless Steels*.
18. F. B. Pickering, *International Metals Reviews*, **Vol.21**, 227, December 1976.
19. A. Hanson and J. G. Parr, *The Engineers Guide to Steel*, Addison-Wesley, Reading, MA, 265, (1965).

20. B. Weiss and R. Sticler, *Metallurgical Transactions*, **Vol.3**, 851, (1972).
21. V. N. Krivobok, *The Book of Stainless Steels*, E. E. Thum, ed., American Society for Steel Treating, Cleveland, Ohio, (1933).
22. C. Husen, C. H. Samans, *Chemical Engineering*, 178, January (1969).
23. B. Strauss, H. Schottky, and J. Hinnuber, *Zeitschrift fuer Anorganische Chemie*, **Vol.188**, 309, (1930).
24. E. C. Bain, R. H. Aborn and J. B. Rutherford, *Transactions of the American Society of Steel Treatment*, **Vol.21**, 481, (1933).
25. P. L. Andresen, F. P. Ford, S. M. Murphy and J. M. Perks, *Proceedings of the Fourth International Conference on Environmental Degradation of Materials in Nuclear Power Systems – Water Reactors*, NACE, International, Houston, TX, p.1, (1989).
26. T. R. Anthony, *Proceedings on Radiation Induced Voids in Metals and Alloys*, J. W. Corbet and L. C. Ianiello, eds., U.S. Atomic Energy Commission Symposium Series 26, CONF 710601, p.630, (1971).
27. M. E. Nicholson, C. H. Samans and F. J. Shortsleeve, *Transactions of the American Society for Metals*, **Vol.44**, p.601, (1952).
28. C. J. Novak, in *Handbook of Stainless Steels*, D. Peckner and I. M. Bernstein eds., McGraw-Hill Inc., New York, p.53, (1977).
29. A. J. Lena and W. E. Curry, *Transactions of the American Society for Metals*, **Vol.47**, p.193, (1955).
30. J. K: L. Lai, *Materials Science and Engineering*, **Vol.61**, p.101, (1983).
31. E. L. Brown et. al., *Metallurgical Transactions A*, **Vol.14A**, p.791, (1983).
32. H. Cao, S. Hertzman and B. Hutchinson, *Stainless Steels / 87, poster paper E*, Institute of Metals, London, (1987).
33. R. O. Williams, *Transactions AIME-TMS*, **Vol.212**, p.497, (1958).
34. J. J. Demo, *Structure, Constitution and General Characteristics of Wrought Ferritic Stainless Steels*, ASTM-STP 619, American Society for Testing and Materials, Philadelphia, (1977).
35. H. Hoffmeister, R. Mundt, *Arch Eisenhüttenwes*, **11**, 159, (1981).
36. H. D. Solomon, *paper presented at ASM Metals Congress*, October 1982, Preprint No. 8201-003.

37. J. W. Pugh and J. O. Nisbet, *Transactions of AIME*, **Vol. 188**, p. 286, (1950).
38. R. M. Davison and J. D. Redmond, *Materials Performance*, **Vol. 29**, p. 57, (1990).
39. K-J. Blom, in *Stainless Steels/87*, p. 123, Institute of Materials, London, (1988).
40. P. Payson, *Transactions AIME*, **Vol. 100**, p. 306, (1932).
41. H. D. Solomon and T. M. Devine, *General Electric Company Report No. 82CRD276*, General Electric Co., Schenectady, NY, November (1982).
42. R. Lagneborg, in *Proceeding of the International Conference on Stainless Steels*, p. 647, **11**, Iron and Steel Institute of Japan, Tokyo, (1991).
43. T. M. Devine, *Metallurgical Transactions*, **Vol. 11A**, p. 791, (1980).
44. G. Herbsleb and P. Schwaab, *paper presented at ASM Metals Congress, Preprint No. 8201-002*, October (1982).
45. K. Kondo et al., in *Proceedings of the Conference on Processes and Materials: Innovation Stainless Steel*, **Vol. 2**, p. 2.191, Associazione Italiana di Metallurgia, Milan, (1993).
46. J. K. L. Lai, *Materials Science and Engineering*, **58**, 195, (1983).
47. Y. Minami, H. Kimura, and Y. Ihara, *Materials Science and Technology*, **2**, 795, (1986).
48. M. Schwind, J. Kallqvist, J. O. Nilsson, J. Agren, and H. O. Andren, *Acta Materialia*, **48**, 2473, (2000).
49. A. Desestret, J. Charles, in *Stainless Steels*, P. Lacombe, B.Baroux, G. Béranger, eds., *Les Editions de Physique*, pp.613, (1991).
50. B. Wallen, and J. Olsson, *Corrosion Resistance in Aqueous Media*, in *Handbook of Stainless Steel*, D. Peckner and I.M. Bernstein, Eds., McGraw-Hill, New York, (1977).
51. R. L. Beauchamp, *Ph. D. Dissertation. Ohio State University*, 1966.
52. I. Olejford, B. Brox, and U. Jelvestam, *Journal of the Electrochemical Society*, **132**, 2854, (1985).
53. C. R. Clayton, and I. Olejford, *Passivity of Austenitic Stainless Steel*, in *Corrosion Mechanism in Theory and Practice*, P. Marcus and J. Oudar, Eds., Marcel Dekker Inc., New York, (1995).

54. A. J. Sedriks, *Metallurgical Aspects of Passivation of Stainless Steels in Stainless Steel'84, 1985*, G. L. Dunlop ed., Chalmers University of Technology, Göteborg, Institute of Metals.
55. H. H. Uhlig, and R. W. Revie, *Corrosion and Corrosion Control, 3rd ed.*, John Wiley and Sons Inc., New York, (1985).
56. H. H. Strehblow, *Passivity of Metals, in Advances in Electrochemical Science and Engineering Vol. 8*, R. C. Alkire ed., Wiley-VCH, (2002).
57. I. Olefjord, and B. O. Elfstorm, *Corrosion-NACE*, **38**, 46, (1982).
58. K. Sugimoto, and Y. Sawada, *Corrosion Science*, **17**, 425, (1977).
59. N. D. Tomashov, and G. P. Chernova, *Passivity and Protection of Metals against Corrosion*, Plenum Press, New York, (1967).
60. A. Legat, V. Dolecek, *J. Electrochem. Soc.*, **142**, 1851, (1995).
61. D. A. Jones, *Principles and Prevention of Corrosion*, Prentice Hall Inc., New Jersey, (1996).
62. ASTM A923-03: *Standard Test Methods for Detecting Detrimental Intermetallic Phase in Duplex Austenitic/Ferritic Stainless Steels*.
63. A. P. Majidi and M. A. Streicher, *Corrosion*, **40**, 584, (1984).
64. R. F. A. Jargelius, S. Hertzman, E. Symniotis, H. Hanninen and P. Aaltonen, *Corrosion*, **47**, 429, (1991).
65. V. Cihal, Proc. *Mechanical Behavior of Materials*, Kyoto, Japan, July 29 – Aug 2, p.557, (1991).
66. M. Verneau, C. Lojewski and J. Charles, *Proc. Duplex Stainless Steel '91, Beaune*, Les Ulis, France, p.863, (1992).
67. S. J. Goodwin, B. Quayle and F. W. Noble, *Corrosion*, **43**, 743, (1987).
68. N. Lopez, M. Cid, M. Puiggali, I. Azkarate, A. Pelayo, *Materials Science and Enigneering A*, **A229**, 123, (1997).
69. W. L. Clarke, V. M. Romero, J. C. Danko, *CORROSION/77, Preprint No.180, NACE*, Houston, Texas, (1977).
70. W. L. Clarke, R. L. Cowan, W. L. Walker, *Intergranular Corrosion of Stainless Alloys, ASTM STP 656*, R. F. Steigerwald, ed., ASTM, Philadelphia, Pennsylvania, p.99, (1978).
71. W. L. Clarke, *The EPR method for detection of sensitization in stainless steels, Prepared for U.S. Nuclear Regulatory Commission and General Electric Company*, NUREH/CR-1095, GEAP-24888. Available from National Technical Information Service, Springfield, VA 22161.

72. A. P. Majidi, M. A. Streicher, *Corrosion*, **Vol.40**, No.8, p.393, (1984).
73. *ASTM Book of Standards*, **Vol.10**, A262, ASTM, Philadelphia, Pennsylvania, (1978).
74. M. A. Streicher, *ASTM Bulletin No.188, American Society for Testing Materials*, Philadelphia, Pennsylvania, p.35, February (1953).
75. G. S. Was, V. B. Rajan, *Corrosion*, **43**, 576, (1987).
76. M. Verneau, C. Lojewski, J. Charles, in *Proceedings of the Conference: Duplex Stainless Steel '91. Editions de Physique*, p.863, (1992).
77. E. Otero, C. Merino, C. Fosca, F. Fernandez, in *Conference: Duplex Stainless Steel '94*, Glasgow, Scotland, 13-16 November (1994).
78. S. K. Dhua, A. Ray, *Mater Charact*, **37**, 1, (1996).
79. G. F. Vander Voort, *Metallography: principles and practice*. ASM International, McGraw-Hill Inc., (1994).
80. *ASTM Book of Standards*, **Vol.11**, E 112, ASTM, Philadelphia, Pennsylvania, (1979).
81. T. Amadou, C. Braham, and H. Sidhom, *Metallurgical and Materials Transactions*, **35A**, 3499, (2004).
82. N. Lopez, M. Cid, M. Puiggali, *Corrosion Science*, **41**, 1615, (1999).
83. T. A. DeBold, Duplex stainless steel – microstructure and properties, *J. Met*, 12-15, March, (1989).
84. B. Josefsson, J. –O. Nilsson, and A. Wilson, in *Duplex Stainless Steel '91, J. Charles and S. Bernhardsson, eds., Les Editions de Physique*, Beaune, Bourgogne, France, **Vol.1**, p.67, (1991).
85. C. –S. Huang and, C. –C. Shih, *Mater Sci Eng A*, **Vol.402**, p.66, (2005).
86. M. Pohl, O. Storz, T. Glogowski, *Materials Characterization*, **58**, 65 (2007).
87. J. W. Elmer, T. A. Palmer, and E. D. Specht, *Metallurgical and Materials Transactions A*, **38A**, 464, (2007).
88. T.H. Chen, J.R. Yang, *Materials Science and Engineering A*, **A311**, 28, (2001).
89. E. Angelini, B. De Benedetti, F. Rosalbino, *Corrosion Science*, **46**, 1351, (2004).

90. M. Akashi, T. Kawamoto, and F. Umemura, *Boshoku Gijutsu (Corrosion Engineering)*, **Vol.29**, p.163, (1980).
91. R. Park, N. Wright, in: R. A. Rula (ed.), *Toughness of Ferritic Stainless Steels*, ASTM STP 706, p.2, (1979).
92. C.-J. Park, H.-S. Kwon, *Corrosion Science* **44**, 2817, (2002).
93. A. Pardo, M.C. Merino, A.E. Coy, F. Viejo, M. Carboneras, R. Arrabal, *Acta Materialia*, **55**, 2239, (2007).
94. E. L. Hall, C. L. Briant, *Metal Trans A*, **Vol.15**, p.793, (1984).